The Interaction Between the Substrate and Frost Layer Through Condensate Distribution

J. L. Hoke, J. G. Georgiadis, and A. M. Jacobi

ACRC TR-177 November 2000

For additional information:

Air Conditioning and Refrigeration Center
University of Illinois
Mechanical & Industrial Engineering Dept.
1206 West Green Street
Urbana, IL 61801

(217) 333-3115

Prepared as part of ACRC Project #106
The Effect of Hydrodynamics, Substrate Energy and Structure on Frost Growth
J. G. Georgiadis, A. M. Jacobi, P. S. Hrnjak, and C. W. Bullard, Principal Investigators

The Air Conditioning and Refrigeration Center was founded in 1988 with a grant from the estate of Richard W. Kritzer, the founder of Peerless of America Inc. A State of Illinois Technology Challenge Grant helped build the laboratory facilities. The ACRC receives continuing support from the Richard W. Kritzer Endowment and the National Science Foundation. The following organizations have also become sponsors of the Center.

Amana Refrigeration, Inc.
Arçelik A. S.
Brazeway, Inc.
Carrier Corporation
Copeland Corporation
DaimlerChrysler Corporation
Delphi Harrison Thermal Systems
Frigidaire Company
General Electric Company
General Motors Corporation
Hill PHOENIX
Honeywell, Inc.
Hussmann Corporation
Hydro Aluminum Adrian, Inc.
Indiana Tube Corporation
Invensys Climate Controls
Kelon Electrical Holdings Co., Ltd.
Lennox International, Inc.
LG Electronics, Inc.
Modine Manufacturing Co.
Parker Hannifin Corporation
Peerless of America, Inc.
Samsung Electronics Co., Ltd.
The Trane Company
Thermo King Corporation
Valeo, Inc.
Visteon Automotive Systems
Wolverine Tube, Inc.
York International, Inc.

For additional information:

Air Conditioning & Refrigeration Center
Mechanical & Industrial Engineering Dept.
University of Illinois
1206 West Green Street
Urbana, IL 61801

217 333 3115

Abstract

Microscopic observations of frost deposition on a variety of substrates having different contact angles, (polytetrafluoroethylene PTFE, kapton, glass and others) allow the quantification of substrate effects on frost structure during inception and growth. The deposition of water vapor at the beginning of the frosting process on a clean glass substrate is found to be as condensate (condensation frosting) rather than as ice (ablimation frosting) for a substrate temperatures above –33°C and an absolute humidity above 0.15 g/kg. The inception of "condensation frosting" (the condensation period and early frost growth period) is further examined microscopically as a function of air and substrate temperatures, absolute humidity, and substrate contact angle. The water distribution on the substrate at the end of the condensation period is found to be strongly dependent on substrate temperature, humidity ratio, and substrate contact angle. Colder substrates result in smaller more uniform droplets and substrates with lower contact angles result in shorter, larger diameter droplets with a larger percentage of the substrate covered. The effective density of the condensate on hydrophobic substrates is found to be lower than that on hydrophilic substrates. The structure and form of the ice immediately after freezing is substrate dependent. High-speed imaging of the freezing process is used to study the propagation of the freezing front in a droplet. The images show that a protrusion is formed at the top of the droplets during freezing. From observations, this protrusion is hypothesized to result from the convective condition at the droplet surface and the difference in specific volume between liquid and solid water. Additionally, the apparent ejection of water vapor during freezing of a droplet on a

hydrophobic substrate was observed. This ejection of water vapor is thought to be caused by the warming of the droplet caused by the release of latent heat. In contrast to trends observed during the early growth period, the growth rate of mature frost is found to decrease with substrate contact angle while frost density is found to increase. This behavior is explained in terms of the effect of substrate contact angle on the structure and form of the incipient frost, which constitutes the initial condition for further (mature) frost growth. A higher conductivity layer is formed on the hydrophilic than on the hydrophobic substrate. A model relating crystal orientation to conductivity is used to simulate the frost growth rate and density on the two different substrates and match the experimental data. Using similar reasoning, the higher conductivity frost formed on colder substrates is also explained.

Table of Contents

Page

List of Tables

Page

List of Figures

Page

Nomenclature

A	kinetic constant, $1/cm^2$-s
c_p	constant pressure specific heat, kJ/kg-K
C_p	condensation period, s
D_{ab}	binary diffusion coefficient, m^2/s
D	diameter, m
f	geometric factor (Eq. 3.3 and 3.14)
g	geometric factor (Eq. 3.4)
h	droplet height, m
	heat transfer coefficient, W/m^2-K
H	channel height, m
h_m	mass transfer coefficient, m/s
J	nucleation rate, $1/s\text{-}m^2$
J'	nucleation rate per particle, 1/s
k	thermal conductivity, W/m-K
	Boltzmann constant, $1.38x10^{-23}$ J/K
m	mass, kg, or $\cos\theta$
m_ϕ	mass converted from liquid to solid, kg
$\dot{m}$	mass deposition rate, kg/s
m''	mass, kg/m^2
$\dot{m}''$	mass flux, kg/m^2-s
n	index of refraction
N	number of drops in field of view
N''	number of drops per unit area, $1/mm^2$
P	probability of freezing
q''	heat flux, W/m^2
r^*	critical radius for nucleation, Å
R	arithmetic mean surface roughness, Å
RH	relative humidity
t	time, s
T	temperature, K or °C
v	average velocity, m/s
V	volume m^3
W	channel width
x	ratio of radii

z height from substrate, m

Dimensionless Groups

Fo Fourier number, $\beta t/(c_{pa} \cdot H^2)$

Ja Jacob number, $c_{pa}\Delta T_\infty/\lambda_{sg}$

Le Lewis number, α/D_{ab}

Re Reynolds number, vD_h/ν

Greek Symbols

α thermal diffusivity, m^2/s
constant, $°C^{-1}$ (Eq. 3.12)

β empirically determined constant, $W \cdot m^2/(kg \cdot K)$

γ area ratio

Γ dimensionless frost height, δ/H

δ frost or layer height, m

ΔG^* Gibbs free energy of nucleus formation, J

ΔG_v change in Gibbs free energy from state 1 to 2, J/m^3

ΔT_w temperature change across frost layer (T_s-T_w), K

ΔT_∞ temperature change across thermal boundary layer $(T_\infty-T_s)$, K

$\Delta \rho_v$ partial density change, freestream to surface $(\rho_{v,\infty}-\rho_{v,s})$, kg/m^3

Δx distance, m

ε volume fraction

ζ fraction of substrate covered by liquid

θ contact angle, degrees

Θ dimensionless temperature ratio, $\Delta T_\infty/\Delta T_w$

λ latent heat, kJ/kg

ν kinematic viscosity, m^2/s

ρ density, kg/m^3

σ surface tension, N/m or surface free-energy, J/m^2
standard deviation

τ dimensionless frost environmental time (Eq. (1.1), (1.2))
dimensionless time constant (Eq. 7.11, 7.12)

Φ dimensionless humidity ratio, $\Delta \rho_v/\rho_a$

ω humidity ratio

Ω average frost spire orientation

Subscripts

1 phase 1

2 phase 2

a air or area weighted average

b water

D diameter

eff	effective
f	frost
g	gas
h	hydraulic
i	initial
ice	ice
l,L	liquid
m	mature
s	solid
tp	water triple point
v	water vapor or volume weighted average
w	wall or substrate
x	distance measured from leading edge
∞	free stream

1 Introduction and Background

1.1 Motivation

The properties of solid water depend on the scenario under which the solid is formed, its history, and present environment. Distinctive properties range from those observable by the naked eye, such as clarity and texture, to properties measured in a lab, such as atomic structure and permittivity. The desire to understand the mechanisms which affect the properties of solid water has been the basis of numerous studies (Hobbs 1974); however, there is still much that is unknown. This study focuses on the deposition of water vapor on substrates where the environmental conditions are such that frost forms.

Frost growth can be considered to occur under two distinct scenarios: the first shall be called "condensation frosting" and the second, "ablimation frosting". The descriptors "condensation" and "ablimation" –as used in this thesis- describe the way frost growth is initiated. In condensation frosting, water vapor deposites to form liquid droplets even at substrate temperatures well below the triple point of water. These droplets grow and coalesce with neighboring droplets. After some period, the droplets freeze and additional water vapor ablimates on to the frozen droplets creating frost. In ablimation frosting, water vapor initially deposits on the substrate as a solid, forming the frost layer which continually grows through ablimation.

For condensation frosting, three regimes will be considered. The first regime is designated the *condensation period.* The condensation period ends and the *early frost*

growth period begins when the condensate begins to freeze. The early growth period is characterized by an almost constant frost thickness growth rate. The transition from the early growth period to the *mature growth period* is gradual and hence difficult to demarcate; however, the mature growth period is characterized by an increase in thickness proportional to the square root of time. The terms "early" and "mature frost growth period" are often used in the frost literature while the term "condensation period" is sometimes referred to as a "transition time" and sometimes this period is not distinguished at all. There are slight variations in the definitions and names used in the literature, so it is imperative to define these terms, cf. Yonko and Sepsy (1967), Hayashi *et al.*, (1977a), Tao *et al.* (1993b), and Sahin (1995). In Fig. 1.1 the structure of the frost corresponding to the different periods is illustrated. Because of the complexity of frosting, this research is focused on a few facets of the frosting process that have particular engineering relevance.

Frost forms on a surface when its temperature is below the triple point of water and the dew point of the surrounding air. These two conditions often occur in the aircraft industry, where frost growth has a detrimental effect on lift and drag (Bragg *et al.* 1994). In the agricultural industry frost can decrease product quality (Leemans *et al.* 1999), and in the air-conditioning and refrigeration industries it can decrease efficiency (Stoecker 1957; Tassou and Marquand 1987). Although there are several industries where this research may be relevant, the principal goal of this work is to reduce the deleterious effects that frost has on the air-conditioning and refrigeration industries. Even though, a very thin frost layer can enhance heat transfer due to increased surface area and roughness (Stoecker 1957), the accumulation of frost on air-handling surfaces can

increase the thermal resistance by up to 75% depending on the air-conditioning and refrigeration application (Emery and Siegel 1990). Frost can also reduce the airflow rate through the evaporator. Stoecker (1957) measured a decrease in airflow from 0.647 m^3/s to 0.255 m^3/s after 2.95 kg of frost accumulation on a finned evaporator with a surface area of 34.4 m^2. Of course, flow rate effects are a function of evaporator design as well as environmental parameters. Eventually, a defrost cycle is required to melt the accumulated frost and to mitigate the performance impact of frost in refrigeration systems. Defrosting is an inherently inefficient process since it requires the transfer of heat into the refrigerated compartment.

As an example, a typical supermarket dairy case, which is continuously open to the environment, requires 2 to 3 defrost cycles per day. A defrost cycle typically lasts 20 to 30 minutes and 328 W/m are supplied to a 2.43 to 3.66 m dairy case (Swofford 2000). The temperature within the dairy case is of greater concern to manufacturers during the defrost cycle than the energy used (Swofford 2000). A pending regulation concerning the temperature, NSF-7 (National Sanitation Foundation International regulation 7), requires the temperature within a dairy case always be below 5°C.

As will be shown in Chapter 3, condensation frosting is generally the scenario encountered on a refrigerator evaporator; therefore, to make the greatest impact on frost growth in the refrigeration industry, condensation frosting is the main focus of this research. The review of the literature is divided into sections that follow the development of frost starting with the condensation period and ending with the mature growth period. Where appropriate, the sections are broken into experimental and numerical reviews.

1.2 Competition Between Condensation and Ablimation

The vast majority of the experiments on frost deposition at air temperatures below 0°C have been carried out by researchers in the field of meteorology. Using cloud chambers, they have investigated the structure of ice crystals suspended in supersaturated air at various temperature ranges below 0°C. They have also developed theories on the nucleation of ice from the vapor phase, as well as from supercooled water droplets. Hobbs (1974) provides a comprehensive survey of such literature. It is useful to emphasize that most of the meteorological experiments consider ice formation on *discrete* particles acting as nucleators.

Shinagawa *et al.* (1992) investigated the heterogeneous nucleation of water vapor on a cooled copper substrate. Experiments were performed for water vapor only, there was no air present. The transition from deposition of liquid to deposition of solid was found to occur at a vapor pressure of 200 Pa, and a substrate temperature of approximately 257 K. The vapor pressure was measured during the experiment to determine which path, condensation or ablimation, the deposition followed. A decrease in the cell vapor pressure indicated the onset of either condensation or ablimation. Further cooling of the substrate resulted in a continuous decrease in vapor pressure for ice (eventually, ice could be seen visually) or a change in the vapor pressure slope as the deposited water changed from liquid to ice.

Shinagawa *et al.* (1994) studied heterogeneous nucleation of water vapor and gave a relation for the temperature at which ablimation occurred as a function of the water vapor pressure. This relation was developed for pure water vapor and the experimental technique used was identical to that used by Shinagawa *et al.* (1992).

The phase transition from vapor to solid for cyclohexane depositing on a substrate was examined using kinetic theory and classical nucleation theory by Shinagawa *et al.* (1995). In their experiments and model, the substrate temperature was held constant while the vapor pressure of cyclohexane increased within the test cell. The model predicted the pressure in the test cell until after the beginning of the deposition of water. This deviation in prediction was attributed to the release of latent heat during ablimation, which altered the substrate and crystal temperatures. To correct for this effect, the surface temperature of the crystal and the temperature of the substrate were adjusted in the model when deposition was predicted. The model satisfactorily predicted the experimental data when the substrate temperature was increased by 0.4 K and the crystal temperature was increased by 1.0 K.

1.3 Experimental Condensation Period Studies

Although many authors have examined the role of the substrate contact angle on condensation (Griffith and Lee 1967; Graham and Griffith 1973; Tanaka 1975; Holden *et al.* 1984), surprisingly little work has been published in the frost literature about the condensation period of frosting, despite the fact that almost all frosting in refrigeration applications begins with condensation frosting. The dearth of research is probably a result of the small performance impact that occurs during the condensation period. However, the water distribution which occurs during the condensation period affects the properties (thickness, density and conductivity) of the mature layer and is therefore significant.

Saito *et al.* (1984) observed condensate forming on a flat plate during frosting and defined the "freezing time" as the time from the beginning of condensation to the freezing of the condensate. The freezing time was measured as a function of substrate temperature, humidity ratio, and free-stream velocity. This study was conducted using a copper plate under forced convection conditions.

Seki *et al.* (1985) examined the condensation period on two substrates of equilibrium contact angle 110° and 43°. No indication of contact angle hysteresis was given. The duration of the condensation period was significantly longer on the hydrophobic substrate. A model for the growth of condensate based on contact angle was developed to predict droplet diameter during the condensation period. The end of the condensation period was predicted based on a single average droplet diameter. No further correlation between mature frost properties and condensate was provided.

Tao *et al.* (1993b) examined the early growth period of frost grown on a flat plate in forced convection. Plate temperatures ranged from -25 to -5° C. Re_{Dh} ranged from 2840 to 5680. The free-stream air temperature was held at 20.5° C and the relative humidity ranged from 30 to 90%. The test surface was an aluminum plate with a surface roughness of 0.167 μm. Two transition times were defined. The first transition time (the condensation period) occurred when the large water droplets on the surface froze. The second transition time occurred when a "homogeneous" frost layer was first evident. On the basis of observations, they constructed a schematic representation of the structure of frost during the condensation period and early growth period. The radii of the droplets were measured and a surface area fraction was defined as the ratio of the drop contact area to the total area. Larger droplets were formed for higher humidities and higher plate

temperatures as well as higher free stream velocities. The uncertainty of measuring the actual frost thickness was determined to be 50% by examining the frost thickness variability. The surface area fraction was relatively insensitive to plate temperature, humidity, and Reynolds number. The error in determining the surface area fraction was estimated to be between 10 and 20%.

Tao *et al.* (1994) microscopically examined the early frost growth on flat plates of four different materials. The four different surfaces used were aluminum, brass, plastic, and PTFE. The radii of the water droplets formed on the plastic and PTFE surfaces in general were smaller than the radii of water droplets formed on aluminum or brass for all Re numbers and all humidity ratios tested (the contact angle on the aluminum and brass is presumably smaller than on PTFE and plastic). Plastic and PTFE had higher void fractions than the aluminum or brass under all conditions tested. The droplets on the PTFE and plastic froze earlier than the droplets on the aluminum or brass, contrary to the findings of Seki *et al.* (1985). This significant difference is probably due to oil or other contamination on the metallic substrates, altering the equilibrium freezing temperature. The duration of the condensation period was also recorded. No contact angle measurements nor surface roughness measurements were reported.

1.4 Freezing Characteristic Studies

Studies of the condensation period consist primarily of observations, without a direct link of early or mature frost properties to this initial deposition. The condensation period naturally ends at the onset of freezing. The freezing front propagates quickly across the hydrophilic substrate (Georgiadis *et al.* 2000), but moves in a progressive

manner from droplet to droplet across the hydrophobic substrate, see Georgiadis *et al.* (1996) for a detailed description of this process.

Horibe *et al.* (1993) described the freezing characteristics of a 3 mm droplet placed at the leading edge of a plate. Experiments were conducted for plate temperatures from 0° to –15°C, air temperatures from 18° to –15°C, and air velocities up to 10 m/s. The initiation of freezing was found to occur at the substrate, even for conditions where the air stream was significantly cooler than the substrate. In stagnant air, the freezing front was found to propagate up from the substrate, remaining parallel to the substrate. A protrusion was formed at the top of the droplet at the completion of the freezing process. The formation of this protrusion was speculated as due to the difference in specific volume between ice and water. With an air velocity of 5 m/s and a wall temperature of –5°C, the protrusion was found to form toward the downstream side of the droplet as the air temperature was decreased. The size of the protrusion also seemed to increase with decreasing air temperature. The position of the protrusion was also moved downstream by increasing air velocities. No clear explanation for the formation of the protrusion or of its behavior was provided.

The solidification of a droplet in a quiescent environment was examined experimentally and numerically by Kawanami *et al.* (1997). Without a forced convection condition, the freezing front was found to propagate from the substrate to the top of the droplet, and no protrusion was formed during freezing.

1.5 Experimental Early Frost Growth Studies

Hayashi *et al.* (1977a) examined the early growth period of frost, but they completely ignored the condensation period. Frost structure was classified into four main groups correlated to substrate temperature and mass transfer driving potential. The early growth period was characterized by the existence of frost crystals on the surface growing vertically (the height of the crystals changed linearly with time) with a relatively large distance between crystals. During the transition from the early growth period to the mature growth period, the vertical crystals developed branches at the top of the crystals. These branches formed a mesh which made a more uniform frost surface. This growth continued, resulting in a relatively flat frost surface. The density of the frost layer increased in this period because of the three dimensional growth of the frost. There was no investigation as to the effect of substrate contact angle, nor were substrate properties measured.

Saito *et al.* (1984), observed the early frost growth and noted that the early growth was predominantly normal to the substrate occurring on "frost nuclei" or frozen droplets. Correlations for the frost thickness and density were developed based on the environmental parameters affecting the condensate, but only a single substrate was examined.

Examining the inception of frost with a microscope, Seki *et al.* (1985) found no significant difference in the early frost growth on the frozen droplets as a function of substrate contact angle. A frost critical time was defined as the time required for the frost to grow to a thickness of 0.5 mm, and a model predicting the thickness and growth of the condensate and the early growth of the frost was developed.

Tao *et al.* (1994) used a microscope to examine early frost growth on vertical fins of two different materials and flat plates of four different materials. For the fin tests, the root temperature varied from -20 to -6° C while inlet air temperature was held constant at 21° C. The relative humidity of the free stream ranged from 30 to 60%. The Reynolds number based on downstream location varied from 130 to 200. The two materials tested were aluminum and brass. Neither the surface roughness nor the contact angle of these samples were reported. This omission of substrate properties makes reproduction and application of these experiments difficult. The frost on the leading edge was found to be of higher density and thicker than frost found elsewhere on the fin. At the midpoint of the fin in the stream-wise direction, the frost appeared to have large, fragile crystals. The growth direction of these crystals was modified by the flow so that they were growing in a downstream direction. At the trailing edge, the frost was similar to that at the leading edge; however, visual inspection revealed that the density and thickness appeared lower. These observations were qualitative with no indication of how density was ascertained with the naked-eye. The growth rate on the aluminum fin appeared slower than on the brass fin. This conclusion was drawn from the comparison between a single test on the aluminum fin with $Re_x = 180$ and a single test on the brass fin with $Re_x = 130$.

Tao *et al.* (1994) examined the growth of frost on a flat plate in a laminar air flow. Four different surfaces were used as the substrate: aluminum, brass, plastic, and PTFE. The test conditions were similar to those specified above, except the Re_x range varied from 2840 to 5680. Two transition times were recorded for each sample. The first transition time occurred when the condensed water droplets changed from liquid to solid. The second transition time occurred when a significant number of branches formed such

that the ice column pattern had vanished. The images showed that the PTFE surface reached the second transition time at about the same time that the aluminum surface reached the first transition time. This finding is contrary to that of Seki *et al.* (1985).

Using confocal microscopy, Georgiadis (1996) reported 3-D, time-resolved measurements of frost inception on two substrates: extruded aluminum heat exchanger fin stock, and a thicker 6061-T aluminum plate. The plate was finished in an electron discharge machine and then electro-polished.

1.6 Experimental Mature Growth Studies

A clear relationship between early growth and mature growth has not yet been established in the technical literature on frost. Furthermore, studies of early growth predominantly provide descriptions of visual observations—not quantitative measurements of frost thermophysical properties. On the other hand, there are many studies in the open literature that examine mature frost growth properties as a function of the environmental parameters for laminar flow over simple geometries. The trends reported in these studies are quickly reviewed to provide context for the present study.

For thermally developing flow over a flat plate in a channel, the frost thickness, density and conductivity have been found to increase with increasing humidity (Thigpen *et al.* 1964; Yonko and Sepsy 1967; Hayashi *et al.* 1977a; Ostin and Andersson 1991; Mao *et al.* 1992; Sahin 1994; Storey 1997). There is some discrepancy in the reported effect of Reynolds number on frost thickness; however, under the conditions of this experiment, the Reynolds number has been clearly reported to have no effect on frost thickness (Storey 1997). It is generally accepted that increasing the Reynolds number

increases the density and conductivity of the frost (Yonko and Sepsy 1967; Biguria and Wenzel 1970; Hayashi *et al.* 1977a; Sahin 1994). Increasing the substrate temperature or air temperature causes the frost growth rate to decrease but the density increases, and most authors correlate conductivity with density (Ostin and Andersson 1991; Sahin 1994). Interestingly, Mao *et al.* (1993) reported that the conductivity increases with decreasing substrate temperature in apparent contradiction to the correlations proposed which correlate conductivity with density (since density decreases with decreasing substrate temperature). In the full-growth period, the thickness and density of the frost are found to increase with time while the conductivity is found to approach a constant (Thigpen *et al.* 1964; Yonko and Sepsy 1967; Biguria and Wenzel 1970; Yamakawa *et al.* 1972; Hayashi *et al.* 1977a; Tokura *et al.* 1983; Abdel-Wahed *et al.* 1984; O'Neal and Tree 1984; Ostin and Andersson 1991; Mao *et al.* 1992; Mao *et al.* 1993; Sahin 1994). Unfortunately, there was no information on the substrate surface energy and roughness for these studies. These trends in mature growth behavior are shown in Table 1.1, reproduced from Dyer *et al.* (2000) with one correction.

Fukada and Inoue (1999) investigated the water mass flux within the frost layer under free convection conditions. This study was conducted by depositing water vapor from two different sources. Initially water vapor was generated from a pool of distilled water of low deuterium concentration. After the frost grew from this source of low deuterium water, the vapor source was switched to a pool of water with a higher deuterium concentration. The vapor pressure of water is approximately 12% higher than deuterium at 0°C. The migration of deuterium was then examined by taking a core of the frost layer and measuring the deuterium concentration of cross sections in a mass

spectrometer. The mass flux inside the frost layer was found to decrease linearly from the surface of the frost layer to the substrate. Alternatively, ablimation of water vapor was found to decrease linearly from the surface of the frost to the substrate. As a result, the density profile normal to the substrate was found to be uniform. If was found that half of the water diffusing to the frost surface is deposited as additional frost thickness and half diffuses into the frost layer increasing the density. The crystal growth direction was assumed to be isotropic, thus accounting for the ratio of mass deposited for vertical crystal growth and horizontal crystal growth. A vapor diffusion model based on the diffusion of water vapor in air, with a factor correcting for the tortuosity of frost, failed to explain the experimental results.

1.7 Numerical Modeling of Mature Growth

Numerous models have been developed to try to predict the frost growth based on the environmental parameters. Most of these models are based on mass and energy balances at the frost surface (Jones and Parker 1975; Padki *et al.* 1989; Sami and Duong 1989; Tao and Besant 1993a). These models use mass diffusion within the frost layer to predict the densification of the layer over time. Usually an empirical relation for the conductivity as a function of the density is used. These models require an initial input of frost thickness and density. Several of these models along with some of the correlations used to predict frost height will be reviewed so the reader has an understanding of the approach generally implemented to model frost properties.

Tao *et al.* (1993a) developed a mathematical model for predicting the densification and growth of frost on a flat plate under forced convection conditions. A

one-dimensional transient formulation based on local volume-averaging technique was used. The local effective vapor mass diffusion rate was increased seven-fold over that measured in pure Fickian diffusion to make the model predict the measured growth rate. The frost growth was broken up into two phases. The first was the early growth phase in which the frost was modeled as ice columns. Appropriate heat and mass transfer coefficients were selected to be used in the model. In the mature growth phase, the frost was modeled as a homogeneous porous layer. Diffusion was assumed to be the only mechanism for internal water transport. The diffusion coefficient was modified by a diffusion factor which included the effects of Knudsen diffusion, metamorphism within the frost structure, pore size distribution, and the variation of gaseous pressure within the fine pores. Initial conditions were required to start the model which described the diameter and length of small ice crystals uniformly distributed on the surface. Correlations for the heat and mass transfer coefficients which take into account the surface roughness were adopted. From this model, the rate of densification was found to have a maximum near the frost surface. The frost density distribution in the full-growth period depends on the distribution during the early growth period. The heat flux was found to increase initially due to the ice columns acting like fins. The heat flux decreased monotonically in the full-growth period.

Sahin (1995) performed an analytical investigation of the frost nucleation and growth during the crystal growth period. The frost was modeled as columns. Frost density increases were manifest as larger column diameters. Conservation of mass, energy and vapor diffusion were used to model the frost growth. An initial volumetric ratio of frost columns was required to start the model and was obtained from an empirical

equation, which expressed initial density as a function of environmental parameters. Sahin based the density of the frost on experiments conducted by cloud physicists where the density was expressed only as a function of ablimation temperature. The temperature of crystal growth was the frost surface temperature. The thickness of the frost was predicted within 25% of experimental data.

Le Gall *et al.* (1997) developed a one-dimensional, transient model of the growth and densification of frost in a channel. Heat and mass transfer balances as well as diffusion were used to model the process. Classical heat and mass transfer correlations for a flat plate were used. Initial values of density and thickness were needed to start the model. Surface melting was taken into effect in the model. In order to get the model to match experimental data, the diffusion factor had to be increased by a factor up to 8. No experimental or physical justification was provided to support this alteration of the diffusion coefficient. No models have been proposed to account for the effect that the substrate contact angle has on frost properties.

1.8 Mature Growth Correlations

Aside from numerical models, there are several correlations in the literature to predict frost thickness, conductivity, and density as a function of environmental parameters. Conductivity is usually predicted based on frost density, although several studies predict the conductivity based on environmental conditions. Schneider (1978) proposed a model of frost thickness based on the transport of mass and heat to a single frost needle. By including scaling arguments and empirical results, an equation predicting the frost thickness as a function of environmental parameters and time was

developed. The equation predicts Schneider's experimental data and data from other studies within 10%.

Another model for frost thickness was developed by Storey and Jacobi (1999). This model was based on frost-surface heat flux and mass continuity. From their analysis they found that the dimensionless frost thickness was proportional to the square root of the environmental time, τ.

$$\Gamma = \sqrt{\tau} = \frac{\delta}{H} \tag{1.1}$$

where

$$\tau = \mathrm{Fo}\frac{\mathrm{Ja}\cdot\Phi}{\Theta\left(\mathrm{Ja}\cdot\mathrm{Le}^{2/3}+\Phi\right)} \tag{1.2}$$

and

$$\mathrm{Fo} = \frac{\beta\cdot t}{c_{pa}\cdot H^2} \tag{1.3}$$

The other dimensionless groups, Ja, Φ, Le, and Θ, are defined in the nomenclature. The constant, β, in the Fourier number was determined from the experimental data to be $8.7\text{x}10^{-4}$ W·m^2/kg·K with an RMS deviation of 13%. Several assumptions used to develop this model restrict its use at early times ($\sqrt{\tau} < 0.1$) (see Storey and Jacobi, 1999). The frost surface temperature was assumed to be at the triple point of water. The data presented by Storey and Jacobi, which consisted of 291 observations were consistent with Eq. (1.1) to within the uncertainty of the measurements, $\pm$ 0.01 on Γ and $\pm$ 8% on $\sqrt{\tau}$. The model was also used to normalize the effects of environmental conditions on the data acquired in the present investigation.

Mao *et al.* (1999) correlated the thickness, density and conductivity as a function of environmental parameters, location on a flat plate, and Reynolds number, for conditions similar to those found in a freezer. The frost surface was characterized as being either smooth or rough and correlations predicting frost properties for both types of frost were presented.

1.9 Mature Frost Property Dependence on Substrate

It is evident from the existing literature that numerous studies have been conducted under frosting conditions; however, there are still several areas which require further investigation. The mechanism by which the substrate affects frost properties is one area which requires further investigation. There are three fundamental studies and one application study available in the literature and they will be reviewed in that order.

Seki *et al.*(1984) examined the incipient growth of frost for two different substrate contact angles, 110 and 43. The hysteresis in the contact angle was not measured. The thickness of frost grown on the hydrophilic substrate was found to be greater than that grown on the hydrophobic substrate, in all cases. The density of the frost was higher on the hydrophobic substrate than on the hydrophilic substrate. No further insight into the relation between the substrate and frost thickness was presented.

Dyer *et al.* (2000) evaluated the frost growth rate on three different substrates. The advancing contact angles for the three substrates, polytetrafluoroethylene (PTFE) coating on steel, bare aluminum, and a hydrophilic-coated aluminum, were 106, 92 and 67°, respectively. The bare aluminum was used as the reference material. The frost thickness grew 19% slower on the PTFE than on the reference bare aluminum. The frost

gown on the hydrophilic-coated aluminum grew 13% faster than on the reference. The initial water coverage at freezing was hypothesized to alter the thermal resistance of the frost layer and cause the difference in growth rates.

Okoroafor and Newborough (2000) investigated the effect on the growth rate and surface temperature of frost of a substrate covered by water-absorbing polymeric coatings (n-vinyl-2-pyrollidone, methyl methacrylate). The thickness of the frost grown on the water-absorbing coating was found to be 10 to 30% lower than that grown on a similar bare aluminum plate after two hours of growth. The surface temperature of the frost was measured by an infrared thermometer and the temperature of the frost surface grown on the water-absorbing coating was found to be lower than that grown on the bare aluminum.

O'Neal *et al.* (1997) investigated the effect of a hydrophobic coating on frost accumulation and duration of the defrost cycle for an aluminum heat pump evaporator. Two coatings, a silicone-based polymer and an acrylic-based coating, were compared against bare aluminum. Contact angles were measured on a sessile droplet of 30 mm^3 volume. The two coated heat exchangers, along with the bare one, were tested in a heat pump to determine the defrost cycle and water accumulation. The silicone-coated evaporator had a longer cycle time for 2 out of the 3 tests and collected less condensate for 2 out of 3 test; however, the test that had the shorter cycle time did not correspond to the test that collected the most condensate. No local measurements of frost accumulation, density or thickness were presented in this study.

1.10 Closure and Objectives

The effect frost has on the performance of an evaporator depends inherently on properties of the frost layer which are difficult to measure: thickness, density, and conductivity. Until recently, frost evolution has only been studied as a function of environmental parameters. Frost properties are correlated with environmental parameters such as substrate and air temperature, absolute humidity, and airflow rate. Seki *et al.* (1984), Dyer *et al.* (2000) and Okoroafor and Newborough (2000) report that frost properties are a function of the substrate on which the frost is deposited. There have been several studies conducted on the condensation period as a function of substrate; however, the focus of these earlier studies has been primarily empirical, and the authors pay little attention to the evolution of the water distribution. Additionally, the freezing of condensate as it pertains to frost formation has never been carefully investigated in relation to the interfacial properties of the substrate. The majority of early and mature frost growth studies are for a single substrate and typically little or no information was presented on the preparation of the surface of the substrate.

The dependence of frost properties on the substrate contact angle for identical environmental conditions indicates that frost properties are a function of more than just the environmental parameters. The objective of this study is to determine how frost properties are altered by the substrate. It is proposed that the role of the substrate is quantified under the capillarity approximation, a well-established classical theory from the field of physical chemistry (MacKenzie 1997). The objective to determine the interaction between the substrate and frost layer will be achieved by carefully examining the evolution of the frost layer on substrates with different contact angles. The evolution

consists of condensation, freezing, early growth, and mature growth, see Fig 1.2 where a flow chart for the research presented in this study is depicted. The understanding provided may lead to methods to decrease the effects of frost in refrigeration systems.

In Chapter 2, the experimental apparatus and procedures used in this study are detailed. The following chapters are arranged so that the significant events which occur during frosting from inception to mature growth are examined in the order which they naturally occur. The early stage of vapor deposition is examined and compared to classical nucleation theory to examine the transition from condensation frosting to ablimation frosting, and the environmental conditions under which condensation frosting occurs is determined in Chapter 3. In Chapter 4, the condensation period is examined for several different substrates to determine the effect that the substrate contact angle has on the condensate distribution. Through the use of high-speed imaging, the freezing differences on hydrophilic and hydrophobic substrates are examined in Chapter 5, and the morphology created during freezing is described. Chapter 6 contains measurements of frost properties and observations of the early and mature growth characteristics as a function of substrate contact angle. In Chapter 7, the mechanism responsible for the differences in frost properties, (thickness, density and conductivity) is explained and a frost model is used to predict the measured trends. Also, the effect that the condensate distribution has on conductivity is examined as a function of substrate temperature. In Chapter 8 the contributions and significance of this work are summarized, and recommendations for future research are detailed. The accompanying appendices contain the substrate cleaning procedures and the program listing for the numerical model used in Chapter 7.

Table 1.1 Flat plate channel flow frost growth trends (Dyer *et al.* 2000)

	Frost Properties		
Environmental Conditions	Growth Rate	Density	Conductivity
Increasing Humidity	⇑	⇑	⇑
Increasing Reynolds #	little effect	⇑	⇑
Increasing Substrate Temp	⇓	⇑	⇑ ⇓*
Increasing Air Temp	⇓	⇑	⇑
Increasing Time	$t^{-0.5}$	⇑	constant

*Discrepancy in the Literature

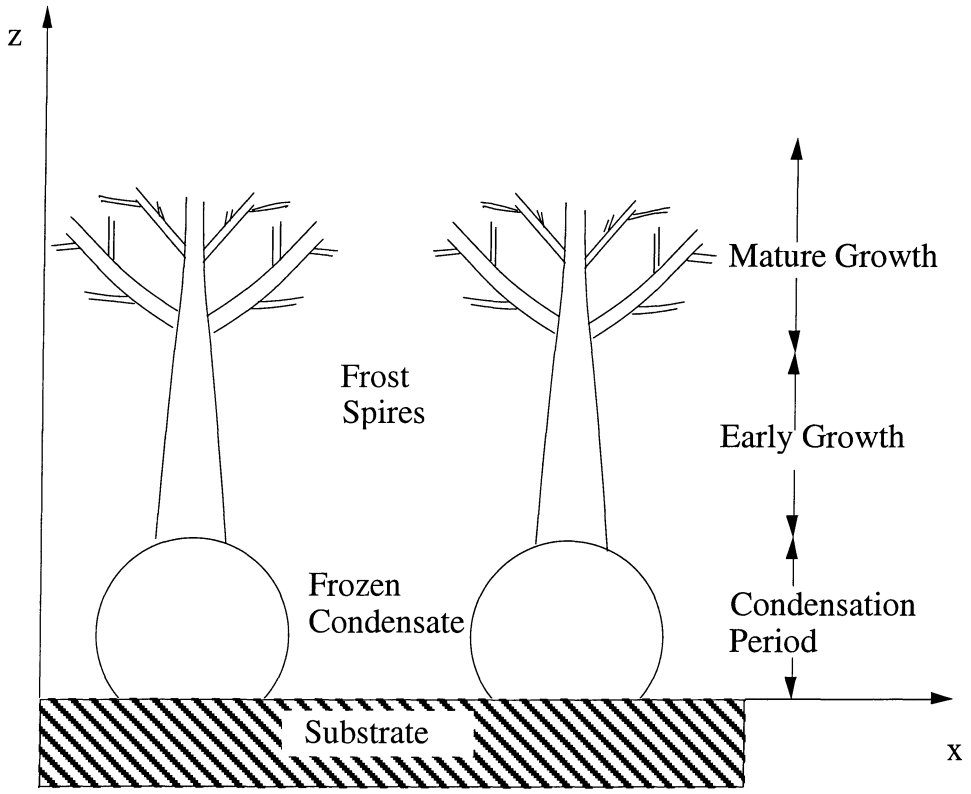

Figure 1.1 Schematic of frost growth periods on a hydrophobic substrate

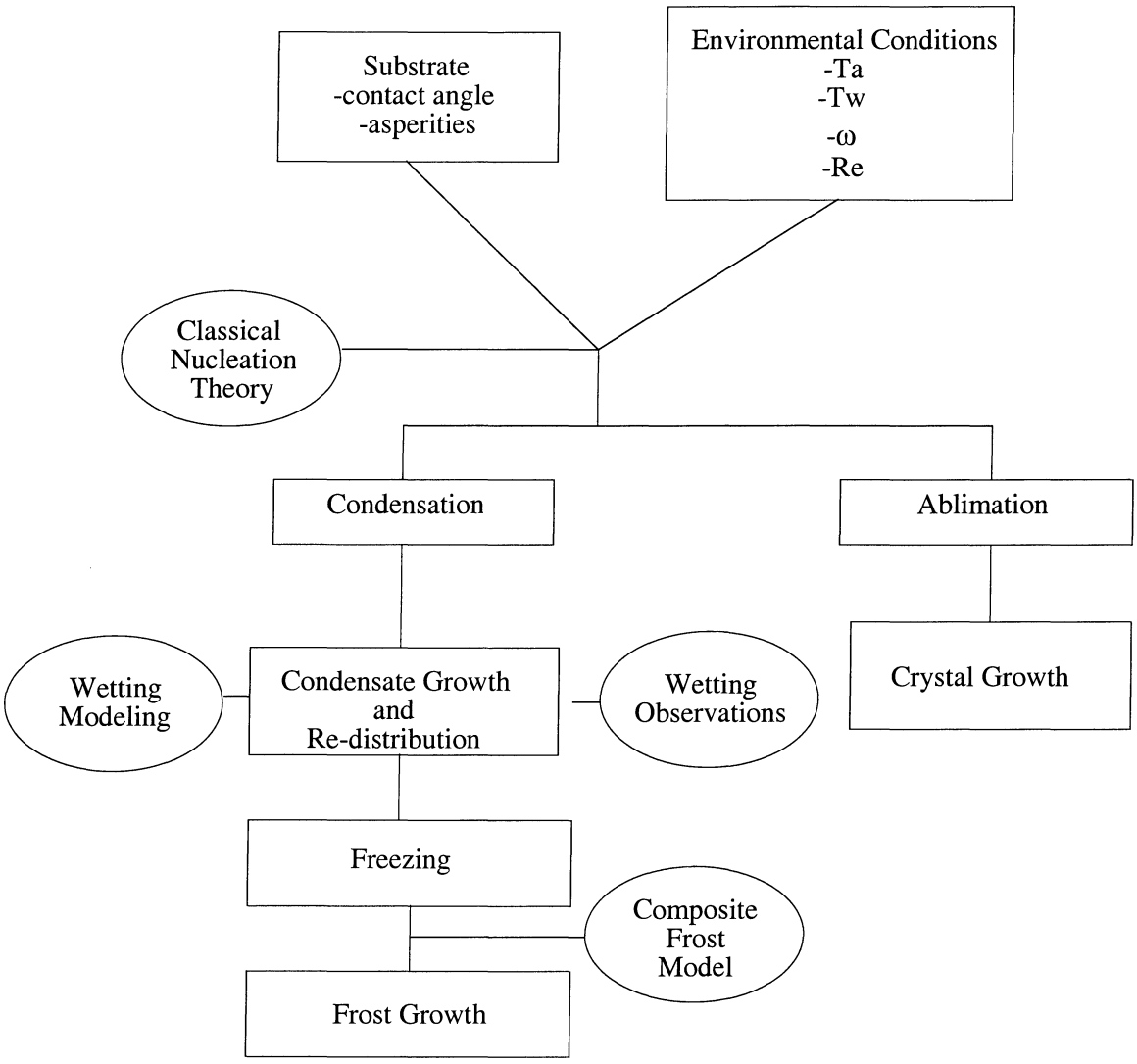

Figure 1.2 Research flow chart

2 Experimental Apparatus and Procedure

2.1 Introduction

Two separate experimental apparatus were used in this investigation. One apparatus, which will be referred to as the "macroscopic" experimental apparatus, was used to obtain quantitative frost height and mass deposition information as the frost thickness grew to 5 mm (the mature growth period). A second apparatus, which will be referred to as the "microscopic" experimental apparatus, was mounted on the stage of a confocal microscope and used to obtain quantitative information regarding condensation, freezing and early frost growth. The macroscopic experimental apparatus and procedure are described in Section 2.2 and 2.3 respectively, and the microscopic experimental apparatus and procedure are described in Section 2.4 and 2.5. There are subtle differences in experimental procedure for different experiments, but these will be detailed in Chapters 3 and 4 where they are pertinent. The substrates used in this study are examined in Section 2.6.

2.2 Macroscopic Experimental Setup and Measurement Uncertainty

The macroscopic experiments were conducted in a closed-loop wind tunnel which was equipped with air temperature, humidity, and flow-rate control. This wind tunnel was built for evaporator testing by Davis (1996) and was adapted for laminar channel frost studies by Storey (1997). A description of the apparatus, similar to what is presented here was provided by Dyer *et al.* (2000). Before reaching the test section, the air flowed through a set of screens and honeycombs and a 4:1 contraction. The test channel was 12.7 mm high by 50.8 mm wide. A flow development length of 632 mm (31

hydraulic diameters) preceded the test section. The turbulence intensity was measured by means of a hot wire anemometer to be below 2.5% at a velocity of 1 m/s. The temperature and concentration boundary layers began to develop at the beginning of the test section, but they did not become fully developed in the test section. The upper wall of the wind tunnel test section was made of clear acrylic to allow optical access. The inlet air temperature was measured using an array of either three or five thermocouples, and the bulk relative humidity was measured using a capacitance-film sensor. The air flow rate was measured in the return pipe, using an ASME standard orifice plate (Storey 1997). A schematic of the test channel is shown in Fig. 2.1.

During an experiment, frost deposited on the lower wall of the test section which consisted of a 3.2 mm thick copper plate covered by the substrate being tested. The test substrate was held against the copper plate by the wind tunnel walls, and thermal paste was used to insure thermal contact. Grooves were machined into the copper plate to allow the flush mounting of 10 type-T thermocouples which were used to measure the substrate temperature. Across the span of the test section, the temperature was within the uncertainty of the data acquisition system, but along the streamwise direction (250 mm), the difference of these thermocouples was a maximum of 3°C. The lower wall of the test section was cooled by intimate contact with an aluminum block, through which a chilled ethylene glycol-water mixture circulated.

The frost thickness was measured optically using a CCD camera to record the reflection of a laser sheet directed toward the frost surface. In order to create the laser sheet, a 15 mW Helium-Neon laser and two cylindrical lenses were used. A schematic of the arrangement is shown in Fig. 2.2. This instrumentation was developed by Storey and

Jacobi (1999). They report that the uncertainty in frost thickness was between ±100 and ±200 μm depending of the conditions of the experiment and time. The uncertainty was larger in the early growth period because of the non-uniformity of the frost surface.

The mass of frost was measured by removing a 51 mm x 101 mm section of the substrate and weighing the substrate and accumulated frost. The net weight was recorded after the substrate had dried. The section of frost removed was located 75 mm to 176 mm downstream from the leading edge. The uncertainty in the measured frost mass per unit area was below ± 5% in all cases. The uncertainty in the density measurements depended on the thickness and the mass per unit area. The maximum uncertainty in frost density, 8%, occurred at the minimum frost thickness measured which was 1.47 mm. At a frost thickness of 3 mm, the uncertainty in density was 6%. Since the uncertainty was dependent on frost height, most water vapor deposition data will be presented as mass per unit area; however, when density is reported the uncertainty will immediately follow.

Twenty readings from each instrument were acquired and averaged (a period of approximately 30 seconds). The frost surface images were acquired at 500 second intervals. Conditions (except for the transient cool down of the substrate) were held constant during the course of an experiment; however, there were small variations in temperature and humidity depending on the conditions of the test. The average values of the 2σ variation in each of the control variables for all tests were: air temperature ±0.8°C, plate temperature ±0.8°C, Reynolds number in the test channel ±2.4%, and relative humidity ±2% RH (Storey and Jacobi 1999). The ranges and uncertainties of these parameters are reported in Table 2.1. It should be noted that during an experiment the hydraulic diameter of the test section decreased as the frost thickness increased. The

subsequent change in Reynolds number was still within the range over which, according to Storey and Jacobi (1999), there was no influence of Reynolds number on frost thickness. The thermocouples used were calibrated in an isothermal bath.

2.3 Macroscopic Experimental Procedure

Each test in the macroscopic test facility was initiated by setting the wind tunnel inlet air temperature, humidity, and velocity and allowing the system to reach steady state, which required approximately two hours. A chiller system was used to cool the test substrate; however, the chiller glycol-water mixture bypassed the test surface until the start of the test. The laser and optics were arranged so that a narrow sheet spanned the test section, and the camera was fixed and focused to provide the desired field of view. Once the optical system was set up, several images of a machined aluminum block were recorded to calibrate the images acquired during the experiment. The calibration images were analyzed by plotting the intensity profile perpendicular to the test substrate (Storey 1997).

After the environmental parameters reached steady state and the calibration images were recorded, the substrate was cleaned with ethyl alcohol and a soft cloth. The test was initiated by opening the valves that allowed the chilled ethylene glycol-water mixture to circulate under the test substrate. The data acquisition systems were then immediately started. At the end of a test, part of the substrate was removed and weighed. The substrate was again weighed after all of the deposited water had evaporated.

2.4 Microscopic Experimental Setup and Measurement Uncertainty

Details of the microscopic facility are presented by Dyer *et al.* (2000), and are repeated here with some clarifications. The microscopic test section rested on the stage

of a Scanning Confocal Microscope (SCM) and consisted of an open-loop wind tunnel with air temperature, humidity and airflow rate control. The test-section flow area was 3 mm by 18 mm. Before entering the test section the air flowed through a temperature-conditioning section over 25 hydraulic diameters in length, and through 3 screens and a 5.25:1 contraction, see Fig. 2.3. Development of the temperature and concentration boundary layers began at the beginning of the test section, but they never became fully developed. The velocity boundary layer was developing throughout the test section as well. The circulation of an ethylene-glycol water mixture through passages under the wind tunnel kept the wind tunnel at a constant temperature (the wind tunnel was made of aluminum). The standard deviation of the air temperature before entering the test section was typically below 0.2°C during the duration of a constant-substrate-temperature experiment.

Substrate cooling was provided by boiling liquid N_2 and pumping the vapor through a heat exchanger in the test cell that was in good thermal contact with the substrate. A PID controller kept the temperature of the substrate constant during and experiment. The standard deviation of the substrate temperature during an experiment was typically less than 0.5°C. A layer of insulation was attached to the sides of the test cell to isolate it from the rest of the wind tunnel. Medical quality air was supplied to the wind tunnel from a compressed air tank. The moisture content of this air was 8-10 ppm which corresponds to a dew point of –61°C. The humidity of this air stream was increased by dividing the air stream into two streams and bubbling one stream through water at room temperature. The humidity was adjusted by altering the percentage of the total flow rate bubbled through the water. Sealing of the wind tunnel was confirmed by

two rotometers placed so that the airflow could be measured before it entered and after it exited the wind tunnel.

Optical access was obtained through a glass window mounted flush with the wind tunnel walls above the test section. Images of the frosting process were recorded via a frame-accurate S-VHS video recorder at 30 frames per second either through the Scanning Confocal Microscope or through a CCD camera mounted in the eye-tube of the microscope. High-speed images of the freezing process were recorded at up to 8000 frames per second for two seconds through the eye tube with a second CCD camera. The field of view of the microscope was calibrated by imaging NIST-traceable 10 μm borosilicate micro-spheres with a standard deviation in diameter of 1.4 μm. A minimum of 10 spheres were imaged and measured to determine the scale of the acquired images. The data for the calibration of both CCD cameras is presented in Tables 2.2 and 2.3 while the internal calibration of the SCM was checked in Table 2.4. The internal calibration of the SCM was used for convenience since it was automatically recorded on the images and was within a standard deviation of the calibration done with the 10 μm balls.

Air temperature was measured before and after the test cell by two 36 gauge, type-E thermocouples. The substrate temperature was measured by a 36 gauge, type-E thermocouple mounted flush to the test cell below the substrate. Ten temperature measurements were averaged and recorded at 5 Hz (the sampling rate was 50Hz). The humidity of the air was measured upsteam of the wind tunnel in a 2-liter plenum with a capacitance-film sensor. The airflow rate was measured with a rotometer. Heat flux was measured with a heat flux sensor. The response time of the heat flux sensor was 0.72 seconds for a 62% rise in heat flux. The uncertainties in the control variables were: temperature measurements ±0.2°C or ±0.5°C depending on the study, relative humidity

±2% RH, Reynolds number ±5% and heat flux ±10%. The range and uncertainty of the parameters measured during the ablimation study are presented in Table 2.5 while those measured in the condensation and early growth studies are presented in Table 2.6.

2.5 Microscopic Experimental Procedure

In the microscopic tunnel, all environmental parameters were held constant during the duration of an experiment except substrate temperature during the condensation versus ablimation study where the substrate temperature was continually decreasing. The surface of the test cell was coated with a thin layer of thermal paste. The cleaned substrate was then placed on the test cell, and the assembly was inserted into the wind tunnel. The wind tunnel was checked for leaks and positioned so that the field of view of the microscope was just upstream of the location of the thermocouple recording the substrate temperature, approximately 19 mm from the start of the thermal/concentration boundary layer. This position was also expected to be the coldest point on the substrate, since this was the location where the vapor N_2 entered the heat exchanger and flowed counter to the wind tunnel test air. Once steady-state was reached, the VCR was turned on and the data acquisition system was started. The flow through the wind tunnel was switched from the dry nitrogen to an air stream with the desired humidity.

2.6 Surface Characterization

In order to make these experiments as repeatable as possible, the surfaces used in this study underwent a cleaning procedure prior to a one-time use and disposal (the only substrate reused was the large glass slide used in the macroscopic-wind tunnel) or prior to

measuring the contact angle and average surface roughness. The cleaning procedure varied depending on the substrate and all cleaning protocols are detailed in Appendix A.

The degree to which a liquid, placed on a solid, covers the solid is defined as the wettability. The wettability can be quantified through measurement of the contact angle of a droplet placed on the solid. The contact angle is a direct manifestation of the relative magnitudes of the interfacial tensions between the liquid and solid, solid and vapor, and vapor and solid. A schematic of the direction with which the interfacial tensions act on the contact line of a droplet on a flat surface is given in Fig. 2.4. In order to maintain equilibrium in the horizontal direction, the three forces must balance, which gives Young's Equation.

$$\sigma_{lv} \cos\theta = \sigma_{sv} - \sigma_{sl} \tag{2.1}$$

The equilibrium contact angle can therefore be calculated from knowledge of the interfacial surface tensions. Unfortunately, values of the solid-vapor and solid-liquid interfacial tension are difficult to measure (Carey 1992).

The roughness of the substrate affects the contact angle. Larger surface roughness decreases the contact angle on a given substrate. The relation between the contact angle on a flat surface and that on a rough surface is given by

$$\cos\theta_R = \gamma \cos\theta \tag{2.2}$$

where γ is the ratio of the actual surface area on a rough surface to the area of a ideal, flat surface. Since γ is greater than one, the contact angle on the rough surface will always be smaller than that found on a flat surface. Carey (1992) gives a proof of the effect of roughness on contact angle based on the change in Helmholtz free energy of the system caused by the roughness.

The advancing and receding contact angles of all substrates used in this study were measured by observing an approximately 3-mm-diameter water droplet placed on the substrate at room temperature, see Fig. 2.4. Advancing contact angles were measured by slowly adding water to the droplet via a thin needle. The advancing contact angle was recorded as the largest angle possible when adding water to the droplet prior to the contact line releasing and advancing. Receding contact angle measurements were recorded as the smallest angle achievable when removing water from the droplet prior to the contact line releasing and receding. Contact angles were measured either by a goniometer or by imaging the droplet during the addition and removable of water and then processing the images, see Fig. 2.5. Typically, 10 or more measurements were recorded. A table of substrates and the contact angles measured along with the standard deviation of the measurements is supplied in Table 2.7.

In order to further characterize the surface being tested, surface profilometry was performed over a 5 mm length on some of the substrates. The minimum measurable surface roughness by the technique used was 10 Å. The average surface roughness is recorded in Table 2.8, and a typical plot of the surface profile is given in Fig. 2.6.

Table 2.1 Macro-test parameters, range and uncertainty

	Range	Uncertainty
T_w	-20.1 to -11.9°C	0.2°C
T_∞	23.1 to 19.6	0.2°C
RH	70.7 to 50.1 % RH	2% RH
ω	12.5 to 8.3 g/kg	0.3 g/kg
δ	0 to 4.7 mm	0.15 mm
$\sqrt{\tau}$	0.051 to 0.388	8%
Γ	0.05 to 0.37	0.01
Re	1012 to 1561	2.40%

Table 2.2 CCD Camera calibration data

	10X	20X	40X	100X
pixel /μm	0.55	1.03	2.12	5.28
Std. Dev.	0.070	0.149	0.257	0.355

Table 2.3 High speed CCD camera calibration data

	10X	20X	40X	100X
pixel /μm	0.68	1.35	2.75	7.31
Std. Dev.	0.101	0.115	0.221	0.516

Table 2.4 SCM calibration data

	10X	20X	40X	100X
pixel /μm	1.56	2.99	5.49	14.57
Std. Dev.	0.241	0.311	0.251	0.397
SCM Calib. Pixel/μm	1.41	2.84	5.64	14.19

Table 2.5 Micro-test parameters, range and uncertainty-ablimation study

	Range	Uncertainty
T_w	-56 to –25°C	0.5°C
T_∞	-18 to -16°C	0.2°C
RH	47 to 93%	2% RH
ω	0.013 to 0.310 g/kg	0.5 to 9.7 μg/kg
Re_{Dh}	550 to 750	5%

Table 2.6 Micro-test parameters, range and uncertainty

	Range	Uncertainty
T_w	-27 to –5°C	0.2°C
T_∞	-16 to 17°C	0.2°C
RH	20 to 80%	2% RH
ω	1.05 to 10.8 g/kg	0.3 g/kg
Re_{Dh}	340 to 420	5%
q"	500 to 2000	10%

Table 2.7 Contact angle measurements

Substrate	Advancing	Std. Dev.	Receding	Std. Dev.
Glass (us cleaned)	<10°	N/A	<10°	N/A
Glass	40°	6.3°	29°	4.6°
Silicon wafer	<10°	N/A	<10°	N/A
OTS on Silicon	99°	5.3°	74°	8.6°
Coated Al	55°	1.6°	38°	1.1°
Kapton tape	67°	3.6°	32°	4.8°
Al (reference)	92°	1.5°	53°	6.7°
PTFE on steel	106°	3.5°	74°	2.8°
PTFE tape	103°	1.8°	84°	3.4°

Table 2.8 Average surface roughness

	Average Roungness, R [Å]
Glass (ultrasonically cleaned)	160
PTFE	3108
Aluminum	3021
Kapton	378

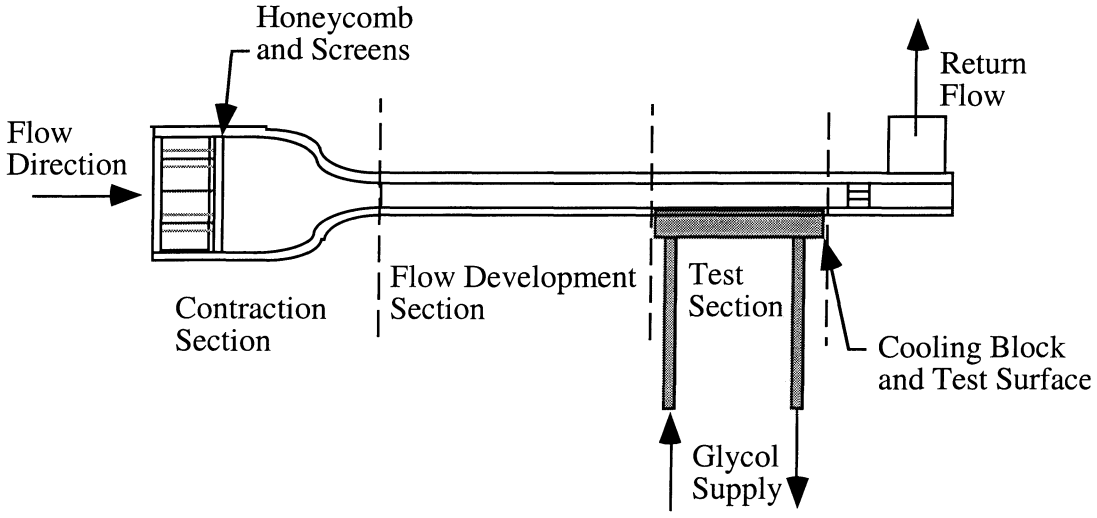

Figure 2.1 Macro-wind tunnel (Storey 1997)

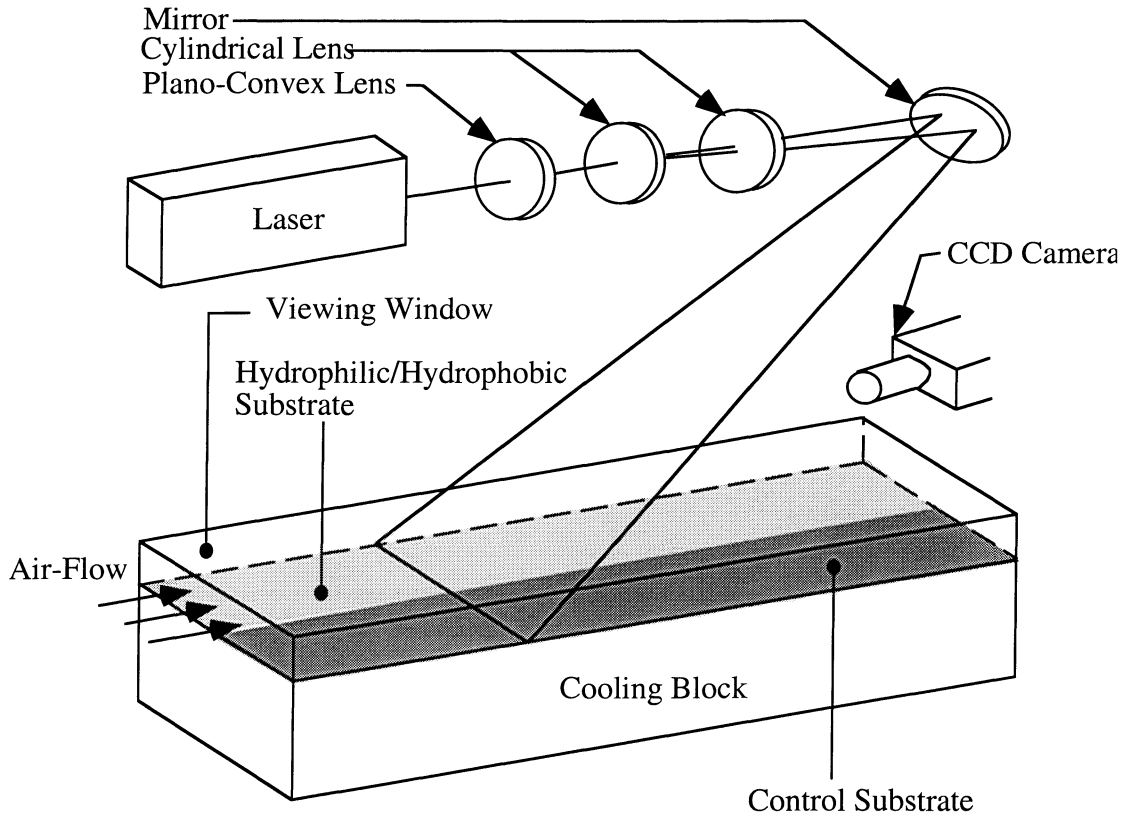

Figure 2.2 Macro wind tunnel test section and frost height measurement optics (Dyer *et al.* 2000)

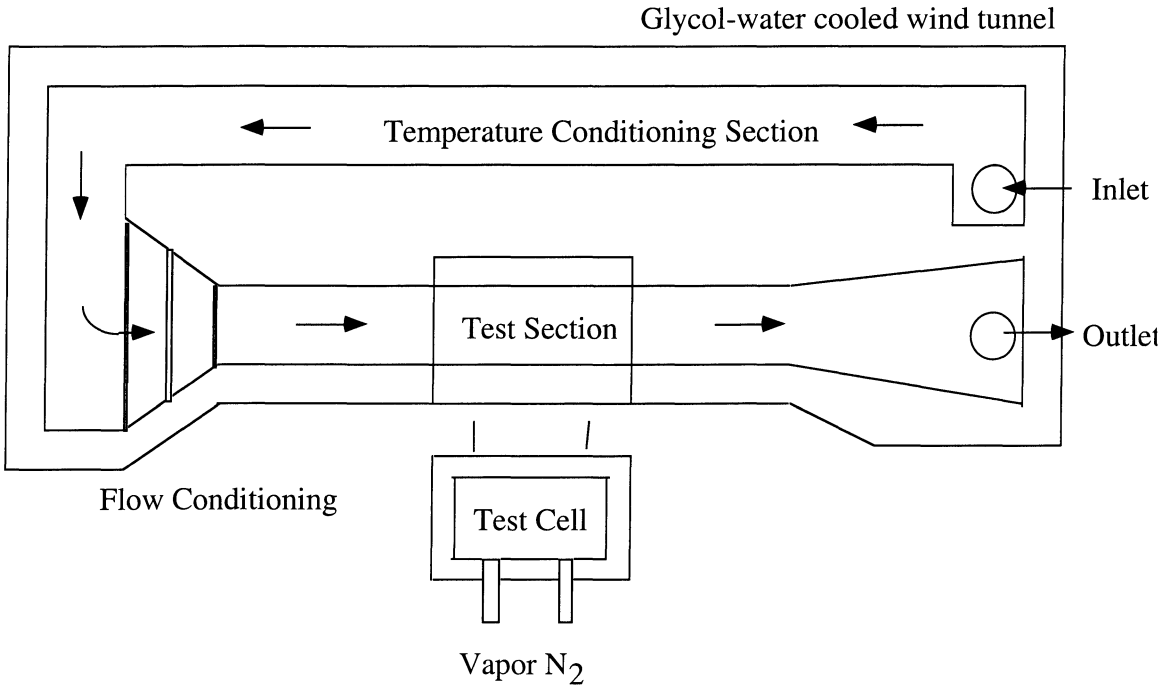

Figure 2.3 Micro-wind tunnel (Dyer *et al.* 2000)

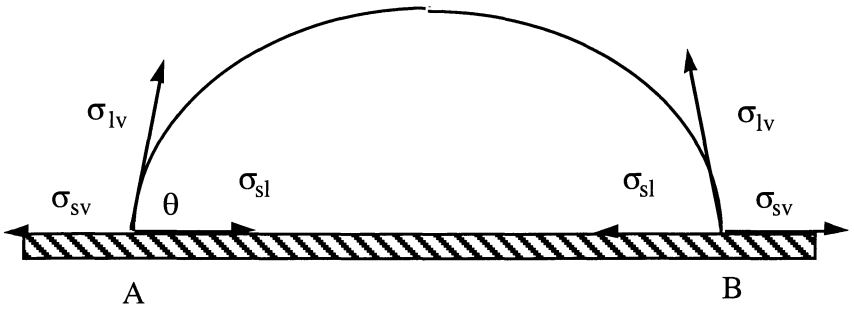

Figure 2.4 Schematic of contact angle and forces on a droplet

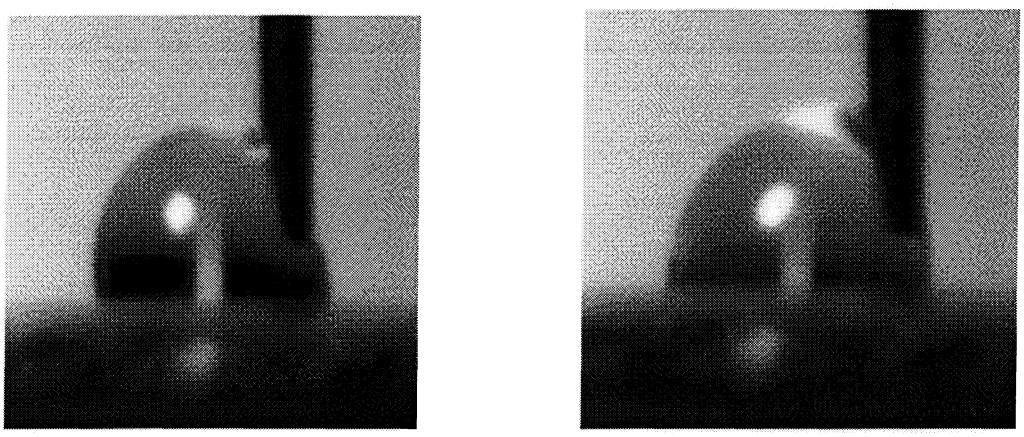

a b

Figure 2.5 Contact angle measurement on PTFE substrate: a) advancing and, b) receding

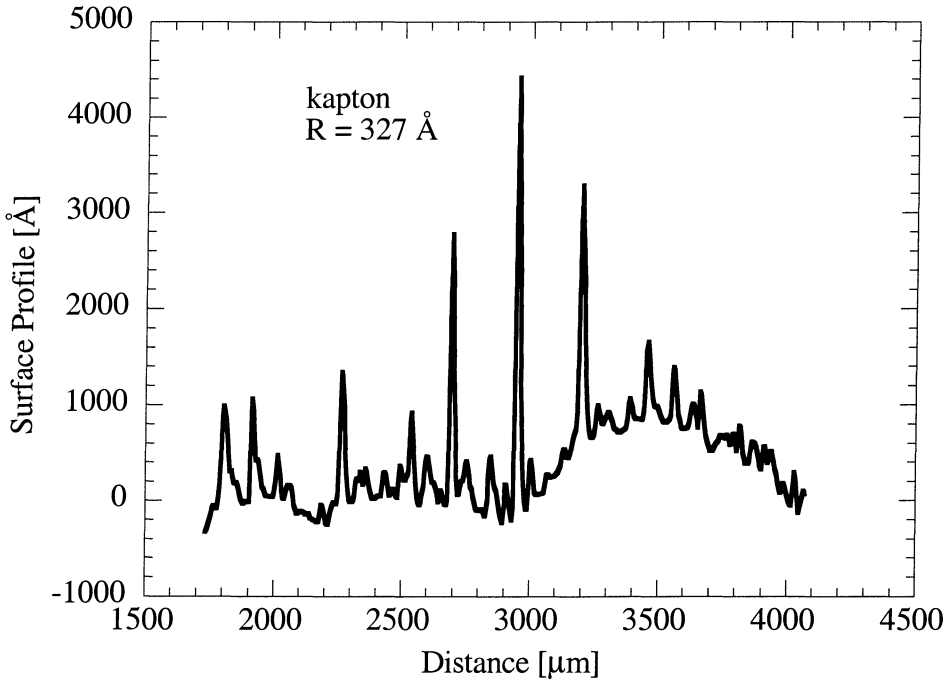

Figure 2.6 Surface profile of kapton substrate

3 Transition from Condensation to Ablimation Frosting

3.1 Introduction

As described in the introduction, there are two scenarios for the deposition of frost. The first was labeled "condensation frosting" while the second was labeled "ablimation frosting". The scenarios are labeled to distinguish the way in which frost growth is initiated. Experiments were conducted to determine the demarcation in environmental conditions which favors one frost initiation scenario over the other.

The experiments were conducted with an average air velocity of 1.5 m/s. The air temperature approaching the test cell was approximately -16°C during vapor deposition. The temperature of the substrate was continually decreasing in this experiment while the humidity ratio of the approaching air was constant. A typical temperature history is given in Fig. 3.1. The substrate cooling-rate was approximately 0.025°C/s during deposition. The cooling rate was kept low so the system stayed near thermodynamic equilibrium. The microscope was position approximately 19 mm from the leading edge of the test section over the thermocouple. This region was expected to be the coldest region on the substrate because the fluid cooling the test cell entered at this location. A glass cover slip, 0.18 mm thick, was used as the substrate in all of these experiments. The average roughness was approximately 160 Å. A typical profile of the surface is shown in Fig. 3.2.

3.2 Experimental Observations

Two deposition scenarios were observed: (i) liquid water condensing on the substrate, and (ii) deposition on the substrate directly as ice, ablimation. At incipience, it was impossible to differentiate between ablimation and condensation because of the small size of the child phase, see Fig. 3.3 (a). However, the growth characteristics of the child phase indirectly reveal the phase of the initial deposition. If liquid were initially deposited, evaporation of unfrozen droplets was observed when freezing occurred in an adjacent droplet. Recall that the temperature of the substrate in this experiment is continually decreasing. When one droplet froze, the water vapor above adjacent, unfrozen droplets diffused to the frozen droplet, where the vapor pressure of water is lower. Thus, a sudden decrease in the size of the deposits indicated that water was initially deposited, see Fig. 3.3. Coalescence of droplets was another indication that water was initially deposited, see Fig 3.4. When the initial deposition was ice, the ice continued to grow until crystals were observed and the test was completed, see Fig. 3.5. The results of 19 experiments are summarized in Fig. 3.6. The transition from condensation to ablimation frosting is marked by the kink of the dashed line (approximate) occurring between –33°C and –35°C and a humidity ratio of 0.13 g/kg to 0.15 g/kg. Shinagawa *et al.* (1992), found that the transition from condensation to ablimation of pure water vapor occurred at a vapor pressure of 200 Pa, and a substrate temperature of approximately –16°C.

3.3 Ablimation versus Condensation

The following parameters are thought to control the deposition scenarios: degree of saturation, substrate temperature and the contact angle of the deposit (either condensate or ice). The deposition of condensate at substrate temperatures below 0°C can be explained on the basis of macroscopic theory for heterogeneous nucleation developed by Fletcher (1958; 1959). Since 1958, another theory called the diffuse interface nucleation theory of crystal nucleation has been developed; however, there is still debate over which model more accurately describes nucleation (Granasy 1995). The conditions necessary for condensation or direct ice deposition and how different parameters affect the nucleation processes based on *classical* nucleation theory will briefly be discussed.

This theory is based on a nucleation embryo forming over an insoluble nucleating agent, which is considered as a perfectly crystalline spherical particle. In this case the surface imperfections will be considered to act as nucleating agents, and the average surface roughness (160 Å) represents the radius of such a nucleating particle. For a detailed discussion of this theory, refer to Fletcher (1958; 1959) and Turnbull and Vounnegut (1952). On this basis, the rate of heterogeneous nucleation, J, of critical embryos per unit area which can develop into macroscopic droplets or ice crystals is given by an expression of the form (Fletcher 1959)

$$J = A \exp\left(-\frac{\Delta G^*}{k T}\right) \tag{3.1}$$

where A is a kinetic constant, k is the Boltzmann constant, T is the temperature, and ΔG^* is the free energy of formation of critical embryo on a nucleating particle. The free energy of formation of the critical embryo can be expressed as (Fletcher 1958)

$$\Delta G^* = \frac{8\pi\sigma_{12}^3}{3(\Delta G_v)^2} f(m,x) \tag{3.2}$$

where f(m,x) is defined as

$$f(m,x) = 1+\left(\frac{1-mx}{g}\right)^3 + x^3\left[2-3\left(\frac{x-m}{g}\right)+\left(\frac{x-m}{g}\right)^3\right]+3mx^2\left(\frac{x-m}{g}-1\right) \tag{3.3}$$

$m=\cos(\theta)$, and

$$g = (1+x^2-2mx)^{1/2} \tag{3.4}$$

The critical radius of the embryo is given by the expression

$$r^* = -2\sigma_{12}/\Delta G_v \tag{3.5}$$

where ΔG_V is the free-energy difference per unit volume of the child phase (phase 2) between the child phase and the parent phase (phase 1), and σ is the surface free-energy of the interface between the child phase and parent phase. The embryo (liquid or solid)

forms on the nucleating particle with contact angle θ. If R represents the radius of the nucleating particle (which is the average roughness in this case), then

$$x = R/r^{*} \tag{3.6}$$

Considering a nucleating particle of radius R, the nucleation rate per particle can be expressed as

$$J' = 4\pi R^2 A \exp(-\Delta G^{*} / kT) \tag{3.7}$$

Fletcher arbitrarily chose to associate nucleation with nucleation rates of one embryo per particle per second (J'=1 sec^{-1}). Using this value for J' in Eq. (3.7) and combining it with Eq. (3.2) yields the following expression for the free energy difference

$$\Delta G_v^2 = [8\pi/3]\sigma_{12}^3 f(m,x)/kT[60.1 + 2\ln(R)] \tag{3.8}$$

Here a value of 10^{25} cm^{-2} sec^{-1} for A, is assumed (Fletcher 1958).

In the case of *condensation*, ΔG_v can be expressed in terms of temperature and saturation ratio as (Fletcher 1958)

$$\Delta G_v = (-kT/V_L)\ln(P_\infty / P_L) \tag{3.9}$$

where V_L is the volume occupied by a molecule of liquid water, P_∞ is the ambient vapor pressure and P_L is the saturated vapor pressure over a plane surface of water. Substituting Eq. (3.9) in Eq. (3.8) yields the following expression for the saturation pressure ratio in terms of temperature and contact angle for condensation:

$$\ln(P_\infty / P_L) = \left[\frac{8\pi\sigma_{12}^3 f(m,x) V_L^2}{3(kT)^3 (60.1 + 2\ln(R))} \right]^{1/2} \tag{3.10}$$

The above equation was solved iteratively to compute the pressure ratio as a function of temperature for a particular contact angle. Here the value for σ_{12} for the vapor to liquid interface is assumed to be 75.6 mN/m (Fletcher 1958). Fig. 3.7 shows the variation of pressure ratio with temperature for a water embryo forming on a particle of radius 160 Å (equal to the average surface roughness) with a contact angle of 5°. This figure shows only a weak dependence of pressure ratio on temperature. For a 40°C change in temperature (about 16%), the pressure ratio changes by only 1.1%. This shows the expected result that condensation is possible at any temperature, provided the air is slightly supersaturated. Increasing the contact angle increases the saturation ratio required at a temperature for condensation to occur.

In the case of direct deposition (*ablimation*) of ice, ΔG_v is given by (Fletcher 1958)

$$\Delta G_v = (-kT / V_s) \ln(P_L / P_S) \tag{3.11}$$

where V_s is the volume occupied by a molecule of ice, P_s is the vapor pressure over plane surface of ice. The ratio of the vapor pressures in the above equation can be represented in terms of the degree of supercooling using the following relation

$$\ln\left(\frac{P_L}{P_S}\right) = \alpha \Delta T \tag{3.12}$$

where α has a value of about 0.00972/°C. Here ΔT is equal to (273-T). Substituting Eqs. (3.11) and (3.12) into Eq. (3.8), the relation for the degree of supercooling is obtained:

$$\Delta T^2 = \left[\frac{8\pi\sigma_{12}^3 f(m,x) V_s^2}{3(kT)^3 \alpha^2 (60.1 + 2\ln(R))}\right] \tag{3.13}$$

The above equation was also solved iteratively to obtain the temperature at which direct deposition occurs as a function of contact angle of the ice embryo. Nucleation on R=160 Å, R=500 Å and R—> ∞ is considered. The first two values correspond to the average asperity size and a hypothetical heterogeneous nucleation site, while the third corresponds to a perfectly flat nucleation site. For the latter case, as x—> ∞, the expression f(m,x) becomes independent of x (Fletcher 1959)

$$f(m) = (2 + m)(1 - m)^2/4 \tag{3.14}$$

In Fig. 3.8 the variation of temperature with contact angle for inception of ablimation is depicted. In these calculations the value of σ_{12} is assumed to be 100 mN/m

for the vapor-ice interface (Fletcher 1958). The temperature at which direct deposition occurs drops sharply with increasing contact angle. Unlike the condensation observations, the direct measurement of the ice-glass substrate contact angle is not measurable in these experiments. On the basis of Fig. 3.8 and a nucleating agent of R=160 Å, an ice contact angle of 20^{o} -21^{o} is consistent with the –33° to –35°C ablimation-condensation transition implied by Fig. 3.6.

In Fig. 3.8 it is also shown that larger particles are better nucleating agents (i.e. the temperature at which deposition occurs increases with increasing nucleating particle radius). The effect of contact angle on the temperature for ablimation inception diminishes with increasing embryo radius. It is also shown in Fig. 3.8 that for ablimation to occur at reasonable temperatures, the contact angel between ice and the substrate must be below 30°. In addition to the dependence on nucleating particle radius, any mismatch in the crystallographic structure between the embryo and nucleating particle embryo will cause the embryo to be in a state of elastic strain due to the mismatch in the crystallographic structures (Turnbull and Vonnegut 1952). This strain shifts all of the curves shown in Fig. 3.8 down (Fletcher 1959).

In heterogeneous nucleation, when the air is saturated and cold (below freezing), direct deposition of ice and deposition of water represent two competing processes. Using the above relations for nucleation rates of ice crystals and condensation, the temperature at which these two processes become equal is computed for a condensate embryo contact angle of 5^{o}. The results show that this temperature varies between -10.3°C and -30°C for R=160 Å when the contact angle of ice embryo is varied between 5^{o} and 20^{o}. Fletcher (1959) has proposed activity surfaces representing different regimes

where condensation and direct deposition occur over the typical nucleating substances. The proposed activity surface is for a contact angle of 5° for condensation and 25° for ice.

By knowing the transition temperature between condensation and ablimation, ablimation can be predicted using classical nucleation theory. A value of 21° is used for the contact angle of ice on the glass substrate because that value was shown to predict the transition temperature. The measured surface roughness of 160 Å and the value of 100 mN/m for the surface tension between ice and vapor are used. Values for the pressure difference between ice and liquid at low temperatures are not available; however, the data of Kraus and Greer (1984) which go down to –20°C were used to extrapolate data down to –50°C. The prediction for ablimation is plotted in Fig. 3.9 along with the measured data. The theory is shown to predict the trend of the experimental data.

Shown in Fig. 3.10 is a comparison between the results obtained by Shinagawa *et al.* (1994) and the results found in this study. For pure water vapor the vapor pressure at which ablimation occurred was found to be 4 to 10 Pa greater than that found in this study. The substrate used in their study was a copper substrate. Typically the contact angle for water is much larger on copper than it is on glass. If the same is true for the ice-substrate contact angle, then the observed lower ablimation temperature found in their study for a given vapor pressure would be predicted by classical nucleation theory, see Fig. 3.8. This comparison and explanation is largely speculation since the only information given about their substrate is that it is copper, the surface roughness and water contact angles are not provided. The trends are the similar to those found in this investigation.

The substrates (primarily PTFE and kapton) used in the remainder of this study have a surface roughness much greater than that found on the glass substrate, see Table 2.8. A higher surface roughness would decrease the temperature at which the deposition transitions from condensation to ablimation. However, the differences in the nucleation site characteristics from substrate to substrate make it difficult to predict how the deposition will occur on other substrates. The substrate temperature range investigated throughout the remainder of the study is form –9°C to –28°C, encompassing most of the range where condensation is expected. Homogenous nucleation of water is observed to occur at approximately –40°C (Fletcher 1958).

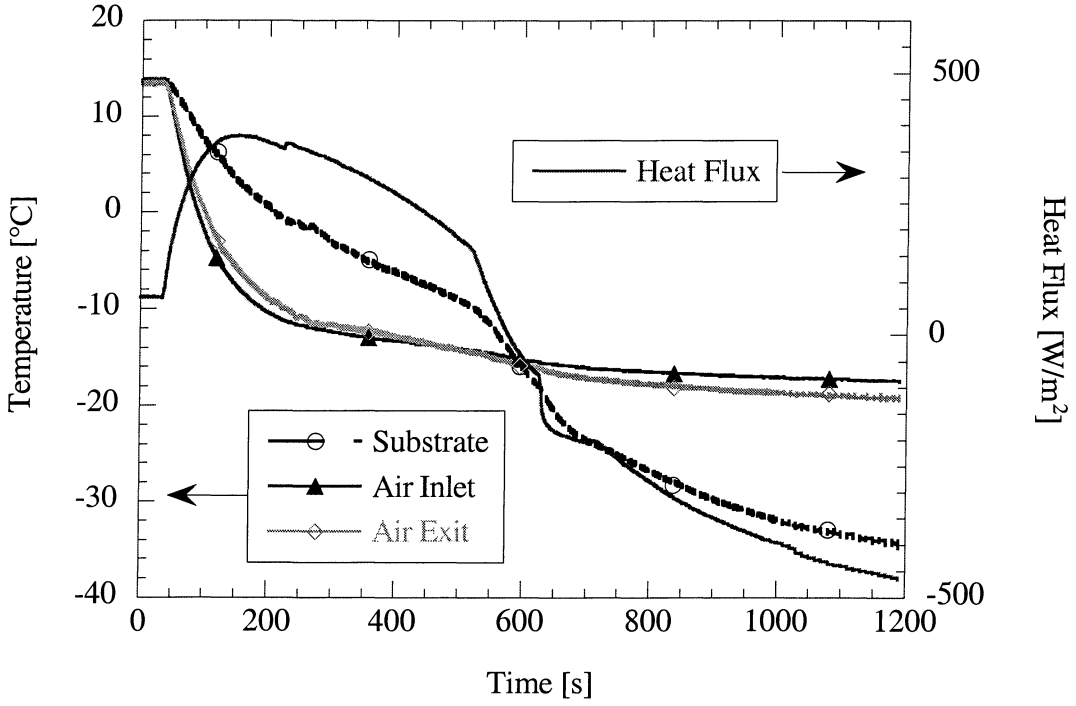

Figure 3.1 Typical temperature and heat flux histories during the ablimation/condensation experiments

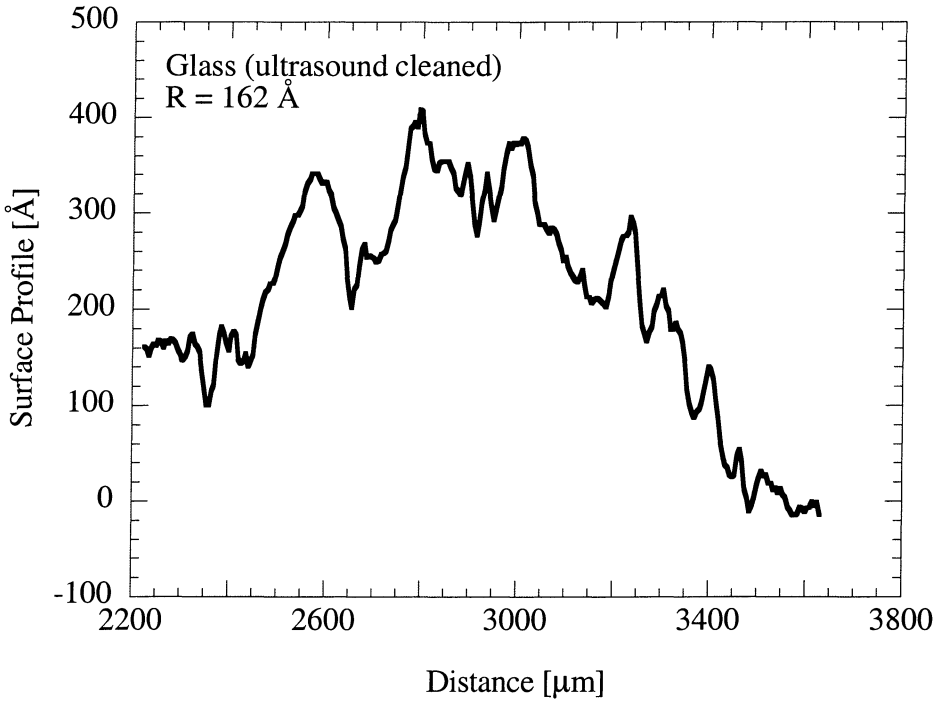

Figure 3.2 Surface profile of the glass substrate obtained with stylus profilometer

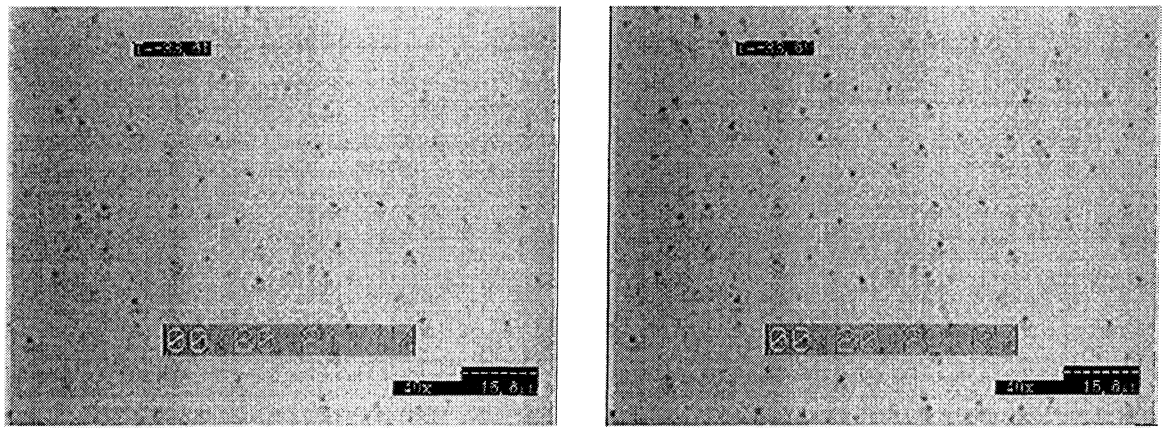

a b

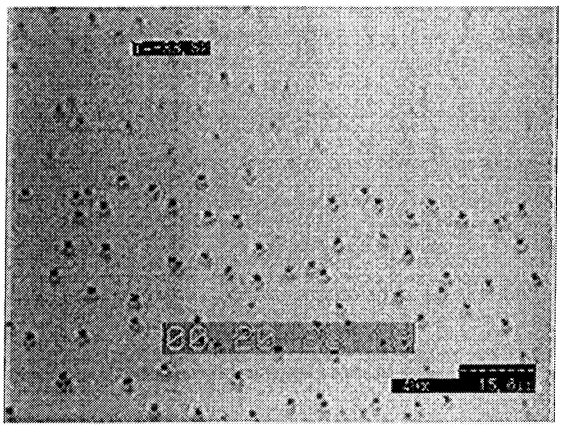

c

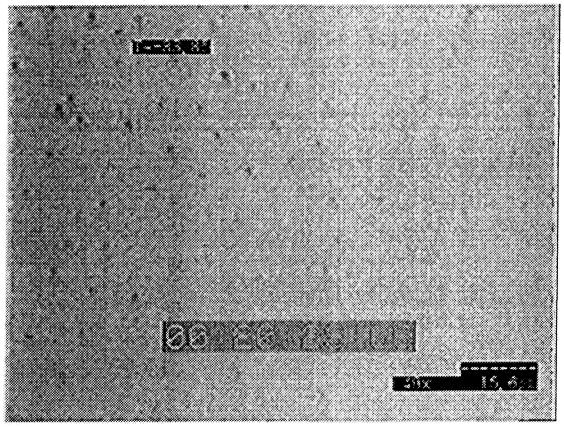

d

Figure 3.3 Initial condensation. Sequence (a), (b), (c), (d) confirms the evaporation of some of the smaller droplets at the instant when a number of droplets freeze T=-30.8°C, ω = 0.1719 g/kg

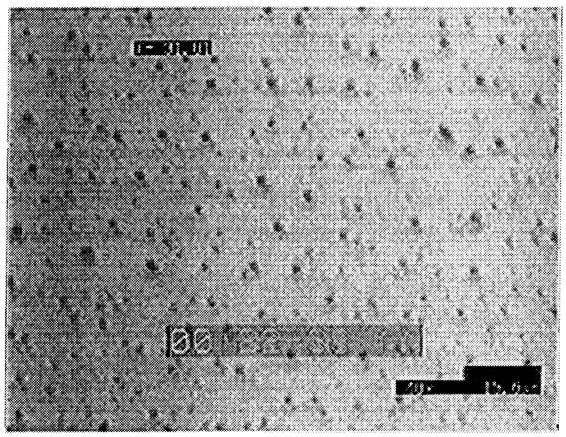

a

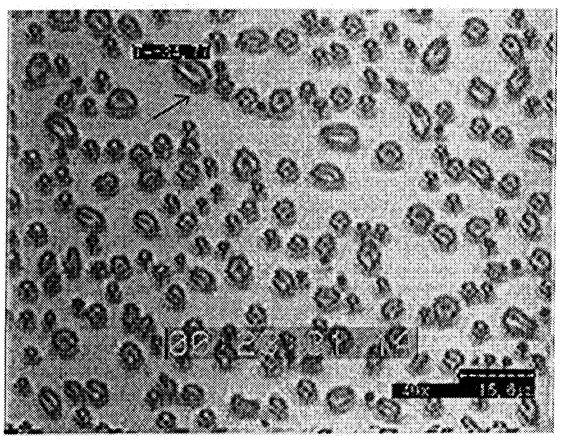

b

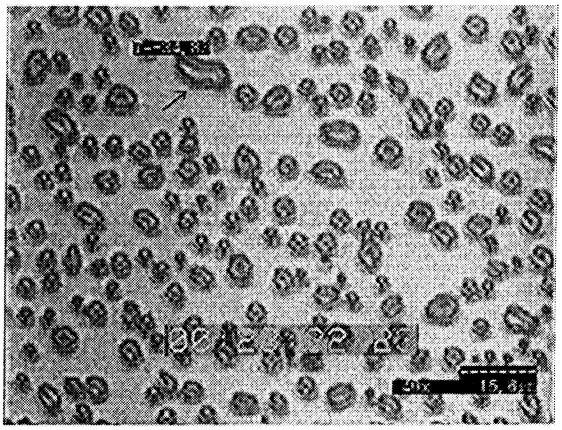

c

Figure 3.4 Droplet coalescence T = -31.2, ω = 0.154 g/k

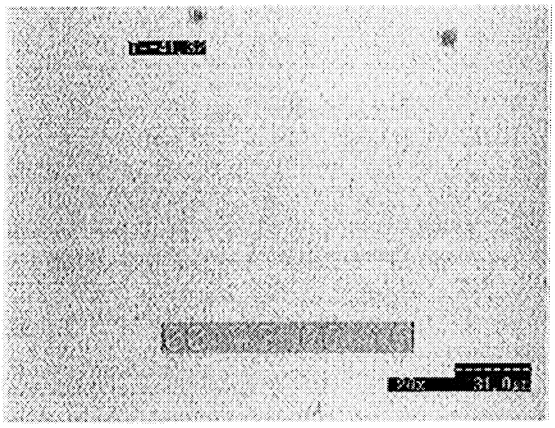

a

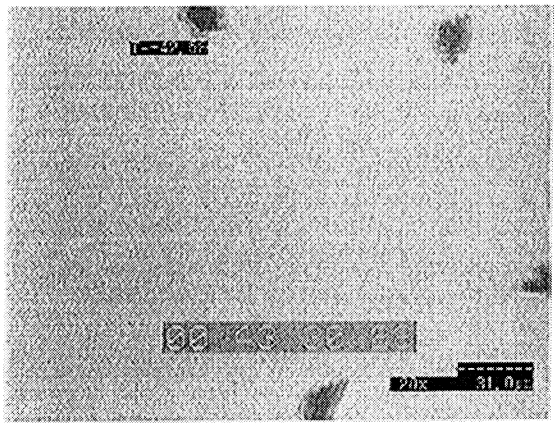

b

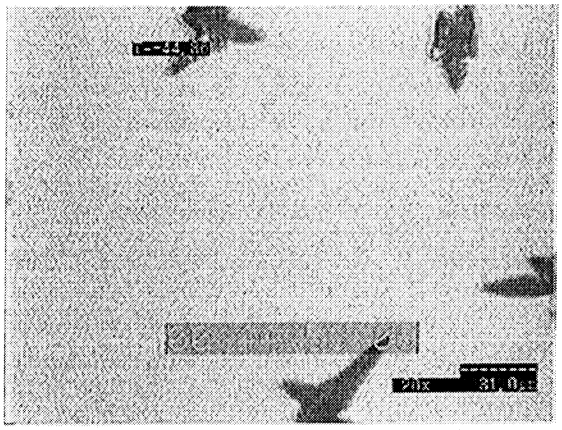

c

Figure 3.5 Ablimation and subsequent crystal growth T = -41.1, ω = 0.051 g/kg

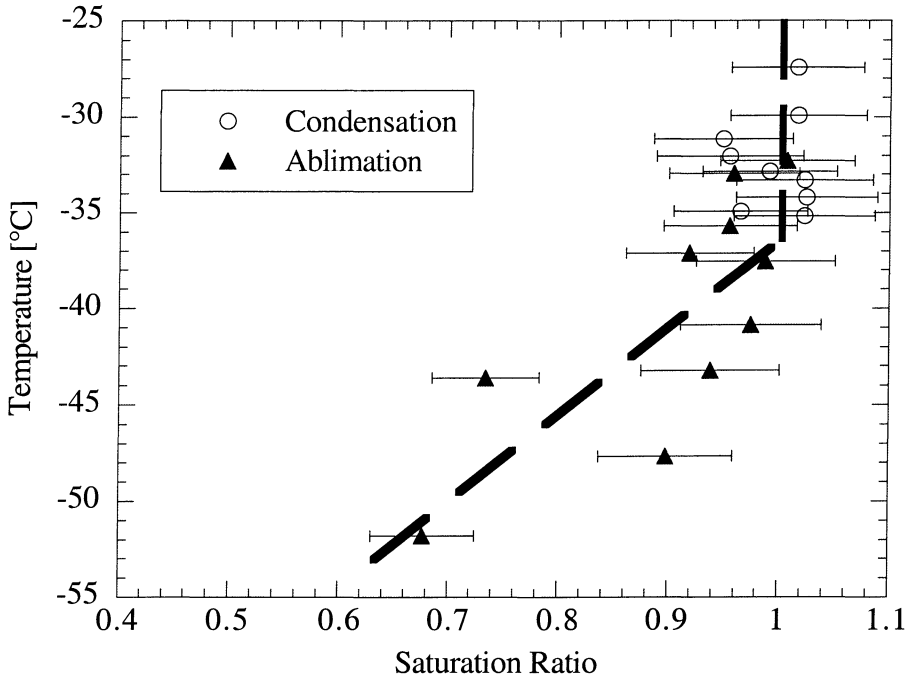

Figure 3.6 Experimentally determined temperature versus saturation ratio for the inception of condensation and ablimation. The dash line delineates the activation boundary inferred from the direct microscopic observation

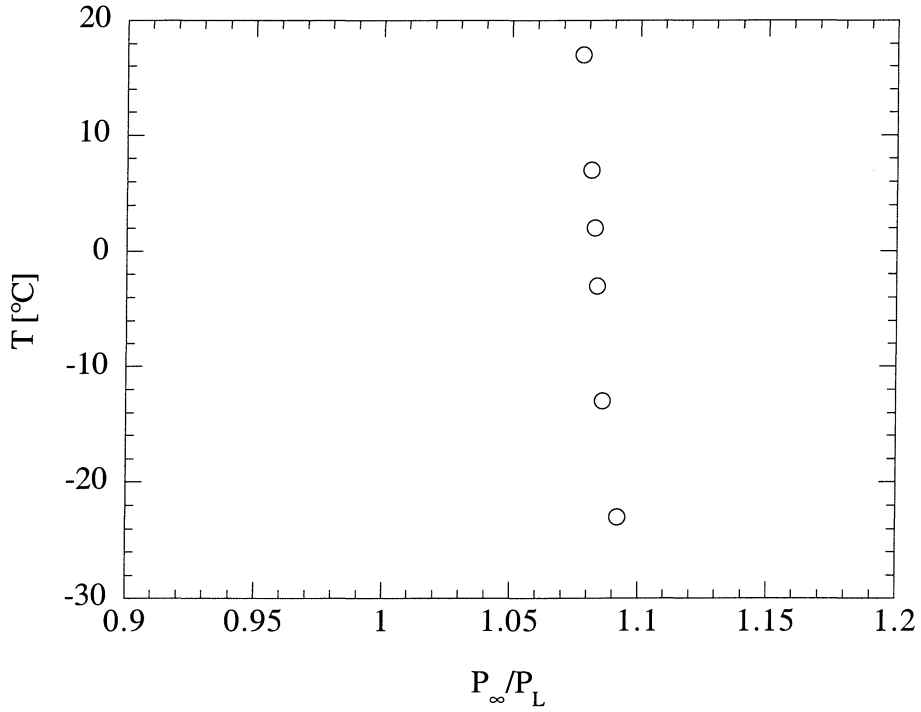

Figure 3.7 Theoretical prediction of the temperature versus saturation ratio (P_∞/P_L) θ =5°, nucleating particle radius = 160 Å

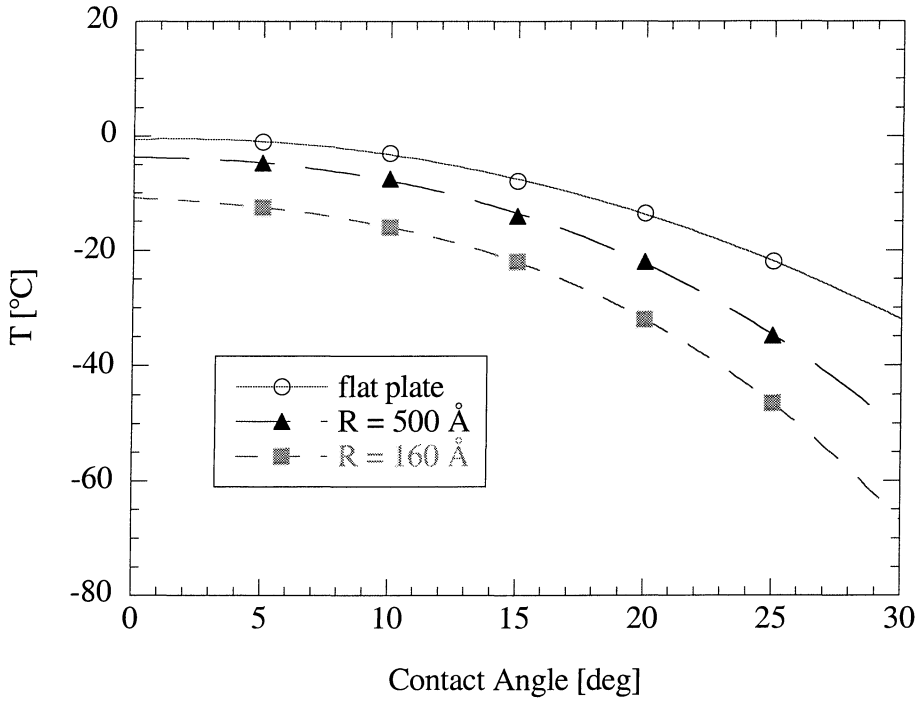

Figure 3.8 Theoretical prediction of the variation of the temperature versus contact angle for the critical ice embryo forming over nucleating particles of different sizes

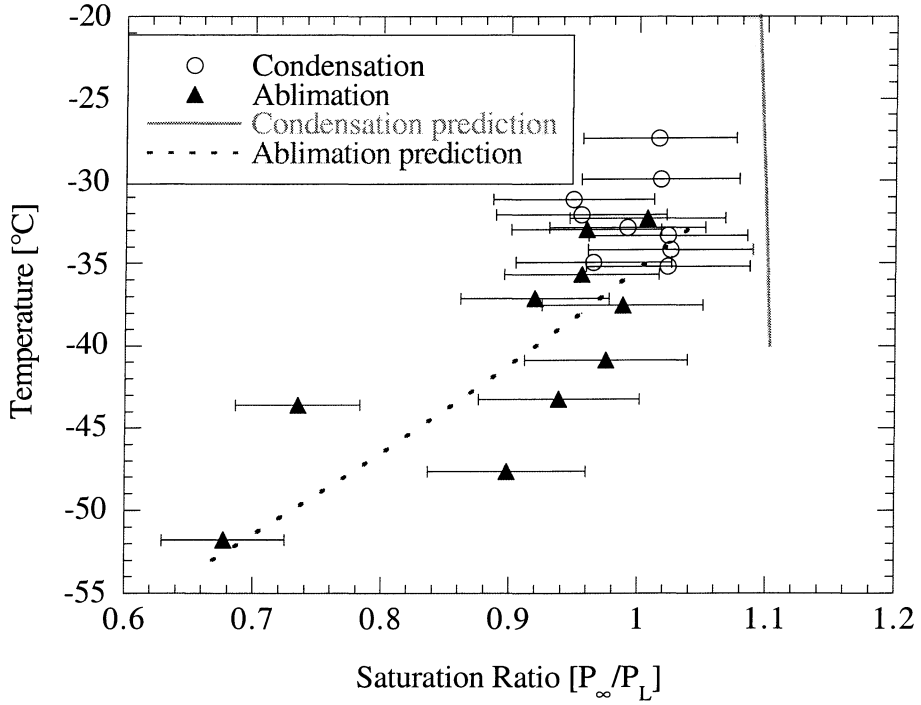

Figure 3.9 Prediction of ablimation and condensation based on classical nucleation theory and transition temperature

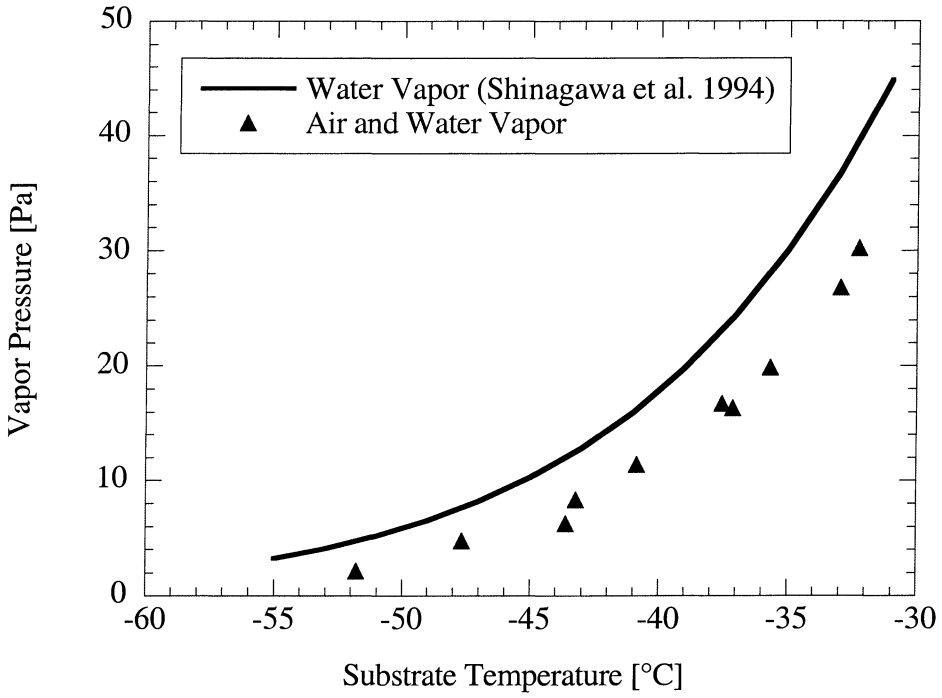

Figure 3.10 Measured temperature versus vapor pressure for the inception of ablimation by Shinagawa *et al.* (1994). The experiments performed by Shinagawa *et al.* (1994) were performed in pure water vapor atmosphere

4 Condensation Period

4.1 Introduction

In most refrigeration applications, the evaporator is operated at temperatures where only condensation frosting is possible (ASHRAE 1998). Even in refrigeration systems operating at very low temperatures, the evaporator will pass through conditions favoring condensation frosting during normal compressor cycling. This transient period can also occur when the system begins operation either for the first time or after a defrost-cycle. Thus, it is expected that refrigeration systems will be subject to condensation frosting, and because the present topic is motivated by applications in refrigeration, the remainder of this study is focused on condensation frosting.

In this condensation study, all environmental parameters were held constant during the duration of an experiment. This procedure represents a change in experimental protocol from that used in the ablimation study, since the temperature of the substrate decreased during the course of an experiment in the ablimation study. The condensation distribution was examined just prior to freezing as that distribution acts as an initial condition for the subsequent deposition of water onto the frozen droplets and eventual mature frost behavior.

4.2 Duration of the Condensation Period

Condensation on substrates at temperatures below the freezing point has a definite beginning and ending. In refrigeration applications, the condensation period begins when the substrate temperature reaches the dew point. In these experiments, the condensation

period started when the dry nitrogen stream, which had been flowing over the substrate during the thermal transient period, was replaced with a flow of humid air as described in Chapter 2. The condensation period ended when the water on the substrate froze. As will be discussed in Chapter 5, the freezing on hydrophobic substrates occurs slowly, so the definition of the end of the condensation period for these substrate was marked by the first appearance of ice in the field of view. The transition from liquid to solid was easily visualized since the opacity of the viewed sample changed, due to scattering from the growing crystal boundaries. Therefore, the accuracy in determining the beginning and ending of the condensation period was ±5 s.

The duration of the condensation period is plotted in Fig. 4.1 versus the mass transfer driving potential for three different temperature ranges, -12 to –10°C, -18 to –16°C and –25 to –23°C. The duration of the condensation period decreased with higher mass transfer driving potential and lower substrate temperatures. Additionally, the condensation period generally decreased as the substrate advancing/receding contact angle decreased. The scatter in the data of Fig 4.1 (a) make it difficult to firmly identify the trends. The scatter was primarily caused by the stochastic nature of the nucleation process. However, at the lower temperatures plotted in Fig 4.1 (b) and (c) there is much less scatter and the trends become more apparent.

From classical nucleation theory the functional form of the heterogeneous ice nucleation rate, J, is given by

$$J(T) = A \exp\left(\frac{B}{T}\right) \tag{4.1}$$

where A and B are constants that depend on the nucleation site characteristics (Hobbs 1974). The probability, P, that freezing will occur in a given time interval is

$$P(V,t) = 1 - \exp\left(-\int_0^t VJ(T)dt \right) \tag{4.2}$$

where V is the volume of liquid (Hobbs 1974).

Equations 4.1 and 4.2 indicate that the freezing probability increases significantly as the temperature of the substrate decreases. Therefore, lower substrate temperatures result in shorter condensation periods. The probability of freezing also increases with an increase in the amount of water on the substrate, since the number of possible heterogeneous nucleation sites increases with the increase of water volume. The substrate contact angle influences the condensation period in two possible ways: (i) Droplets on a hydrophilic substrate exhibit a large contact area with the substrate exposing the droplet to a greater number of heterogeneous nucleation sites at the substrate, altering the magnitude of the parameter A in Eq. (4.1); (ii) The activation barrier for nucleation is lower on a hydrophilic substrate resulting in a modification of the parameters A and B in Eq. (4.1). In Fig. 4.2 the length of the condensation period is plotted versus the substrate temperature multiplied by the difference in absolute humidity between the substrate surface and the free stream (the absolute humidity difference is approximately proportional to the amount of water on the substrate at a given time). The mass of condensate on the substrate was not measured but inferred through the driving potential. Therefore the effect of mass on the substrate and the effect of the deposition rate could not be separated. The absolute humidity driving potential in these experiments varied from 0.00054 to 0.010. The data are plotted this way because it provides a better

collapse of the data than the functionality given by Eqs. (4.1) and (4.2). Plotting the data in this fashion gave an upper envelope, inside which, the probability of finding the condensate frozen was unity. Also plotted in this figure is the probability curve when 50% of the experiments had completed the condensation period. It is apparent that the potential error in predicting the duration of the condensation period becomes larger at higher substrate temperatures and smaller mass transfer driving potentials.

4.3 Prediction of Condensate Distribution at the End of the Condensation Period

The distribution of condensate at the end of the condensation period on a hydrophobic substrate differs significantly from that on a hydrophilic substrate. For high contact angles, the liquid deposited on the substrate forms spherical caps. As the contact angle decreases, the approximation of the condensate as a spherical cap becomes less accurate. At low contact angles the condensate forms pools on the substrate and the perimeter of the pool can not be reasonably compared to that of a circle. Thus, the number and distribution of drops on a substrate with a low contact angle is less important than the coverage of the substrate. Separate predictions will be developed for the condensate distribution on substrates, where the droplets can be approximated as spherical drops and substrates where the deposited water forms pools.

On a substrate where the droplets can be accurately described as spherical caps, there are several parameters that must be known to predict the quantity of condensate on the substrate at the end of the condensation period. Assume for now that the distribution of the condensate can be adequately described by a single parameter, the volumetrically averaged droplet diameter, D_V. Where D_V is defined by

$$D_V^3 = \sum_{i=1}^{N} \frac{D_i^3}{N} \tag{4.3}$$

Here N is the total number of droplets in the field of view and D is the diameter of each droplet modeled as spherical cap. At the end of the condensation period, the volumetrically averaged droplet diameter is a function of

$$D_V = D_V\left(h_m, \rho_{v\infty}, \rho_{vw}, C_p, \theta\right) \tag{4.4}$$

As seen in Section 4.1, the duration of the condensation period is difficult to predict because of the stochastic nature of nucleation. This difficulty notwithstanding, at the end of the condensation period the water mass on the a substrate which has a contact angle greater than 90° is given by

$$m'' = h_m\left(\rho_{v\infty} - \rho_{vw}\right)C_p = \frac{1}{3}\rho_L N''\pi\left(\frac{D_V}{2}\right)^3\left(1+\sin(\theta-90°)\right)^2\left(2-\sin(\theta-90°)\right) \tag{4.5}$$

while for contact angles less than 90° the mass deposited is given by

$$m'' = h_m\left(\rho_{v\infty} - \rho_{vw}\right)C_p = \frac{1}{3}\rho_L N''\pi\left(\frac{D_V}{2}\right)^3\left(1-\sin(90°-\theta)\right)^2\left(2+\sin(90°-\theta)\right) \tag{4.6}$$

where N" is the number of droplets per unit area. Because of coalesce, the number of droplets on a particular substrate is dependent on the size of the droplets. Steyer *et al.* (1991) found that in the transient period of droplet growth, the number of droplets was dependent on the diameter as

$$N \propto \overline{D}^{-1.35} \tag{4.7}$$

where $\overline{D}$ is an ensemble average. Shown in Fig 4.3 is the relation between the droplets per unit area and volumetrically averaged droplet diameter. Note that in these

experiments, the number of droplets per unit area is governed by the quantity of liquid on the substrate. The number of droplets per mm^2 on the PTFE substrate can be approximated by

$$N'' = 1.1036x10^{6} * D_V^{-1.35} \tag{4.8}$$

where the form of the equation is chosen to match the findings of Steyer *et al.* (1991). The correlation coefficient for the above fit was 0.957. The number of drops on the kapton substrate is approximated by

$$N'' = 1.2584x10^{5} * \left(\frac{D_V}{\cos(90° - \theta)} \right)^{-1.35} \tag{4.9}$$

and the correlation coefficient for the fit was 0.958. The diameter of the spherical cap is directly measured for contact angles greater than 90°; however, for contact angles lower than 90° the diameter of the spherical cap must be calculated using the contact angle. The contact angle is left in the correlation given by Eq. (4.9) so that additional error by assuming a contact angle is not introduced.

Another significant parameter that affects the growth of frost is the coverage of the substrate. The fraction of the substrate covered by liquid, ζ, for contact angles larger than 90° is given by

$$\zeta = N''\pi \left(\frac{D_A}{2} \right)^2 \cos^2(\theta - 90°) \tag{4.10}$$

and for contact angles less than 90° the substrate coverage is given by

$$\zeta = N''\pi \left(\frac{D_A}{2} \right)^2 \cos^2(90° - \theta) \tag{4.11}$$

where D_A is the surface area averaged diameter given by

$$D_A^2 = \sum_{i=1}^{N} \frac{D_i^2}{N} \tag{4.12}$$

Again, because of coalescence, the surface area averaged droplet diameter can be related to the volumetrically averaged droplet diameter. In Fig. 4.4, D_A is plotted versus D_V and a linear relation is observed on the PTFE substrate

$$D_A = 3.4087 + .82446 D_V \tag{4.13}$$

and for the kapton substrate

$$\frac{D_A}{\cos(90° - \theta)} = 1.9885 + \frac{.8612 D_V}{\cos(90° - \theta)} \tag{4.14}$$

and the correlation coefficients for the curve fits are 0.998 and 0.997, respectively. With these correlations, the distribution of condensate can be described simply by the volumetrically averaged droplet diameter. Of course the amount of water on the substrate must be determined through the environmental conditions, mass transfer coefficient, and the duration of the condensation period.

When there are large pools of condensate on the substrate, as found on substrates with low contact angles, the substrate coverage becomes important to describe the initial condition for frost growth. The substrate coverage at the end of the condensation period is a function of

$$\zeta = \zeta\left(h_m, \rho_{v\infty}, \rho_{vw}, C_p, \theta\right) \tag{4.15}$$

The fraction of the substrate covered increases with decreasing contact angle and increasing water mass deposited. In this study, only one heat transfer coefficient and only one substrate that formed pools of water was examined in detail, a glass cover-slip. There was a large variation in the measured fraction of the substrate covered by liquid. This variation was partly due to the narrow field of view and partly due to the variability

of the substrate properties which caused the contact line to snag. The coverage for the glass substrate was measured to always be above 67% at the end of the condensation period. In Fig 4.5, the substrate coverage for the glass cover-slip is shown along with the coverage observed on the PTFE and kapton substrates for comparison. The substrate coverage for the glass cover slip can be crudely (the correlation coefficient is 0.692) approximated by the correlation

$$\zeta = -33.54 * (\Delta\omega Cp)^{-0.951}\left(1 - \exp\left(0.02597 * (\Delta\omega Cp)\right)\right) \qquad (4.16)$$

Although the predictions provide a way to calculate the substrate coverage (hydrophilic and hydrophobic) and number of drops (hydrophobic), the predictions depend on the length of the condensation period which is difficult to predict.

4.4 Distribution Observations at the End of the Condensation Period

Shown in Fig. 4.5 is the substrate coverage plotted versus the mass transfer driving potential times the length of the condensation period. For equal mass transferred (assuming the mass transfer coefficient does not differ significantly between substrates) the glass substrate which had an advancing contact angle below 10°, covered a significantly larger portion of the substrate than either kapton or PTFE. The percentage of the substrate covered by water did not change with environmental parameters as radically as it did with substrate contact angle.

The effective density of the liquid on the PTFE substrate at the end of the condensation period was between 15 and 35% that of water, ±5%. The effective density of the liquid on the hydrophilic glass substrate was significantly higher than that on the PTFE. In general, the error in measuring the mass deposited and density on the

hydrophilic substrates was large due to the sensitivity of this calculation on the contact angle which was greater than ±15% for a contact angle of 67°. Therefore, the extreme case of a perfect substrate where a layer of water is deposited will be compared to the water deposited on the hydrophobic, PTFE substrate. For the water deposited on a prefect hydrophilic substrate, the density of the layer is that of water. Thus the initial density of the condensate on the ideally hydrophilic substrate is approximately 3 to 6 times greater than that measured on the PTFE substrate.

Shown in Fig. 4.6 is the volumetrically averaged droplet diameter versus the substrate temperature for PTFE and kapton. The size of the drops at the end of the condensation period was generally smaller at lower substrate temperatures. Plotted in Fig. 4.7 is the number of droplets per mm^2 versus the substrate temperature on PTFE. As expected, for the same mass transfer driving potential, as the droplet diameter decreased, the number of droplets increased.

To elucidate the contact angle and substrate temperature effects, three-dimensional images of the water deposited on the substrate were constructed. The effect of a warmer substrate on the distribution of water at the end of the condensation period can be see by comparing Fig. 4.8 and 4.9. In Fig. 4.9 the substrate temperature is 5.6° warmer while the other environmental parameter were similar to those of Fig 4.8. Note that the condensation period for the conditions of the experiment shown in Fig 4.9 is 1.76 times longer than for the conditions in Fig. 4.8. The effect of the substrate contact angle can be seen by comparing Fig. 4.9 and 4.10. The environmental parameters during these two experiments were similar, but in Fig 4.10 the droplets are much flatter and pancake shaped.

In order to construct these images, the location and diameter of the droplets were recorded. The droplets were assumed to be spherical caps with a contact angle equivalent to the advancing contact angle measured for an approximately 3 mm diameter droplet see Table 2.7. A typical SCM image is shown in Fig. 4.11. The scale of the SCM image is displayed in the lower-right corner and the temperature of the test was recorded in the upper-left corner. The diameter of the droplets was found by recording the area of each droplet and then calculating the diameter assuming a circular cross section, see Fig. 4.12. With the position and diameter of all the droplets in an image, a three dimensional view of the condensate was constructed by assigning a value of one (1) to all pixels located within the droplets and zero (0) to all pixels located outside of the droplets. The step in the z direction was 3 pixels. The resulting image is shown in Fig. 4.8, (cf. Fig.4.11.)

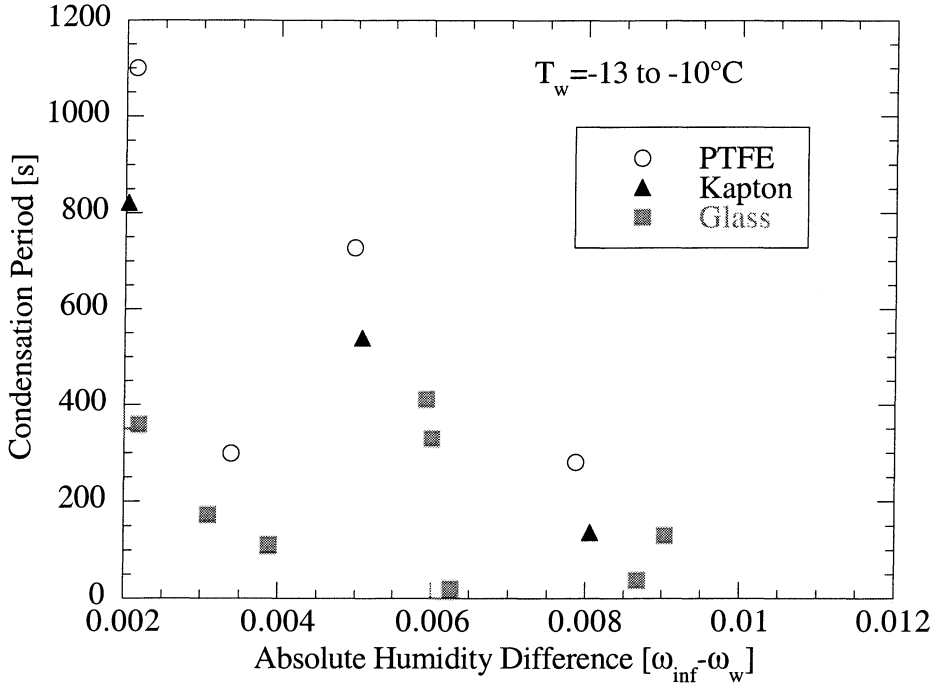

a

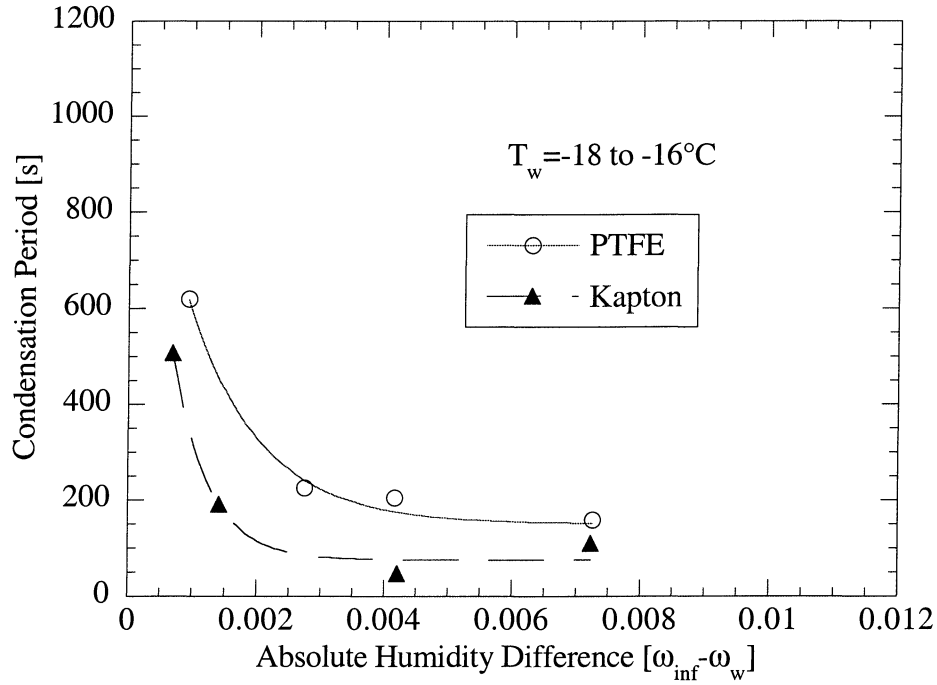

b

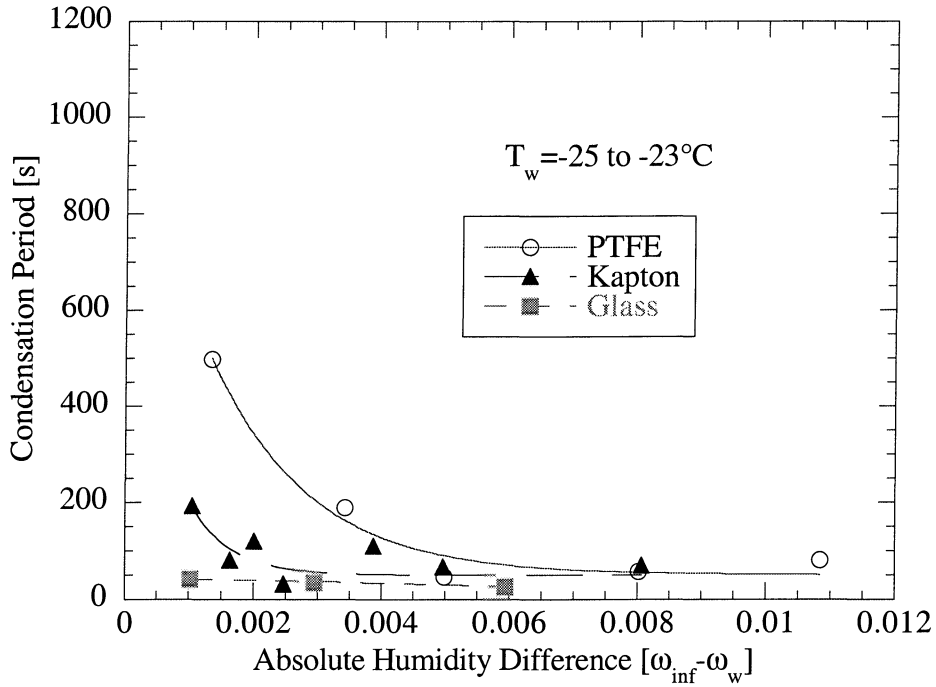

c

Figure 4.1 Condensation period versus mass transfer driving potential: (a) T_w= -12 to –10°C, (b) T_w= -18 to –16°C, and (c) T_w= -25 to –23°C

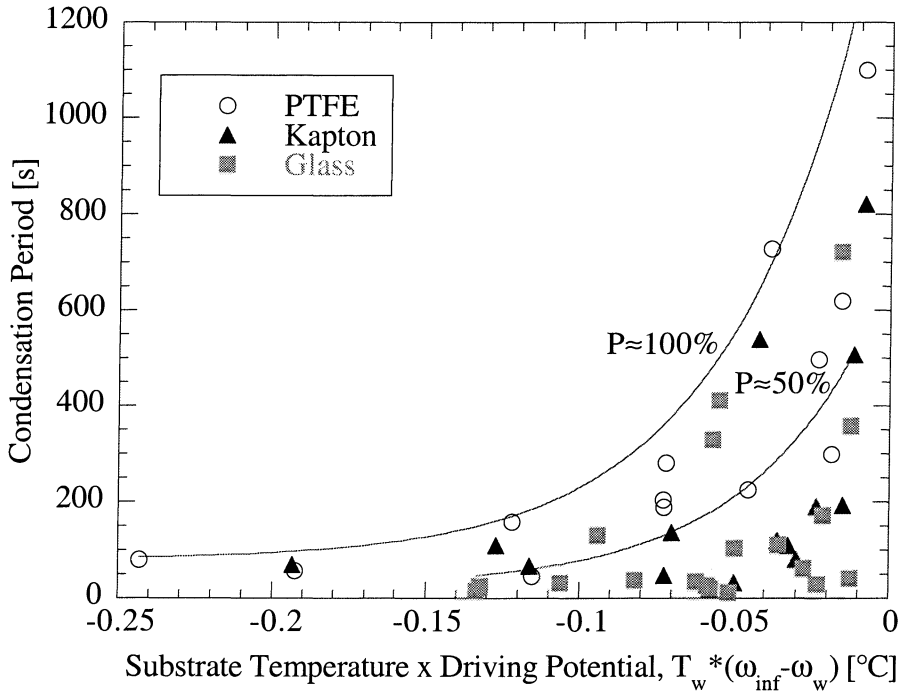

Figure 4.2 Condensation period versus substrate temperature times mass transfer driving potential

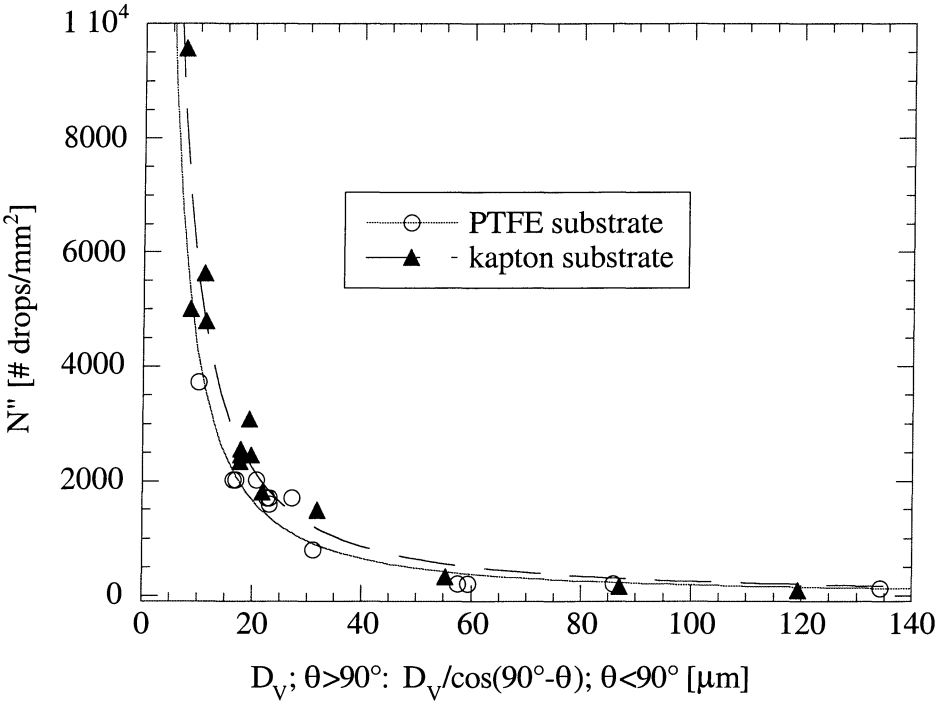

Figure 4.3 Number of drops per unit area versus the volumetrically averaged droplet diameter

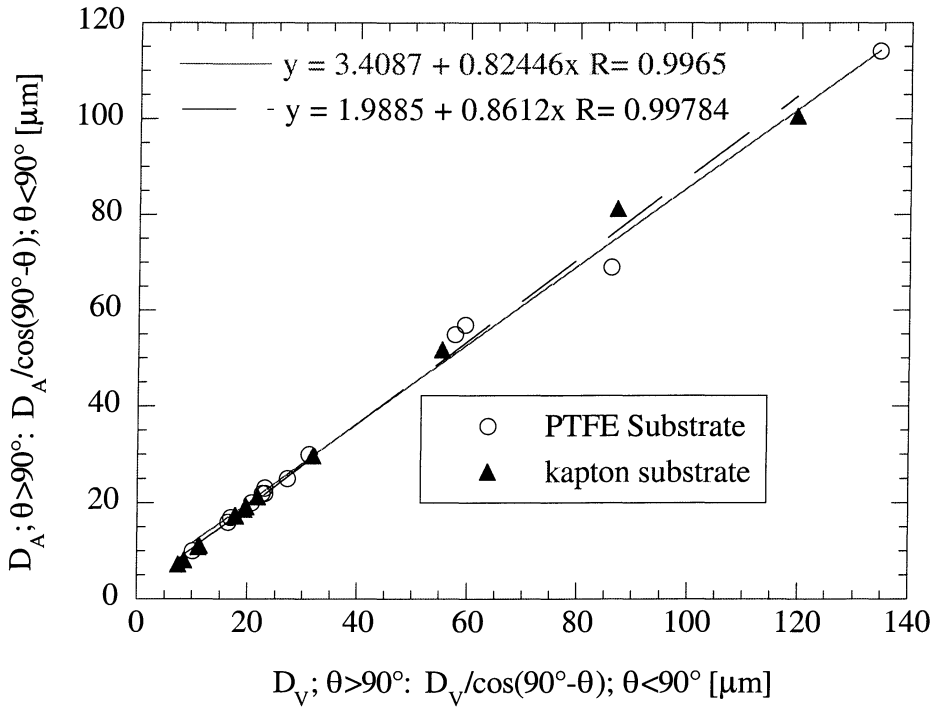

Figure 4.4 Surface area averaged droplet diameter versus volumetrically averaged droplet diameter

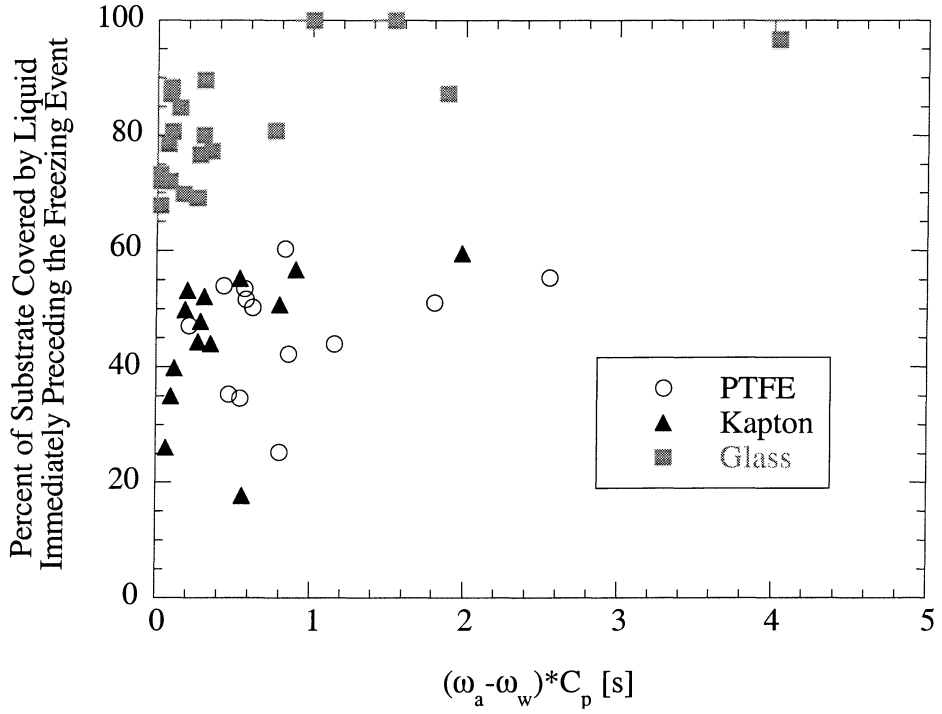

Figure 4.5 Percentage of substrate covered versus potential mass transferred

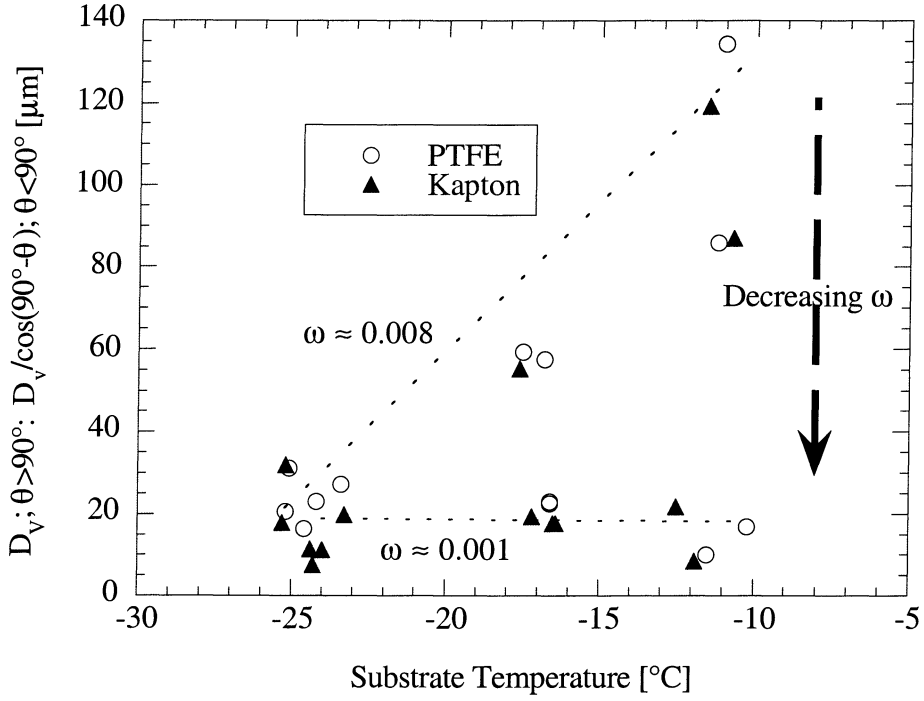

Figure 4.6 Volumetrically averaged droplet diameter versus substrate temperature

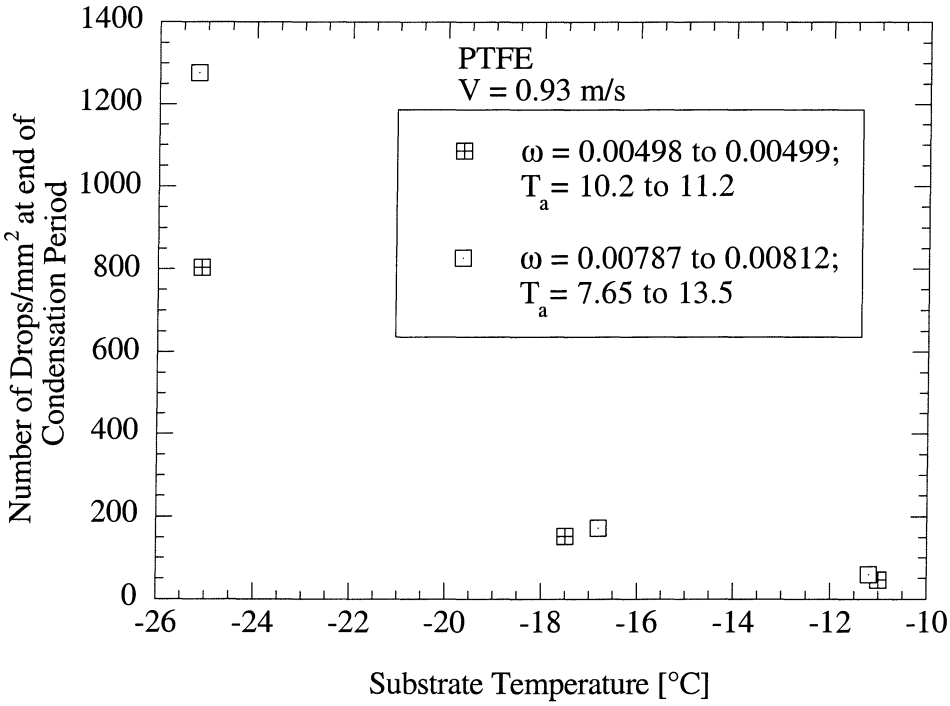

Figure 4.7 Droplets per mm^2 versus substrate temperature

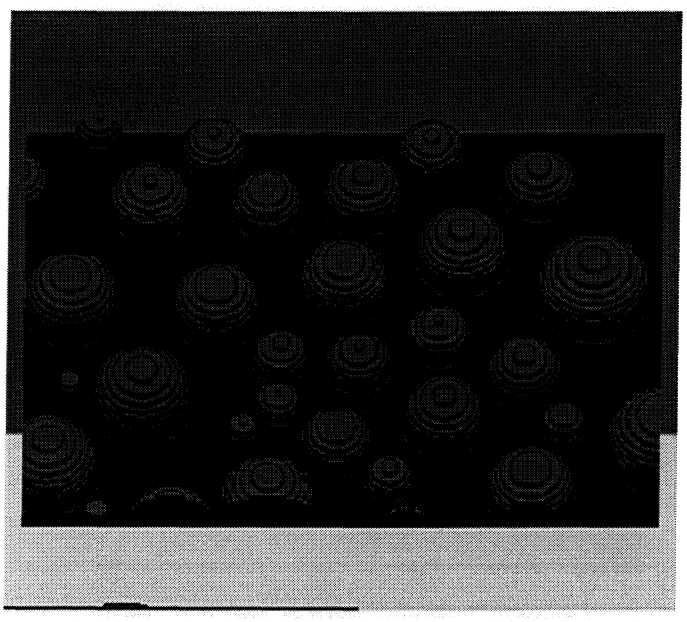

Figure 4.8 Reconstruction of condensate on PTFE substrate: C_p = 159 s, ω = 0.0081, T_s = -16.8°C, and T_a = 11.4°C

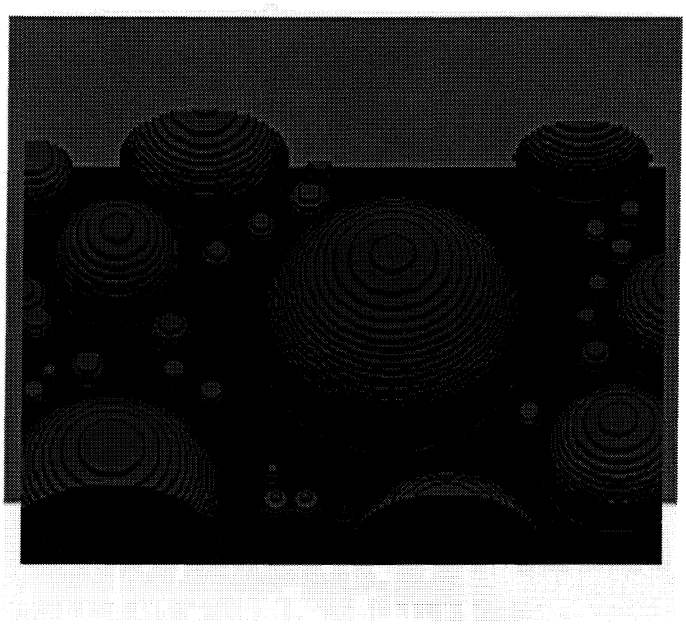

Figure 4.9 Reconstruction of condensate on PTFE substrate: C_p = 281 s, ω = 0.0079, T_s = -11.2°C, and T_a = 13.5°C

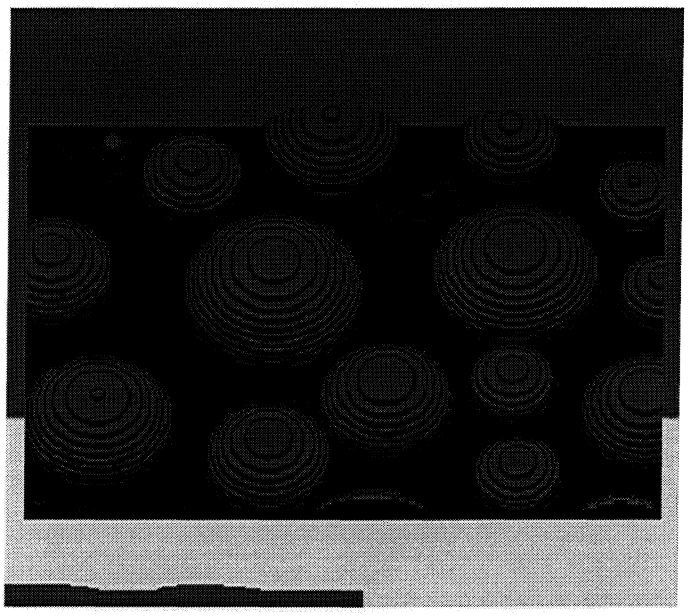

Figure 4.10 Reconstruction of condensate on kapton substrate: C_p = 137 s, ω = 0.0081, T_s = -10.7°C, and T_a = 12.4°C

Figure 4.11 SCM image of condensate on PTFE substrate immediately preceding freezing

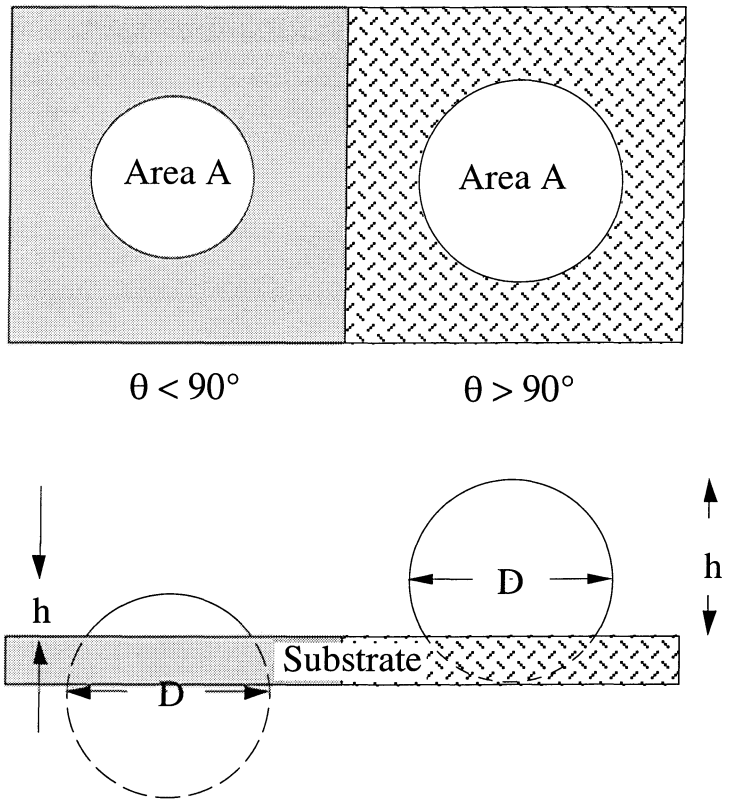

Figure 4.12 Schematic of diameter and height calculated to reconstruct 3-D image

5 Freezing Characteristics

5.1 Introduction

As described in Chapter 4, the distribution of water on the substrate varies from tall independent droplets on a hydrophobic substrate to a thin layer on a hydrophilic substrate. The freezing event separates the condensation period from the early growth period. In this chapter, the freezing front propagation and resulting frost structure are examined with respect to substrate contact angle. A transient dilation phenomenon is reported for the first time, and an explanation proposed, relating the observations to the transient appearance of fine satellite droplets around the main condensate mass during the freezing process on a hydrophobic substrate.

5.2 Freezing on a Hydrophilic Substrate

Nucleation in an isolated droplet occurs at the perimeter of a droplet on the surface of the substrate (Hoke *et al.* 2000). The freezing front propagates from this initial nucleation site (there can be multiple nucleation sites within a droplet or layer) essentially, as a planar front parallel to the substrate; however, because of the release of latent heat, the entire thickness of the layer does not freeze. Two distinct freezing fronts are evident propagating through a thin layer of water on an oxidized silicon wafer in Fig. 5.1 (a). As discussed in Chapter 2, the contact angle for water on a clean silicon wafer was less than 10°. This layer of water on a silicon wafer was viewed from an angle between 30 and 60° off normal to the substrate, but the wafer was horizontal. The edge of the silicon wafer runs from the lower-left corner toward the upper-right corner of the

image. The larger arrow indicates the direction of propagation of the freezing fronts while the two smaller arrows show the two distinct freezing fronts. The position of the fronts are shown 0.13 s later in Fig 5.1 (b). The freezing front propagated across the width of the field of view (≈1.1 mm) in 1 s. When there was a single layer of water on the substrate, the freezing front propagated across the substrate as fast as the latent heat of fusion was removed either by conduction into the substrate or convection into the boundary layer. An image of the resulting frozen layer on the silicon wafer is shown in Fig. 5.2. In this image, the silicon wafer was parallel to the focal plane. Large crystal structures are clearly evident.

Glass substrates that were ultrasonically cleaned, also had a contact angle un-measurable, and less than 10°; however, there were regions where the contact line was pinned because of surface imperfections. An image of ice on a glass slide is shown in Fig. 5.3 just after the condensate froze. Prior to freezing, the substrate was covered by large flat droplets. Typically, after a droplet freezes, the adjacent droplets on the substrate will freeze because a crystal from the frozen droplet grows along the water vapor pressure gradient toward the adjacent unfrozen droplets. Once the crystals contact the unfrozen droplets, freezing begins immediately. This progressive freezing process is better illustrated by examining droplets on a hydrophobic substrate (and will be examined in Section 5.3) since there is a greater distance between these droplets. In Fig. 5.3, the complex multi-crystalline structure of the ice layer on theses substrates is depicted.

5.3 Freezing on a Hydrophobic Substrate

Unlike freezing on a hydrophilic substrate, the freezing event on a hydrophobic substrate can have a duration of many seconds, even over the small area in the field of view for these experiments. The five images shown in Fig. 5.4 were recorded over roughly a 16 second period; they show freezing progressing across the substrate. In this figure, the substrate was a silicon wafer coated with octadecyltrichlorosilane (OTS). OTS forms a self-assembled monolayer on silicon, see Jeon *et al.* (1997) for details. The advancing contact angle was 99°, and the receding contact angle was 74°. In Fig. 5.4 (a) droplet 'A' had already frozen. This observation is based on the coarseness of the perimeter, opacity of the "droplet", and change in amount of light reflected from the top of the droplet. The droplet adjacent to 'A', droplet 'B', froze next and then 'C', froze. The progression of the freezing process branched out and droplet 'G' and 'E' froze, as shown in Fig. 5.4 (b) through (d). In Fig. 5.4 (d) two arrows point toward ice crystals which grew from a frozen droplet toward an unfrozen one. In Fig. 5.4 (e) one of the ice crystals had reached the unfrozen droplet, 'G' and 'H', which caused these droplets to freeze. This growth of ice crystals from a frozen droplet to an unfrozen droplet occurs because of the vapor pressure difference between ice and water at the same temperature. At –10°C the difference in vapor pressure between ice and water is approximately 26 Pa (Kraus and Greer 1984), and the water vapor pressure in equilibrium with ice at –10°C is 260 Pa (Lide 1992). Comparing the area around the white circle in Fig. 5.4 (e) with the corresponding area in (c) many of the satellite droplets, the small droplets surrounding the larger droplets, have disappeared. This disappearance of the small droplets was also caused by the vapor pressure difference between the water vapor pressure above the large

frozen droplets and the water vapor pressure above the smaller liquid droplets. Many of these droplets evaporate completely before freezing can occur.

A broader perspective of the freezing process on a hydrophobic substrate can be gained by examining Fig. 5.5. In Fig. 5.5 (a) arrows indicated the recent propagation of the freezing front across the substrate. The droplets in the lower-right corner were frozen while those in the upper-left corner were still liquid as evident by the reflection from the center of the droplets. The droplet circled was the next droplet to freeze. In Fig. 5.5 (b) the droplet is freezing, and careful comparison between Fig. 5.5 (a) and (b) reveals a substantial increase in the opaque area caused by the droplet. In Fig. 5.5 (c) the area has decreased to approximately that in (a). This fleeting dilation of the freezing droplet was better captured in Fig. 5.6. In Fig. 5.6 (a), all of the droplets were liquid. In Fig. 5.6 (b), the droplet in the upper-right corner was freezing and a dilated perimeter of the droplet was evident by comparing the distance between the freezing droplet and its nearest neighbor in Fig 5.6 (a) and (b). The original perimeter of the unfrozen droplet has also been superimposed on the image. In Fig. 5.6 (c) the dilation had receded and the droplet was frozen. To this author's knowledge, this phenomenon has not been previously reported. A plausible explanation for the cause of this fleeting dilation will be given in Section 5.4.

Another phenomenon that occurred during freezing of a droplet on a hydrophobic substrate was the formation of a protrusion on the top of the droplet. In Fig. 5.7 the development of the protrusion on a droplet during freezing is shown. The droplet was imaged on a vertical surface, so the gravity vector pointed into the picture. In Fig. 5.7 (a) the droplets were liquid. In Fig. 5.7 (b) a protrusion formed at the top of the droplet

during freezing is shown, and in Fig 5.7 (c) the protrusion is shown to have grown into a dendroid.

The freezing morphology and characteristics have significant implications for frost properties and growth patterns which will be discussed in Chapter 6 and 7. In Section 5.4, the underlying mechanism for the formation of this protrusion is detailed.

5.4 Protrusion Formation Mechanism

In this section, mechanisms important to the structure and form of a freezing droplet on a hydrophobic substrate are examined. Through the use of a high-speed CCD camera, images of the freezing process within a droplet were acquired. For the images presented in this section, the substrate temperature was held constant at –13.5°C, and the airflow rate over the substrate was 0.93 m/s with an absolute humidity of 0.0069 kg/kg. Images of the freezing front were acquired at 4000 Hz. Time zero was defined as the last frame for which the entire droplet was still liquid. In Fig. 5.8 the initiation of freezing and the propagation of the freezing front across the lower portion of the droplet closest to the substrate is shown. The diameter of the droplet in this image was 59 μm. In Fig. 5.8 (b) the droplet has been touched by an ice crystal in the lower-left-hand corner of the image, marked by an arrow, and distortion of the droplet was evident. The freezing front propagated across the droplet in Fig. 5.8 (c) and (d). The velocity of the freezing front was estimated to be 17 mm/s. This initial rapid freezing occurred because of the subcooling of the droplet and intimate thermal contact with the substrate. Assuming, no heat transfer to the droplet, 21% of the droplet will freeze before the temperature of the droplet increased to T_{tp} as given by Eq. (5.1).

$$\frac{m_\phi}{m} = \frac{c_p\left(T_{tp} - T_s\right)}{\lambda_{ls}} \tag{5.1}$$

The assumption of an adiabatic droplet during freezing leads to a conservative estimate of the percentage of the droplet which froze initially. The droplet was in intimate contact with the substrate and from the images, the freezing front propagated quickly across the droplet, freezing the liquid closest to the substrate because the latent heat of fusion could be conducted into the substrate. In Fig. 5.8 (d) the completion of the initial freezing event which occurred in approximately 5 ms is imaged. In Fig. 5.8 (e), the crystal structure is observed to grow and coarsen. At this point, there is a layer of ice along the substrate and liquid in the upper portion of the droplet

In Fig. 5.9, the completion of the freezing process is shown to proceed much slower, occurring in 200 ms. The average velocity of the freezing front across the droplet is approximately 0.6 mm/s, based on a length scale of half of the diameter of the droplet. This velocity is consistent with an order of magnitude analysis of the propagation of a freezing front in 1-D medium. The velocity of the freezing front is given by

$$v(t) = \frac{k_{ice}}{\rho_s \lambda_{sl}} \frac{\partial T_{ice}}{\partial x} - \frac{k_l}{\rho_l \lambda_{sl}} \frac{\partial T_l}{\partial x} \tag{5.2}$$

and inserting the magnitude of each of the parameters

$$v(t) \approx \frac{O(1)}{O\left(10^3\right)O\left(10^5\right)} \frac{O(10)}{O\left(10^{-4}\right)} - \frac{O(0.1)}{O\left(10^3\right)O\left(10^5\right)} \frac{O(10)}{O\left(10^{-4}\right)} = O\left(10^{-3}\right) \tag{5.3}$$

The velocity is found to be on the order of mm/s.

In Fig. 5.9 (a) and (b) the continuing coarsening of the crystals created during the initial freezing event is shown. In Fig. 5.9 (c), a new freezing front is evident around the perimeter of the droplet. This freezing front proceeded toward the top of the droplet as

evident in Fig. 5.9 (c) through (i). Because the latent heat of fusion could be removed through conduction through the drop *and* convection to the thermal boundary layer over the flat plate, the water on the outer shell of the droplet froze faster than the interior water. The difference in freezing time of the interior and exterior water resulted in the formation of a protrusion on the top of the droplet as the remaining, interior water expanded during freezing. (Horibe *et al.* (1993) found the location of the protrusion was a function of air stream velocity, indicating that convective heat transfer is significant.) The protrusion is evident as the dark circle approximately located in the center of the frozen droplet, see Fig. 5.9 (i). As demonstrated here, the formation of the protrusion at the top of the droplet is caused by the freezing front propagation and the difference in specific volume of water and ice. This protrusion rapidly grows into a dendroid during the early growth period.

For the contact angles found on kapton, the spacing between droplets and the thickness of the droplets decreased compared to those on the PTFE substrate. Shown in Fig 5.10 (a) and (b) are two different focal planes of frozen droplets on kapton, which has receding and advancing contact angles of 28° and 67°, respectively. A frost spire is shown to be growing out of the top of each of the larger droplets. The frost spire is growing on a protrusion created at the end of the freezing. This type of protrusion was not always observed on kapton and never observed on the more hydrophilic substrates.

5.5 Freezing Dilation Phenomenon

The observation of an intermittent dilation during freezing was unexpected; it was possible because of the high resolution microscopy. This phenomenon does not

significantly affect the frosting process, but is discussed here because it is an interesting display of physics. Figure 5.12 and 5.13 provide another view of the freezing event; however, the microscope was focused immediately above the substrate rather than on the droplet. In Fig. 5.12, a 77 μm droplet froze after being touched by an ice crystal. The substrate temperature was –10.1°C , and the air flow rate was 0.93 m/s. After being touched by the crystal the droplet moved so that the right contact line moved to the left by approximately 22 μm, compare Fig. 5.12 (a) and (g). Images were acquired at 2000 Hz.

In Fig. 5.13, a freezing front is evident on the surface of the droplet proceeding from the initiation site on the left to the right. In Fig. 5.13 (b), small droplets are first evident on the right side of the freezing droplet. The number of droplets increased in the successive images up through Fig. 5.13 (i), the completion of the freezing event. Figure 5.13 (j) was acquired 845.5 ms after (i) and it was evident that a large number of the droplets had evaporated between Fig. 5.13 (i) and (j), probably depositing onto the now frozen droplet. It is interesting to note that the majority of droplets were located on the side of the droplet toward which, the freezing front propagated. However, this was also the side where the droplet originally was located. In Fig. 5.14 the original droplet location superimposed on the frozen droplet image is shown. The majority of small droplets appeared within this perimeter, but there were a number of small droplets located in the upper and lower-left-hand corners, outside of this perimeter.

I postulate that the creation of the small droplets around the large droplet is driven by the a vapor pressure differences between the substrate and freezing droplet. As noted earlier, the initial freezing front propagates relatively quickly over the surface of the

supercooled droplet. For the supercooling experienced by this droplet, approximately 16% of the droplet will freeze, as predicted by Eq. (5.1), before the temperature of the remaining water in the droplet reaches the triple point. This sudden rise in droplet temperature increases the vapor pressure above the droplet. A sudden vapor pressure 'spike' has been recorded by Shinagawa *et al.* (1992) for droplets freezing on a substrate in a quiescent chamber. The saturation humidity ratio is 0.001591 and 0.003787 at –10.1°C and 0°C, respectively. However, the air temperature around the droplet was closer to the substrate temperature. Using boundary layer theory we can estimate the temperature of the air 100 μm from the substrate will be 1.5° C higher than that of the substrate. This leads to a condition of supersaturation around the droplet. The equilibrium humidity ratio at –8.6°C is 0.001817 and the ratio of supersaturation would be 2.1. This supersaturation may result in a cloud of suspended droplets around the freezing droplet causing the apparent dilation during freezing.

The freezing process took approximately 450 ms, whereby the humidity ratio above the droplet will be assumed to be that in equilibrium above water at 0°C. The mass flux of water toward the substrate can be approximated by

$$\dot{m}'' \approx D_{AB} \frac{(\omega_{0°C} - \omega_{-10°C})\rho_a}{\Delta x} \qquad (5.4)$$

The diffusion coefficient for water vapor in air at 0°C is 2.3×10^{-5} m^2/s, while at –10.1°C the diffusion coefficient is slightly less at 2.15×10^{-5} m^2/s. The characteristic length over which diffusion occurs is assumed to be half of the droplet diameter, 38.5 μm and the density of the air is taken to be 1.31 kg/m^3. The mass flux of water to the substrate is 1.66×10^{-3} kg/m^2-s. This flux over an area equal to half of the droplet area for 450 ms results in a mass transferred to the substrate of 1.74×10^{-12} kg, corresponding to a volume

of 1742 μm^3. Based on Fig. 5.13 (i), the number and diameter of the small droplets on the substrate was estimated to be 300 and 1.5 μm, a cumulative volume of 1019 μm^3. The lack of small droplets to the left of the image was attributed to the fact that there was a cold frozen droplet onto which the water vapor preferentially ablimated.

This phenomenon is robust since it was observed on several different hydrophobic substrates and was even observed on pendent droplets viewed through the substrate (the substrate was glass with a clear hydrophobic coating). This phenomenon was not observed on kapton or glass (hydrophilic), probably due to the intimate thermal contact that the droplets had with the hydrophilic substrates. Another view of this phenomenon is shown in Fig. 5.14 where a water droplet is shown during freezing on solid cylcohexane. The time between images is 1/30 s.

a

b

Figure 5.1 Freezing front propagation on an oxidized silicon wafer, viewed 30 to 60° from normal to the substrate

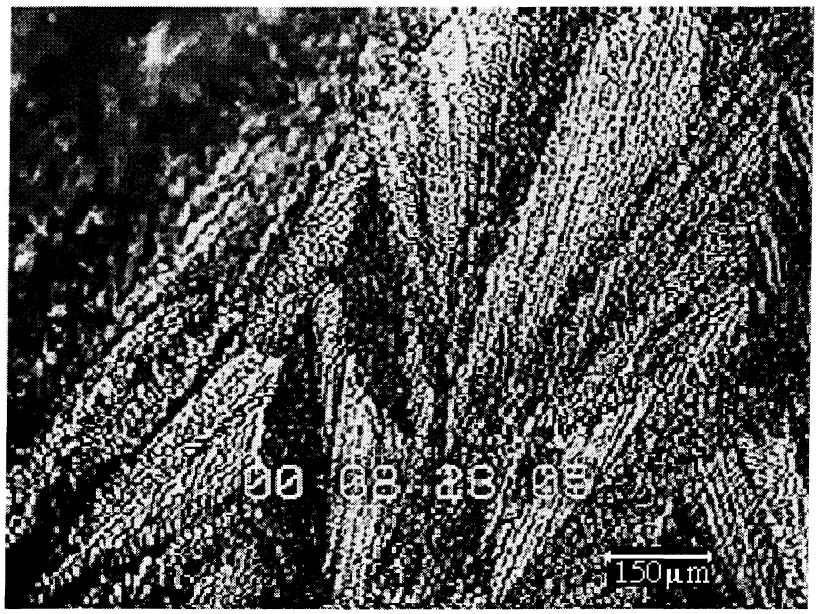

Figure 5.2 Freezing follows condensation on a clean silicon wafer

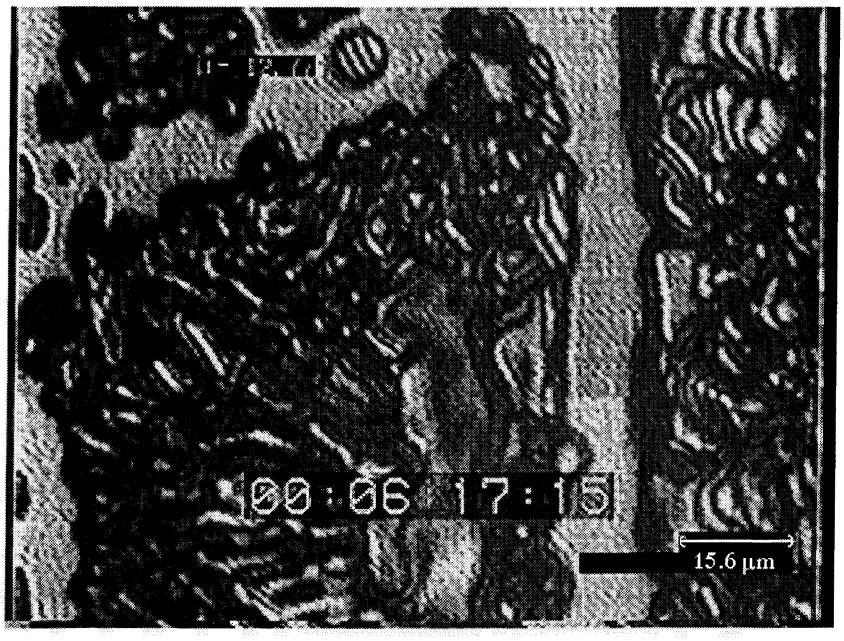

Figure 5.3 Freezing follows condensation on ultrasound cleaned glass

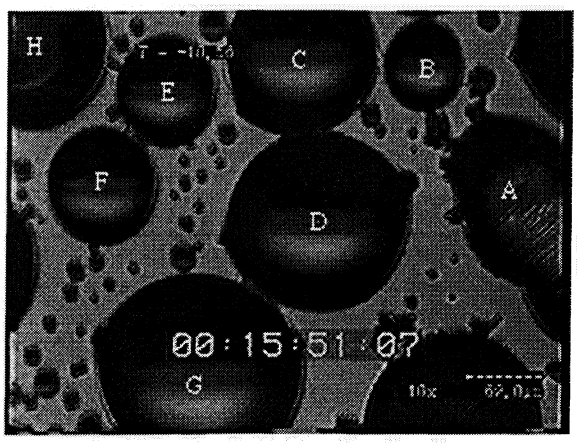

a

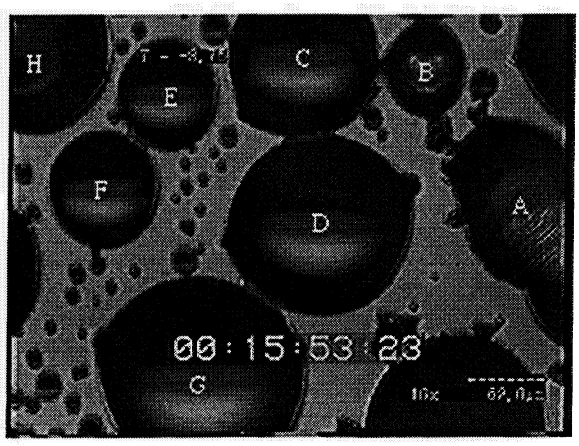

b

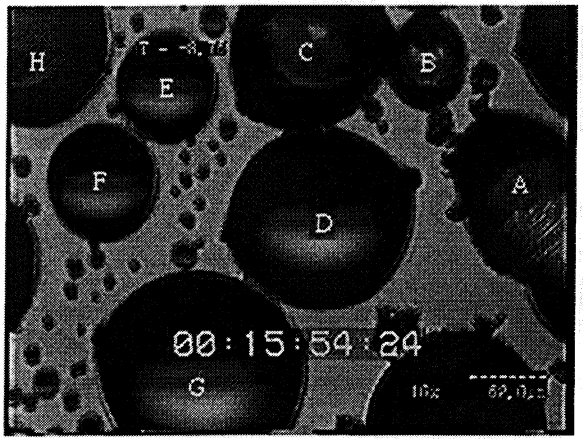

c

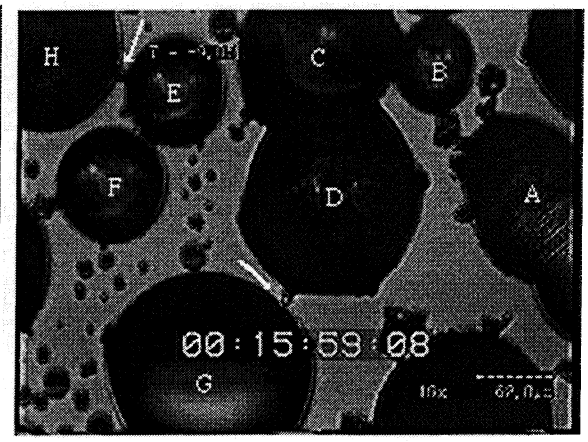

d

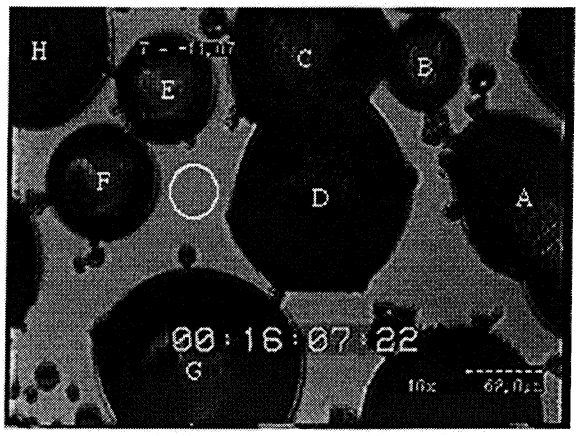

e

Figure 5.4 Water droplets freezing in-tandem on a hydrophobic substrate, fabricated by depositing OTS on a silicon wafer

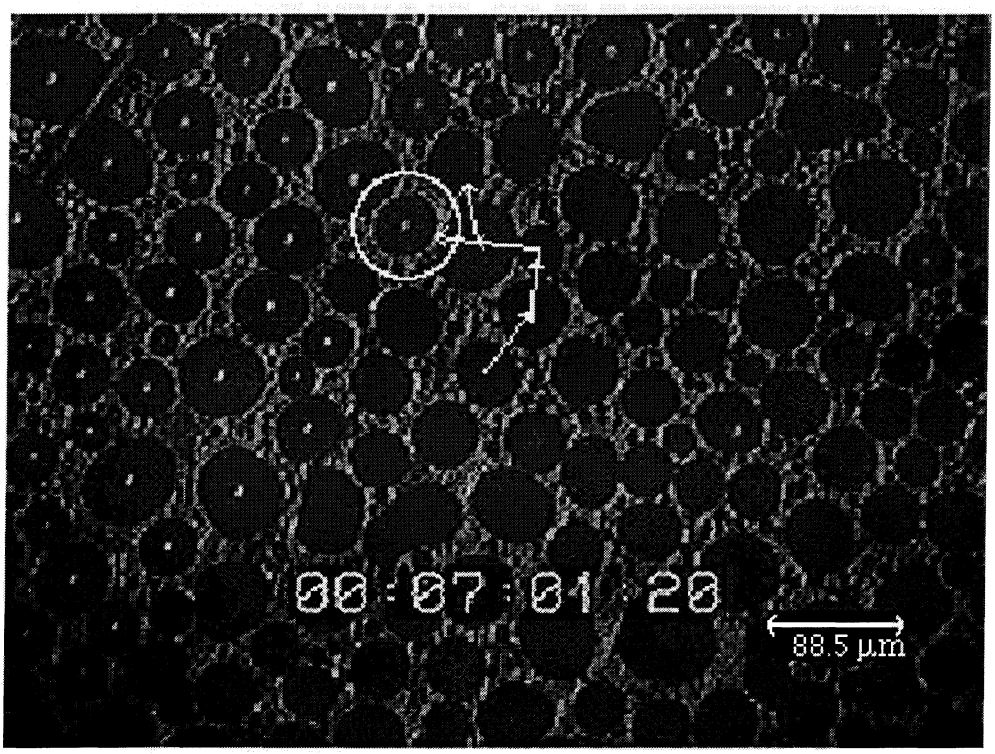

a

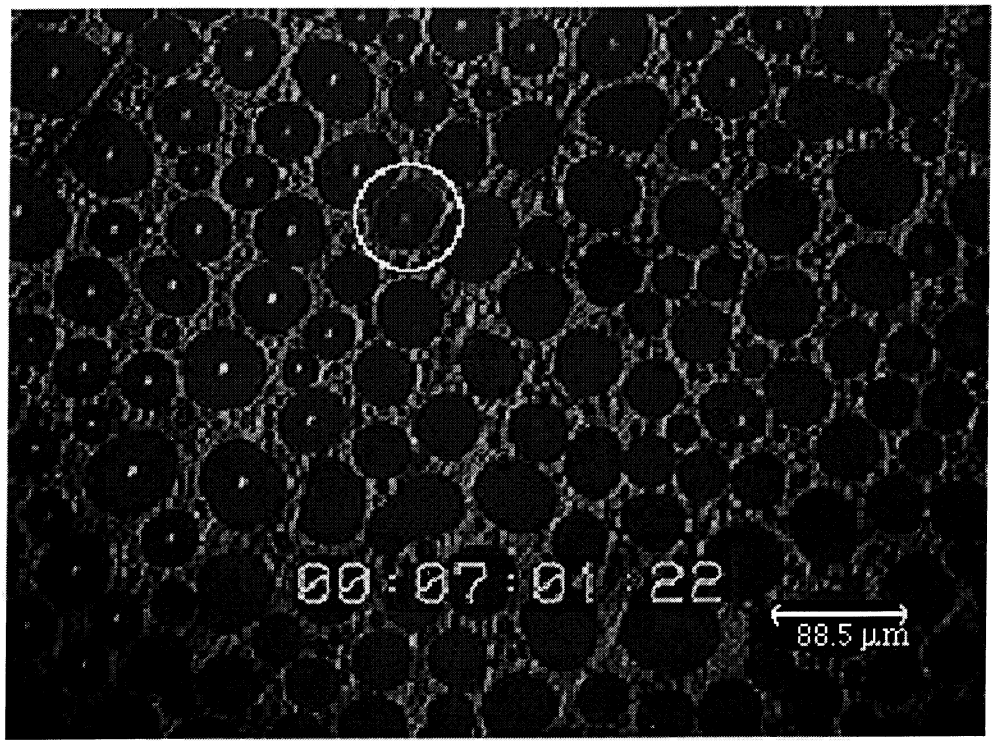

b

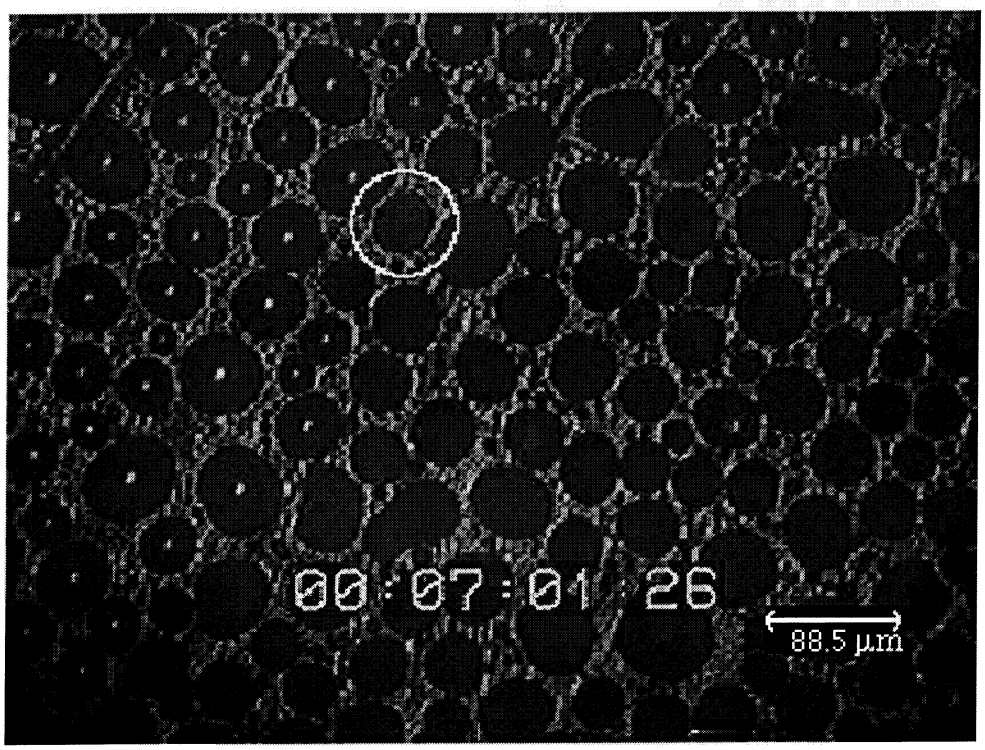

c

Figure 5.5 Freezing front propagation on hydrophobic PTFE substrate

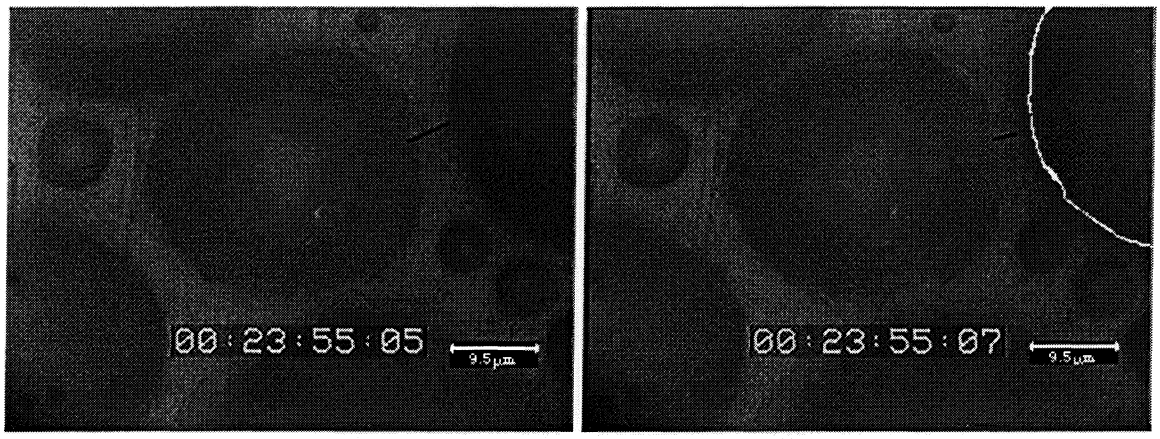

a b

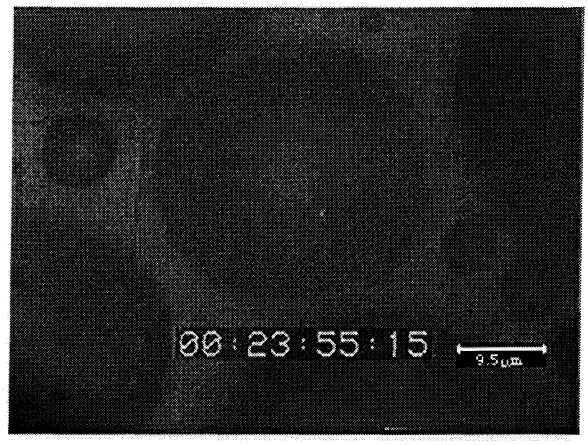

c

Figure 5.6 Droplet dilation on PTFE substrate 100X CCD Camera

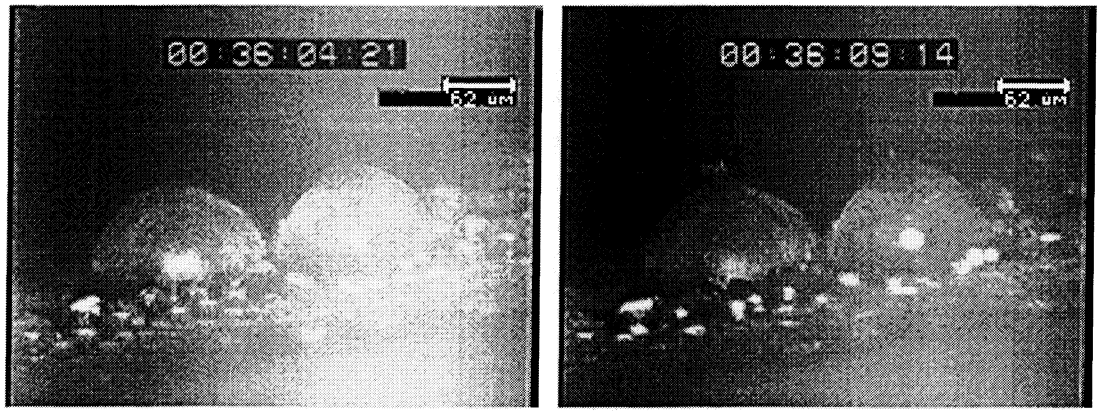

a b

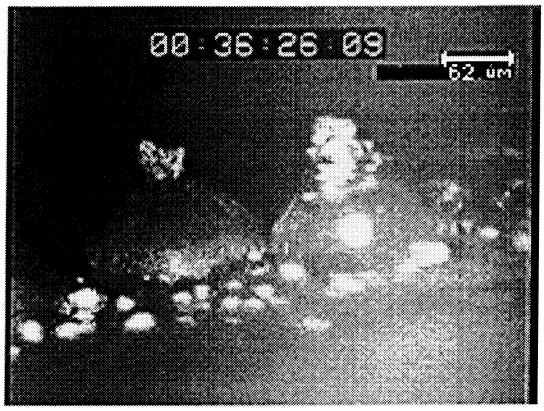

c

Figure 5.7 Side view of droplet freezing on PTFE substrate

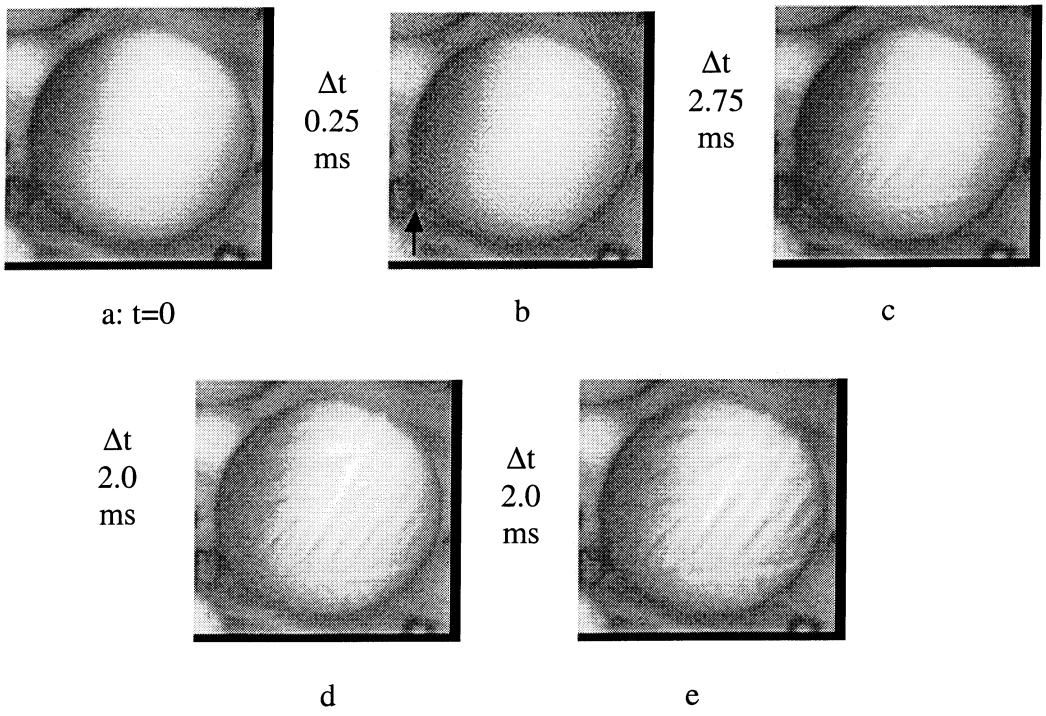

Figure 5.8 Initial freezing front propagation, condensate on PTFE substrate

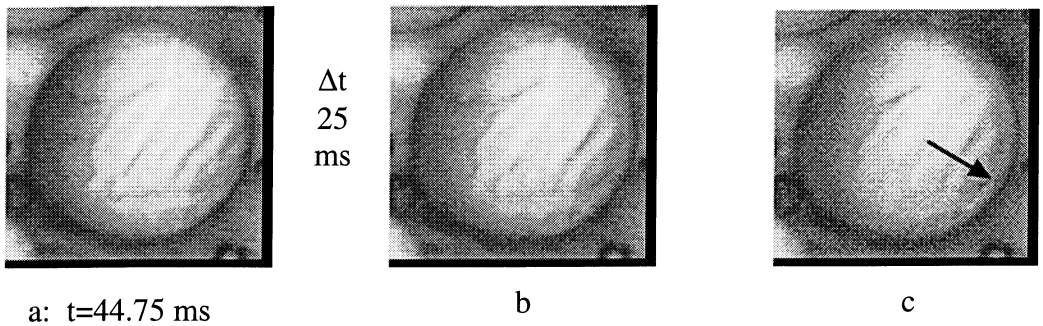

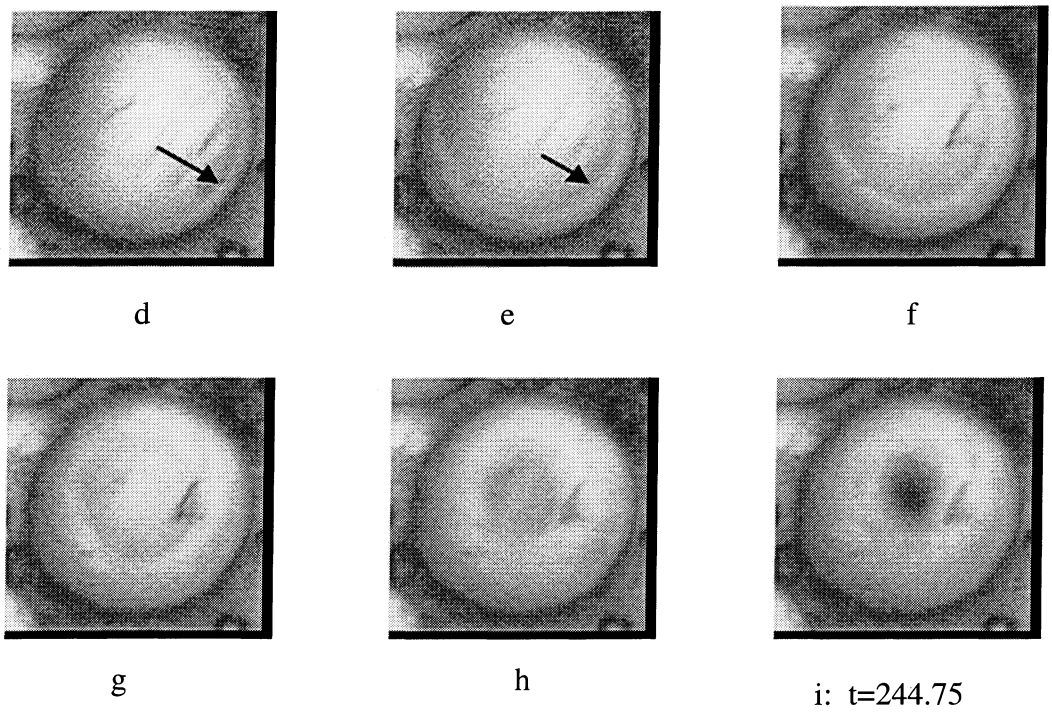

Figure 5.9 Freezing of upper portion of droplet and protrusion formation

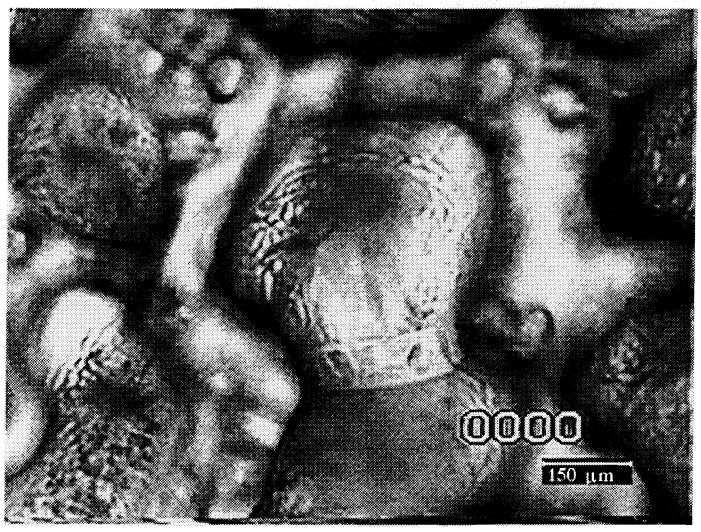

a

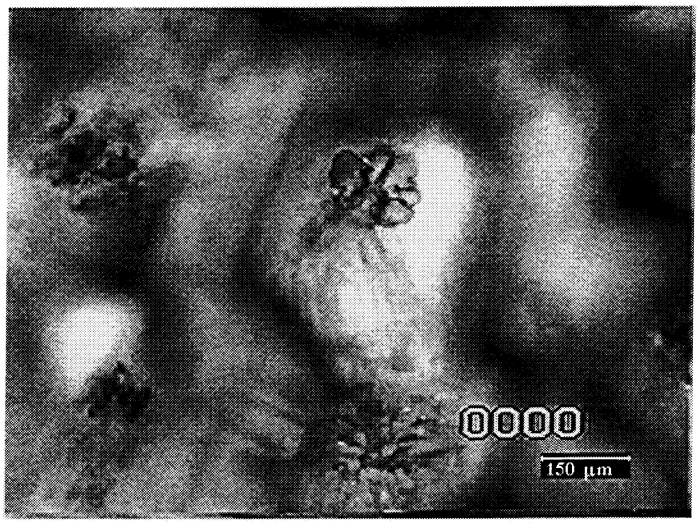

b

Figure 5.10 Droplets frozen on kapton substrate showing protrusion: (a) focal plane near substrate (b) focal plane near tip of frozen droplet

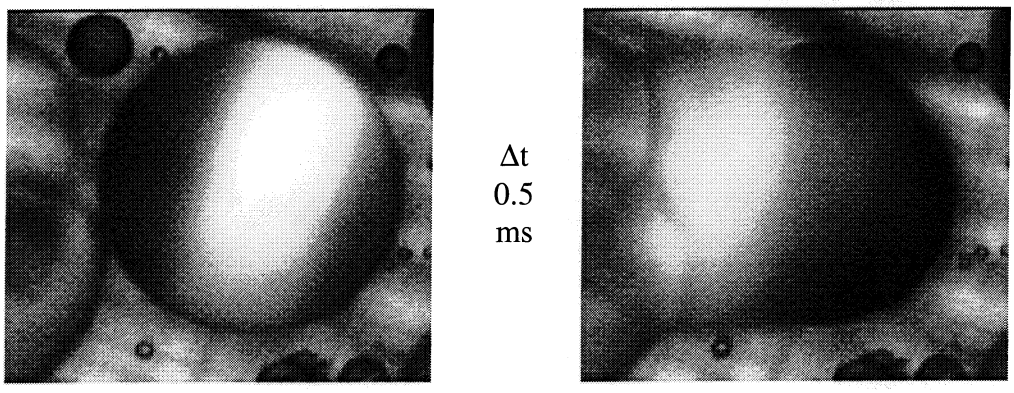

a: t=0

Δt
0.5
ms

b

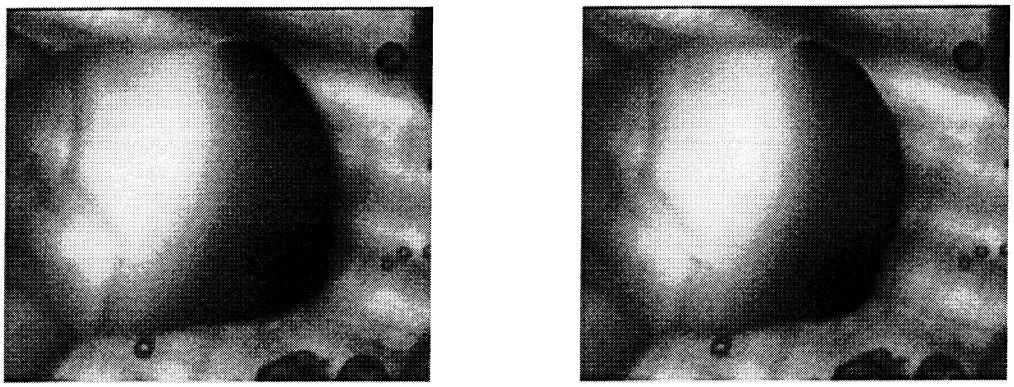

c

d

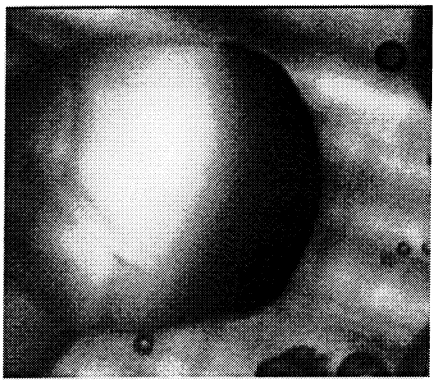

e

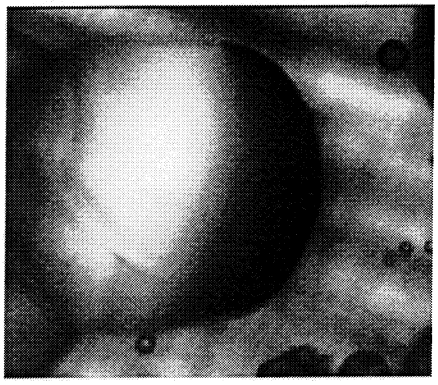

f

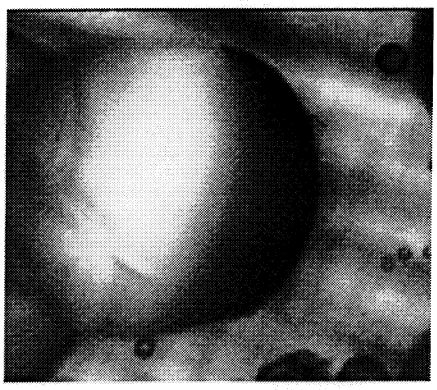

g

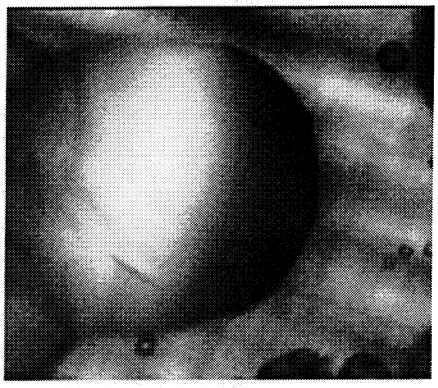

h: t=3.5 ms

Figure 5.11 Initiation of freezing

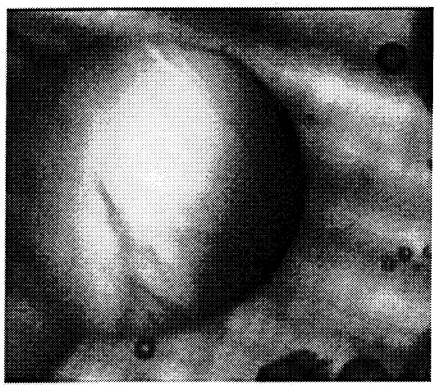

a: t=53.5 ms

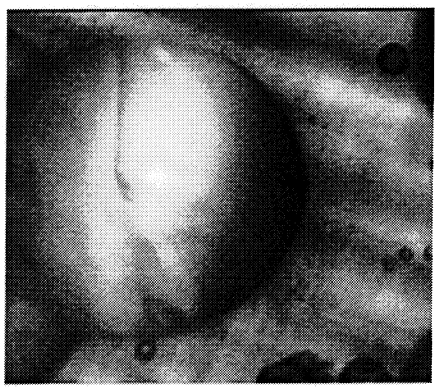

b

c

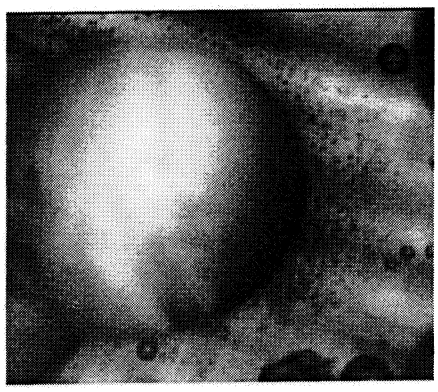

d

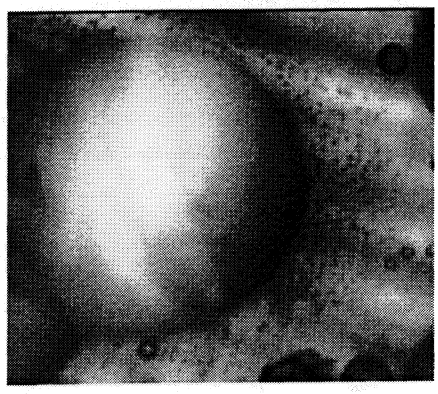

e

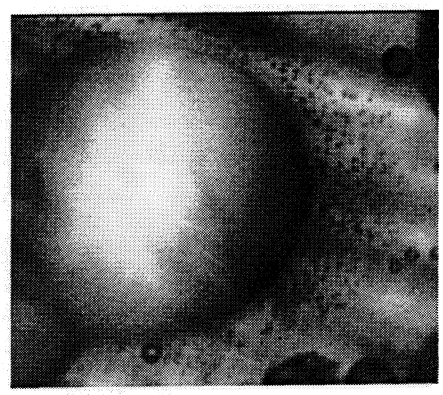

f

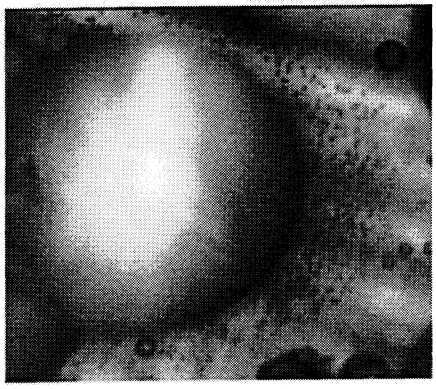

g

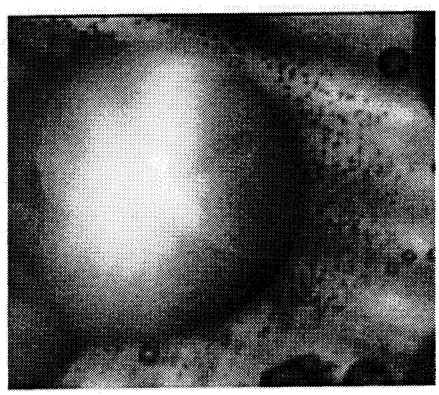

h

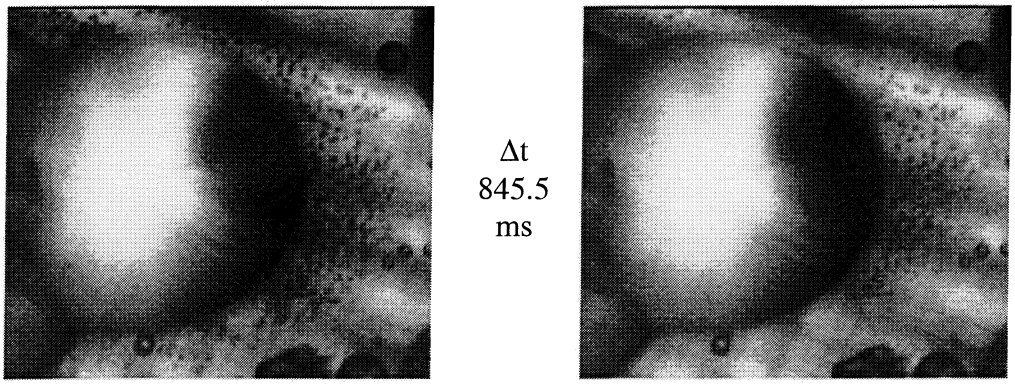

i: t=453.5 j: t=1300 ms

Figure 5.12 Droplet freezing and satellite droplet formation-substrate is the focal plane

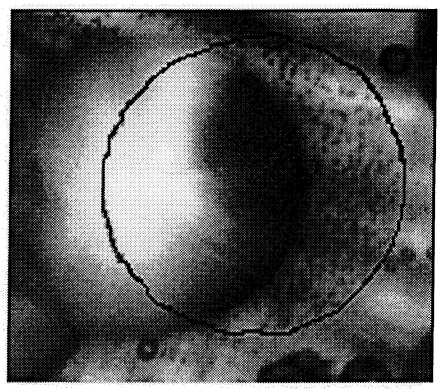

t=453.5

Figure 5.13 Superposition of water droplet position and frozen droplet

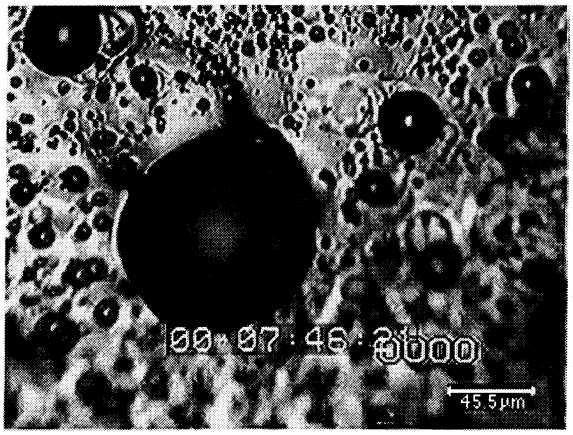

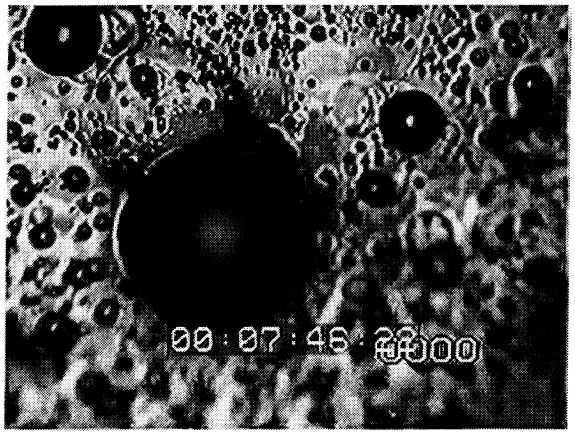

a b

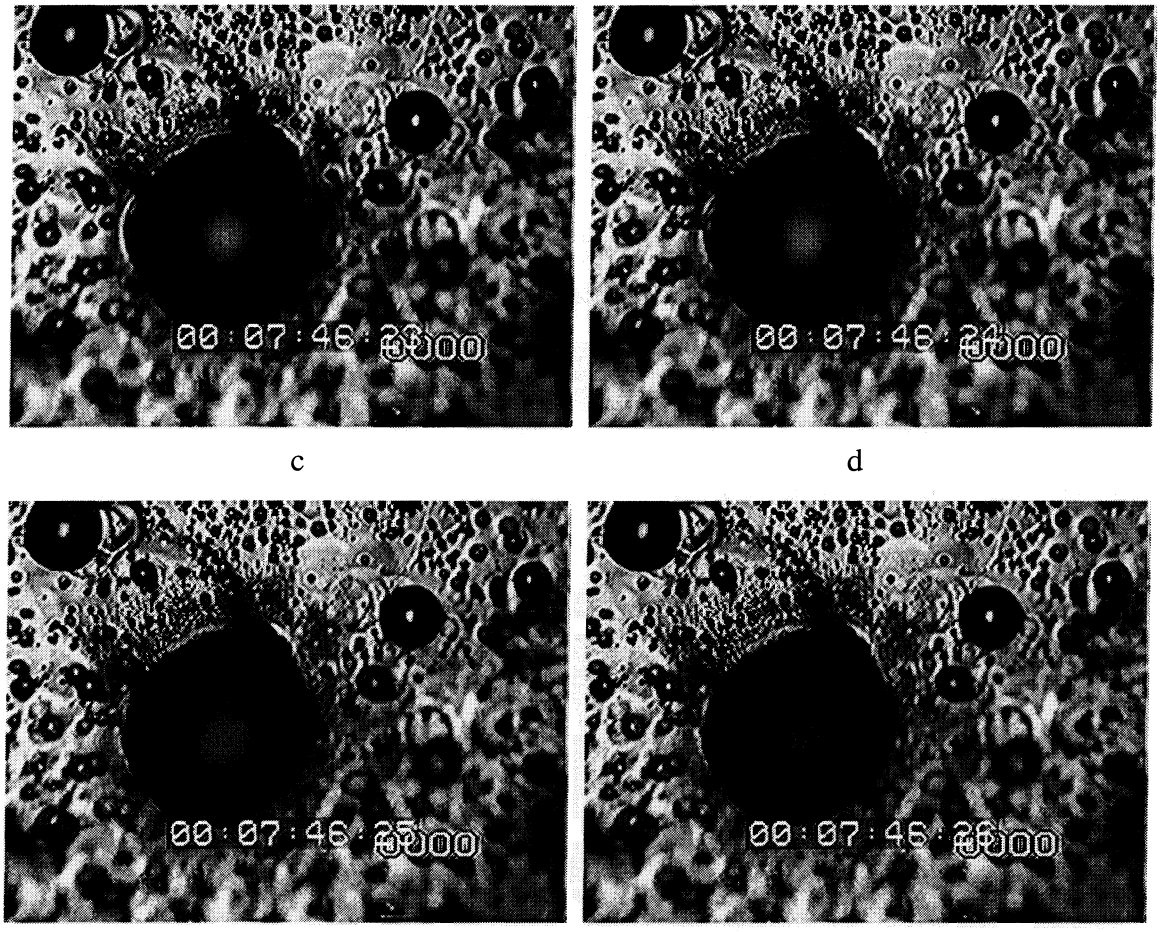

c d

e f

Figure 5.14 Freezing water droplet on frozen cyclohexane

6 Early and Mature Frost Growth Trends as a Function of Substrate

6.1 Introduction

Once the condensate on the substrate has frozen, no further condensation onto the bare substrate between frozen droplets is possible because of the vapor pressure difference between water and ice at the same temperature. Rather, water vapor ablimates onto the frozen droplets and frost spires form during the early growth period. These frost spires predominantly grow normal to the substrate along the vapor pressure gradient in the concentration boundary layer. After some period, the temperature of the tips of these small crystals increases and the equilibrium water vapor pressure at the tips also increase. Then, diffusion of water vapor into the frost layer becomes significant and horizontal crystal growth occurs within the layer. This horizontal growth begins the transition from the early growth to the mature frost growth period. Trends during the early and mature growth periods are examined as a function of substrate in Sections 6.2 through 6.4.

6.2 Early Growth Properties

On the hydrophilic substrate, the condensation period ends abruptly as the freezing front propagates quickly through the thin liquid film covering the substrate. An image of the frozen condensate on a silicon wafer (hydrophilic substrate) is shown in Fig. 5.2. The resulting frost growth can be seen in Fig 6.1. In contrast to the frost growth that occurs on the protrusion formed when a droplet on a hydrophobic substrate freezes, frost grown on the hydrophilic substrate has many possible locations to initiate growth and

densify. In Fig. 6.2 a side view of the crystals growing up from a hydrophilic substrate is shown.

In Fig. 6.3, frost spires emerging from the top of almost every frozen droplet on the hydrophobic PTFE are evident as bright hexagonal shapes. Looking down on the droplets, a single frost spire was emerging from the center of each droplet. It is obvious from Fig. 6.3 that the density and number of frost spires growing up from the condensate creating the initial frost layer was dependent on the number and distribution of droplets on the substrate. In this particular image, the volume fraction of the dendritic crystals growing up from the droplets was approximately 5%. In Fig 6.4, additional images of the early growh on PTFE are shown. Again, the number of frost spires corresponded one to one with the number of droplets on the substrate at the end of the condensation period. In Fig 6.4, three images of frost spires in the early growth period for different substrate temperatures are shown. As the temperature of the substrate decreased, the number of spires growing up from the substrate increased. Examing Fig. 4.7, where the number of droplets per area as a function of substrate temperature are shown, there is a larger number of droplets present at the end of the condensation period for lower supbstrate temperatures. With larger diameter droplets comes a smaller number of drops on the substrate, and the spires were observed to grow more parallel to the substrate, resulting in a larger observed diameter as seen in Fig 6.4. Growth parallel to the substrate within the layer is not as condusive to the development of a frost layer with a high thermal conductivity as growth perpendicular to the substrate.

One additional characteristic of the early frost growth on a hydrophobic substrate is revealed by imaging the frost from the underside; the space between the frozen

condensate fills in slowly. In Fig. 6.5 (a), the frozen droplets were observed pendent from a hydrophobic coated clear glass slide. In Fig. 6.5 (b) and (c), the substrate coverage was imaged with approximately 50 minutes between images. The absolute humidity was 0.0125 kg/kg with an airflow rate of 0.7 m/s. The substrate temperature was not measured but was estimated to be between –10 and –25°C. Comparing Fig. 6.5 (b) and (c), a considerable amount of coarsening occurred; however, the percentage change of substrate covered was too small to measure. These images indicate that the substrate has little interaction with the ablimation process after the condensation period.

6.3 Height During the Mature Growth Period

The thickness of frost has been found to be a function of substrate contact angle by Seki *et al.* (1984) and Dyer *et al.* (2000). The pertinent points made by Dyer *et al.* (2000) will be repeated here for completion. For three of the six data sets of that study, half of the width of the test channel was covered with either a 0.89 mm (0.035") thick steel coated with PTFE, or with 0.18 mm (0.007") thick aluminum coated with a hydrophilic coating. The other half of the channel was covered with 0.18 mm (0.007") thick bare aluminum to provide a reference substrate, see Fig. 2.2. For the other three tests, the hydrophilic substrate covered the entire channel. Note that the difference in material and thickness of the test substrates has a negligible effect on the surface temperature for the conditions of these tests. The advancing and receding contact angle measurements for these substrates are given in Table 2.7. The experimental range is expressed in the non-dimensional parameters defined in the nomenclature: $6.0\text{x}10^{-3} < Ja < 7.4\text{x}10^{-3}$, Le~0.91, $0.95 < \theta < 2.0$, $3.0\text{x}10^{-3} < \Phi < 5.9\text{x}10^{-3}$, $0 < Fo < 40$, $1000 < Re <$

1600. For convenience, Table 2.1 gives the environmental parameters in dimensional form, along with a summary of measurement uncertainty for each.

In Fig. 6.6 the dimensionless thickness as a function of the square root of the environmental time for the hydrophilic (coated aluminum), and hydrophobic (PTFE coated steel) substrates is shown. The data were plotted this way to normalize the effect of different environmental conditions. A least-squared-error fit to the hydrophilic data produced a slope of 1.13 ±0.03 while a least-squared-error fit to the hydrophobic data produced a slope of 0.81 ±0.03. The slope of the control data was 1.01 ±0.07. The slope of the data presented by Storey and Jacobi (1999) was 1.0 ±0.06 and is represented by the line in Fig. 6.6. The difference in slope between the hydrophilic and hydrophobic data and the control data represents a significant difference in growth rate. In the model used to interpret the macroscopic data, the empirical quantity β was determined experimentally. In deriving Eqs. (2.1)-(2.3), β has physical meaning as the slope of the thermal conductivity - density curve (Storey and Jacobi 1999). The difference in the slope, β, between the frost grown on the hydrophilic and hydrophobic substrate indicates that the frost grown on the hydrophilic substrate has a higher thermal conductivity. The microscopic experiments showed that the frost grown on the hydrophobic surface at least initially, was a more porous, frost layer. The hydrophilic surface on the other hand, grew a more uniform layer. These observations are consistent with those observed in the mature growth period. The hydrophilic data consist of 55 height measurements taken during 4 separate tests while the hydrophobic data consist of 26 height measurements taken during 2 tests.

6.4 Mass Deposition During the Mature Growth Period

The measurements of condensate acquired with the microscope during the condensation period reveal that the droplets on the hydrophobic substrate were taller and the effective density was lower. When the droplets on the hydrophobic substrate froze, a protrusion formed on the top of the droplets which served as a location for a frost spire. The form and structure of the frozen condensate on the hydrophobic substrate and the greater penetration into the concentration boundary layer would result in a larger amount of water mass being deposited on the hydrophobic substrate. This observation is confirmed by measurements taken in the macro-wind tunnel. After 1860 s of growth, the mass deposited on PTFE is in general, greater than that deposited on kapton by approximately 14% as seen in Fig. 6.7. The discrepancy in mass deposited reveals that the mass deposition rate was higher on substrates with higher contact angles, during the condensation period and during the early growth period. This difference in the mass deposited is most likely caused by the increase in effective surface area caused by the shape of the droplets on the more hydrophobic substrates.

As the frost layer grew and became more uniform, the mass deposition rate on the frost layer on the hydrophobic substrate decreased below the rate on the hydrophilic substrate. The decrease in mass deposition rate can be seen in Fig. 6.8 where the mass deposited after 4000 s appears to be independent of the substrate surface energy and in Fig. 6.9, where the mass deposited on the hydrophilic substrate has surpassed that on the hydrophobic substrate after 7000 s. This change in deposition rate during the mature growth period was most likely caused by a difference in the mass transfer driving potential. The hydrophilic substrate had a lower frost surface temperature (which results

in a lower concentration of water vapor at the frost surface) because of a higher thermal conductivity, which will be discussed in Chapter 7.

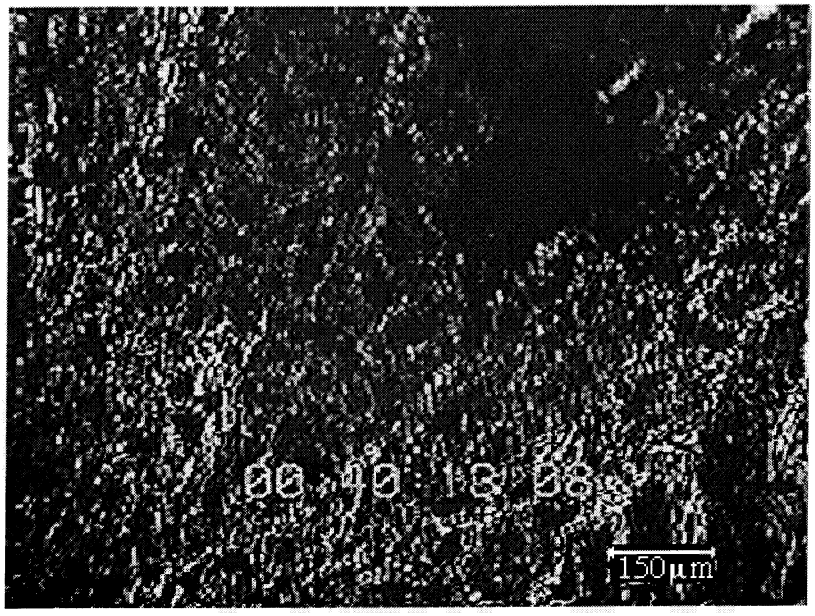

Figure 6.1 Early growth of frost on a silicon wafer

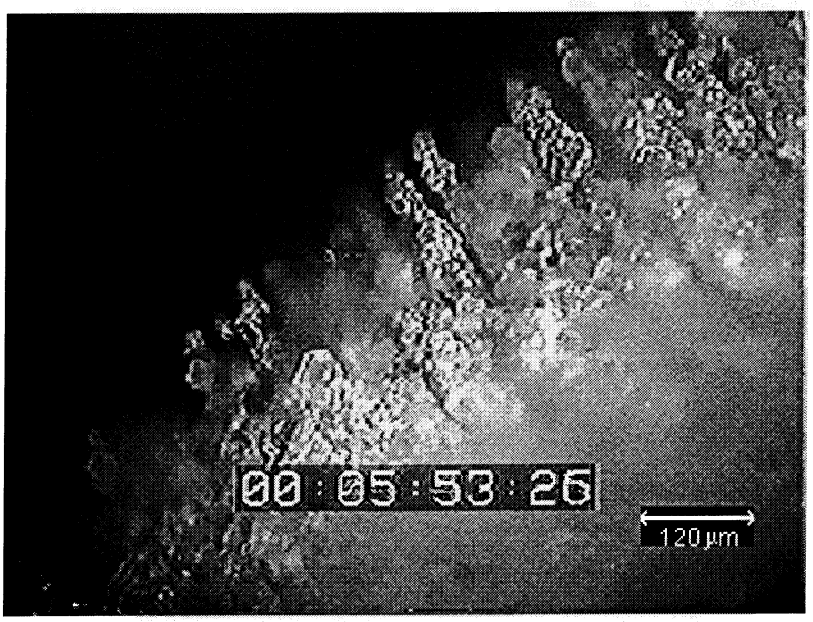

Figure 6.2 Early growth of frost on a silicon wafer, side view

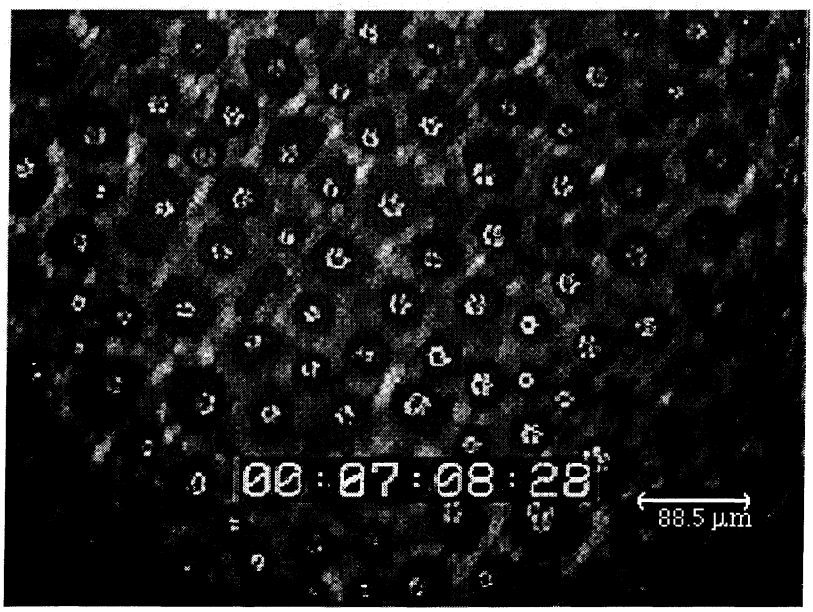

Figure 6.3 Early growth of frost on PTFE substrate, free convection

a

T_w=-11.0, T_a=11.2, ω = 0.00497 V=0.93 m/s

b

T_w=-17.5, T_a=11.2, ω = 0.00498, V=0.93 m/s

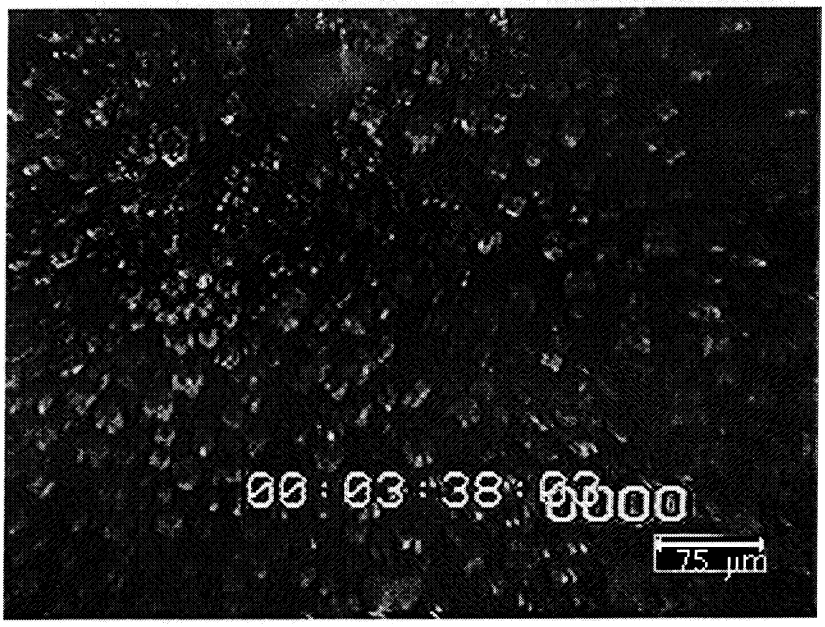

c

T_w=-25.1, T_a=10.5,ω = 0.00499, V=0.93 m/s

Figure 6.4 Early frost growth on PTFE substrate: (a) T_w=-11.0, (b) T_w=-17.5, and (c) T_w=-25.1

a

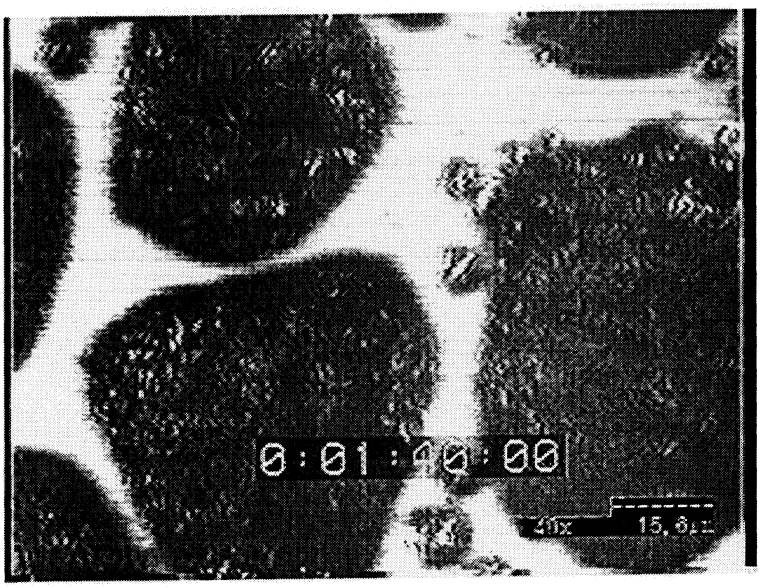

b

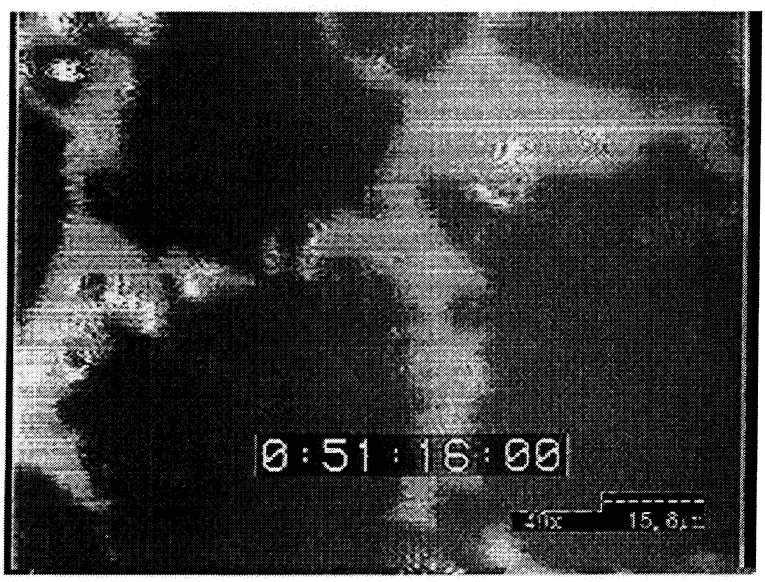

c

Figure 6.5 Frost growth observed from beneath pendant drops: (a) condensate, (b) shortly after freezing and (c) after 51 minutes

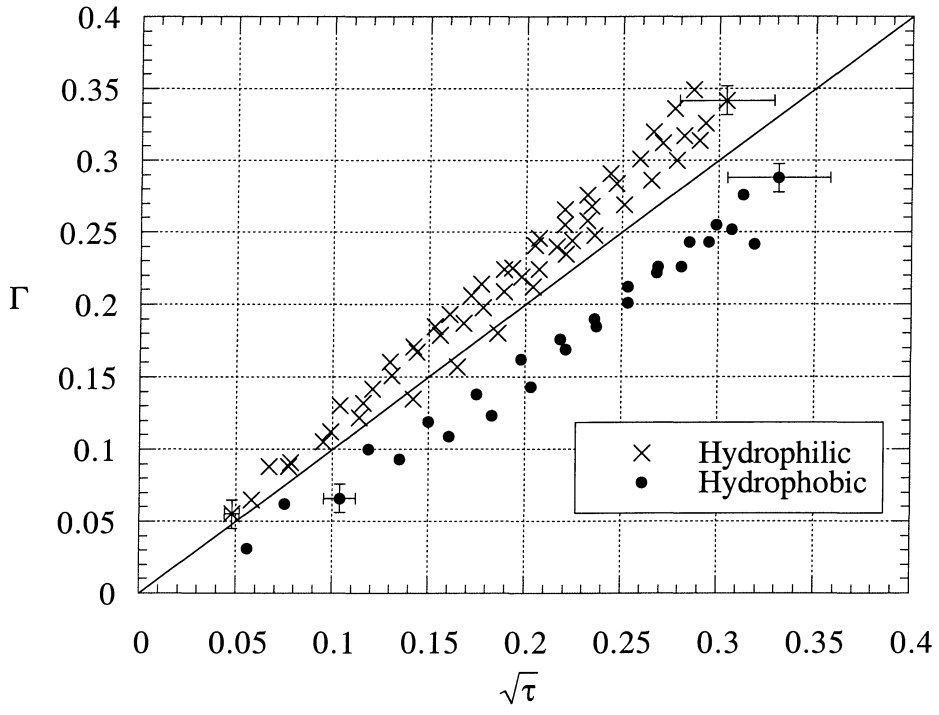

Figure 6.6 Effect of hydrophobicity on height: dimensionless height versus the square root of environmental time (Dyer *et al.* 2000)

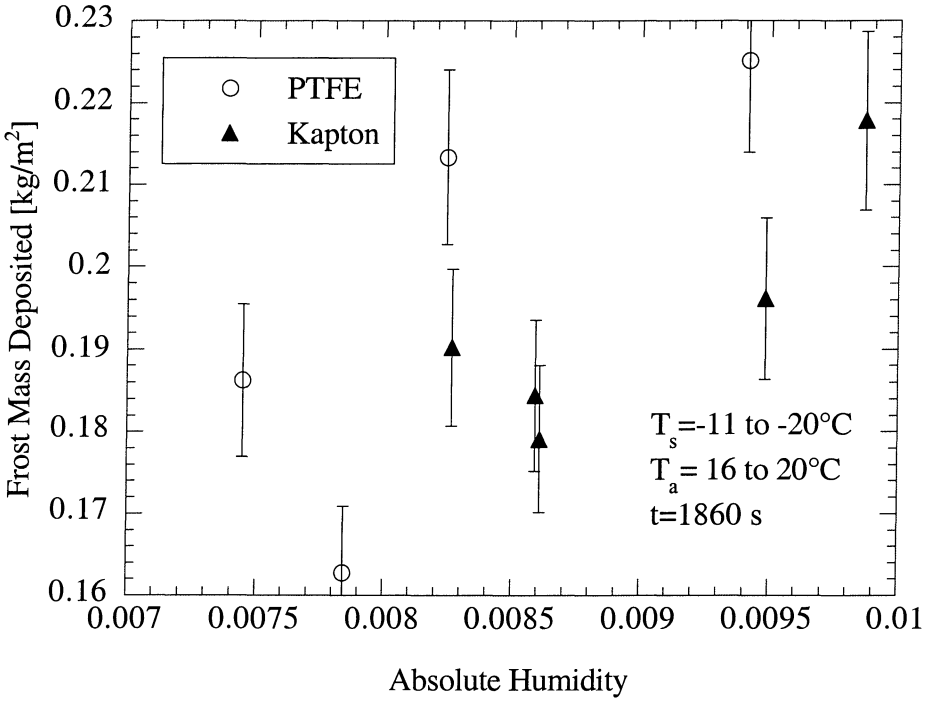

Figure 6.7 Mass deposited after 1860 s on PTFE and kapton versus absolute humidity

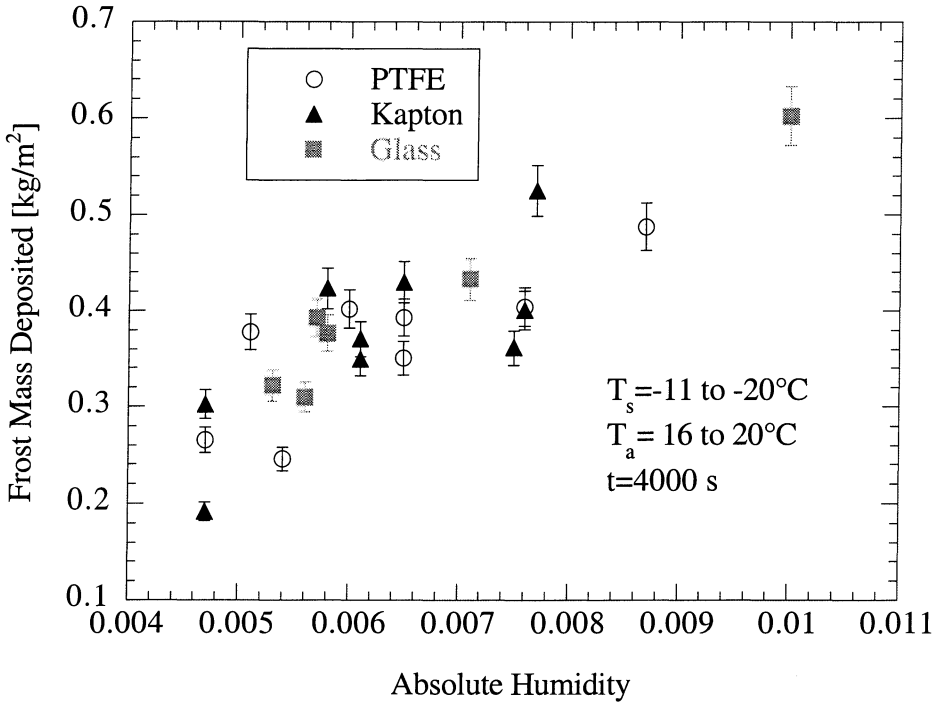

Figure 6.8 Mass deposition after 4000 s on PTFE, kapton and glass substrates

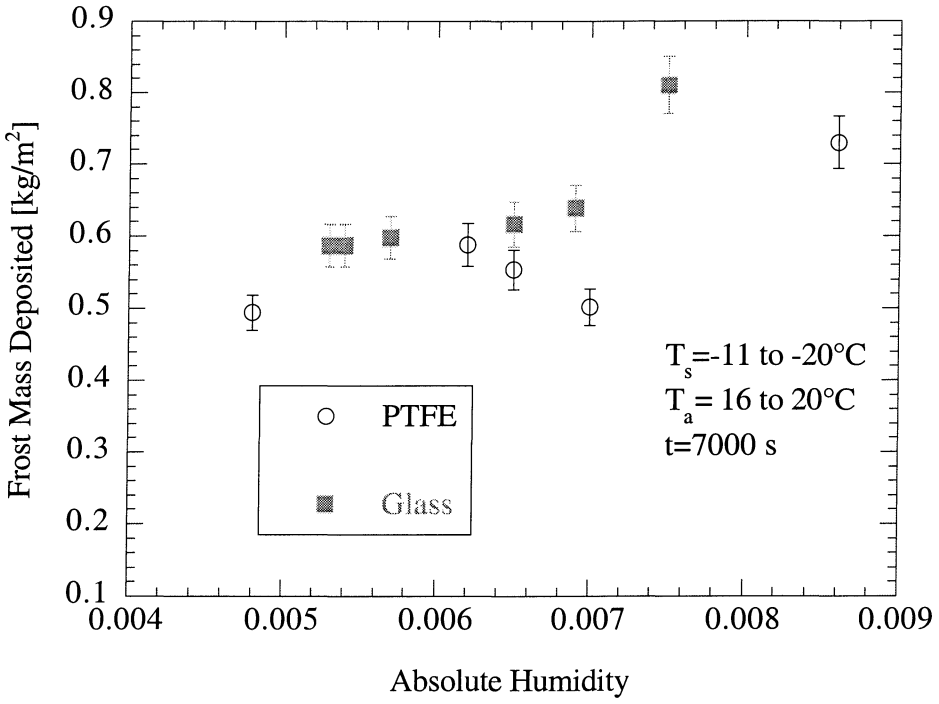

Figure 6.9 Mass deposition after 7000 s on PTFE and glass substrates

7 Substrate and Temperature Influence on Mature Frost Properties

7.1 Introduction

Numerous observations and measurements have been presented concerning the effect the substrate contact angle has on the growth of frost. The primary influence that the substrate has on vapor deposition occurs during the condensation period; however, there is a frost property dependence on the substrate that persists at least several hours into the frost growth process. In this chapter, the important observations are reviewed before a hypothesis is presented to explain the interaction between the substrate and frost properties. A numerical frost growth model is used to bolster the proposed hypothesis. Because of the unique opportunity to study frost properties as a function of the initial condition, the hypothesis presented is extended to explain the frost growth rate as a function of substrate temperature.

7.2 Review of Experimental Results and Observations

A paradox presents itself upon examining the condensation and early growth data: initially the thickness of the frost on the hydrophobic substrate is greater than that on the hydrophilic substrate and the density of the frost on the hydrophilic substrate is larger than that on the hydrophobic substrate - opposite to what is observed for mature frost growth. As an example, a reconstruction of the condensate on the substrate immediately preceding the freezing event is shown if Fig. 7.1. The condensate is approximately 2 times taller on the hydrophobic PTFE than that on the glass, while the estimated density

of condensate on the PTFE is approximately 42% of that on the hydrophilic substrate. Water is seen to cover 86% of the hydrophilic substrate but only 34% that of the hydrophobic substrate. The volume of water as a percentage of total volume between a plane above the substrate and the surface of the substrate is shown in Fig. 7.2. The shape of the curves shown in Fig. 7.2 depends on the contact angle on the substrates. The conditions for these two experiments were similar: a substrate temperature of –10.2 and –11.4°C, an air temperature of –0.24 and –1.24°C, an air flow rate of 0.93 m/s, and an absolute humidity of 0.003 and 0.002 for the hydrophobic and hydrophilic substrate, respectively. The condensation periods for these two tests were similar, 300 seconds for the PTFE substrate and 270 seconds for the glass substrate. There exist substrate temperature and absolute humidity conditions that make frost properties less dependent on the substrate contact angle, for example, when either a very sparse amount of liquid water forms on the substrate or when the substrate is flooded at the end of the condensation period, the contact angle plays a less important role.

The condensation period naturally ends at the onset of freezing. The morphology created during freezing was examined in detail in Chapter 5. On a hydrophobic substrate, a protrusion forms at the top of the droplet during freezing. A single frost dendroid grows from each of these droplets. On a hydrophilic substrate, multiple frost spires grow from the large pools of frozen condensate. As such, the distance between vertical frost spires on a hydrophilic substrate is hypothesised to be lower than that on the hydrophobic substrate.

The mature frost thickness as a function of time for frost grown on two different substrates is shown in Fig. 7.3. The hydrophilic substrate is glass with a water advancing

contact angle of 40° and a receding contact angle of 29°, while the hydrophobic substrate was PTFE with an advancing contact angle of 106° and a receding contact angle of 84°. The air velocity for both tests was 1.2 m/s. The frost grown on the hydrophilic substrate is shown to have grown over 25% thicker after 3500 seconds than the frost grown on the hydrophobic substrate. There is a difference of approximately 500 seconds in the condensation period for these two substrates. By comparing the frost thickness on the hydrophobic substrate at 3500 seconds with the thickness of frost on the hydrophilic substrate at 3000 s, the difference in the length of condensation period can be removed; however, the frost on the hydrophilic substrate was still 23% thicker. Interestingly, the density of the frost grown on the hydrophilic substrate was 14% *lower* than that on the hydrophobic substrate (the uncertainty in the density measurement was 5.8% and 7% for frost grown on the hydrophilic and hydrophobic substrates, respectively).

7.3 Analysis

The experimental observations clearly show that the density and thickness of frost are not only dependent on the substrate contact angle, but that there is a time dependent variation in growth rate and densification which results in an intersection of both the density and thickness versus time curves for the two substrates (not necessarily occurring simultaneously). I hypothesize that the difference between the frost layers grown on a hydrophobic and hydrophilic substrate is caused by the difference in thermal conductivity between the layers. The difference in thermal conductivity is caused by a difference in frost structure caused by the distribution of condensate on the substrate prior to freezing. The distribution of condensate determines the locations and number of frost spires. The

conductivity of the frost layer is affected by the spacing of these spires. Closer spaced spires result in frost growth which is more normal to the substrate and has a higher effective conductivity. As the frost layer grows and densifies, the effect of the differences in the initial condensation is expected to decrease; however, frost only grows on existing frost and the "foundation" of the frost layer influences the resulting structure.

This morphological characteristic, the condensate distribution, explains why the thermal conductivity of the frost layer grown on the hydrophilic substrate is appreciably higher than that of the frost layer grown on the hydrophobic substrate. Higher conductivity results in a smaller temperature gradient across the frost layer and a lower frost surface temperature. The smaller temperature gradient causes a larger portion of the convected water vapor to be deposited on the surface of the frost (increasing the thickness), rather than diffusing into the layer. In addition, the driving potential for mass transfer to the frost surface is larger. In the limit of the Biot number of the frost layer, $\frac{h\delta_f}{k_f}$, approaching zero, all of the water vapor will be deposited on the surface of the frost layer. The result of a small Biot number is readily seen by a mass balance at the frost-air interface, as shown in Eq. (7.1). Note that the water vapor density gradient within the layer is dependent on the temperature gradient, assuming the saturation ratio within the frost layer is unity.

$$h_m\left[\omega_\infty - \omega\left(z = \delta_f^+, t\right)\right] = D_{eff}\frac{\partial \rho_v\left(z = \delta_f^-, t\right)}{\partial z} + \rho_f \frac{d\delta_f}{dt} \tag{7.1}$$

To examine the above hypothesis quantitatively, the mature growth model proposed by Tao and Besant (1993a) will be considered. This model is based on the conservation of mass and energy, and the listing of the program for this model is given in Appendix B. Initial conditions are acquired by observing the incipient growth of frost under a scanning confocal microscope. The details of the numerical model will be quickly reviewed for completeness, then explanations of the initial conditions and conductivity are given before the results of the simulation are examined and compared to experiments. For frost growth on a flat plate, only transport in the direction normal to the plate is considered. The energy and mass conservation within the frost layer yield

$$\rho_f c_p \frac{\partial T}{\partial t} + \dot{m}\lambda_{sg} = \frac{\partial}{\partial z}\left(k_{eff} \frac{\partial T}{\partial z} \right) \qquad (7.2)$$

and

$$\frac{\partial(\varepsilon_a \rho_v)}{\partial t} - \dot{m} = \frac{\partial}{\partial z}\left(D_{eff} \frac{\partial \rho_v}{\partial z} \right) \qquad (7.3)$$

where the phase change rate is related to the volume fraction by

$$\frac{\partial \varepsilon_b}{\partial t} + \frac{\dot{m}}{\rho_{ice}} = 0 \qquad (7.4)$$

and

$$\varepsilon_a + \varepsilon_b = 1 \qquad (7.5)$$

The boundary conditions for the energy conservation equation are a convection condition at the frost surface and an isothermal condition at the plate surface, T_w. For the mass balance equation, the boundary conditions are that no mass is transferred into the plate (the derivative of the mass concentration must be zero at the substrate surface, z=0)

and there is a convective condition at the frost surface. The vertical growth is computed by Eq. (7.1), with frost properties assigned in a way consistent with available experiments. The diffusion of water vapor and densification of the frost layer needs to be quantified. The effective diffusivity is taken as

$$D_{eff} = \varepsilon_a D_{AB} \tag{7.6}$$

Tao and Besant (1993a) used a correlation for the conductivity of frost which depended solely on density and was developed by Yonko and Sepsy (1967).

$$k_{eff} = 0.02422 + 7.214\text{x}10^{-4}\rho_f + 1.1797\text{x}10^{-6}\rho_f^2 \tag{7.7}$$

where ρ_f is in kg/m^3 and k_{eff} is in W/m-K. The conductivity of a porous, fibrous medium such as frost depends inherently on the structure and orientation of the fibers or crystals in this case, as well as the porosity.

$$k_{eff} = k_{eff}(\text{structure}, \varepsilon_b) \tag{7.8}$$

Two limiting cases elucidating the effect of structure on conductivity are that of two media in series or parallel. For values of porosity typical to frost, the conductivity of these two extreme cases can differ by a factor of 20. The microscopic observations of the initiation of the frost layer reveal several significant differences in frost structure for frost grown on hydrophilic versus hydrophobic substrates and suggest a dependence of frost

growth rate on substrate contact angle. The orientation of the frost crystal relative to the macroscopic direction of heat flow, Ω, determines the effect that the structure has on conductivity.

$$k_{eff} = k_{eff}(\Omega, \varepsilon_b) \tag{7.9}$$

Bauer (1993) has determined an expression for the conductivity of a fibrous media based on porosity and the average orientation of the fibers.

$$\left(\frac{k_{eff} - k_{ice}}{k_a - k_{ice}}\right)\left(\frac{k_{eff} + \left[\left(1-\sin^2\Omega\right)/\left(1+\sin^2\Omega\right)\right]k_{ice}}{k_a + \left[\left(1-\sin^2\Omega\right)/\left(1+\sin^2\Omega\right)\right]k_{ice}}\right)^{-\left(\frac{\sin^2\Omega}{1+\sin^2\Omega}\right)} = 1-\varepsilon_b \tag{7.10}$$

For fibers parallel to the macroscopic direction of heat flow, $\Omega = 0$, and $\Omega = 90°$ for fibers perpendicular to the macroscopic direction of heat flow. The value of conductivity predicted by Eq. (7.7) for a frost density between 50 and 500 kg/m^3 is within 1.5% of the value predicted by Eq. (7.10) with the average ice crystal orientation set at $\Omega = 53°$. This agreement indicates that the frost conductivity can be approximated by an average crystal orientation more parallel to the substrate than perpendicular.

Single crystal growth has been systematically analyzed and found to depend on crystal temperature and degree of supersaturation. Frost however, is a complex, polycrystalline material and a product of local heat and mass transfer as well as surface kinetics. The proximity of neighboring crystals can affect the availability of water vapor and the direction of growth, this proximity of crystals is the mechanism by which the

substrate contact angle affects frost properties. For the hydrophobic substrate, there is a relatively large distance between crystals growing up from the substrate favorable to horizontal growth to fill in the layer. For a hydrophilic substrate the spacing between vertical spires is smaller, not limited by the location of frozen droplets since there is a frozen layer covering the substrate.

In the early growth period, the orientation of crystals is observed to be predominantly normal to the substrate and a value for the average crystal orientation closer to zero is adopted, Ω_i=25°(the conductivity is a weak function of fiber orientation below 25°). As the crystal layer grows and become multifaceted, the average orientation of the crystals approaches that of the mature frost layer and the equation proposed is

$$\Omega = (\Omega_m - \Omega_i)\left(1 - \exp\left(-\frac{\sqrt{\tau}}{0.1}\right)\right) + \Omega_i \qquad (7.11)$$

where Ω_m and Ω_i are the mature and initial average crystal orientations respectively and τ is the environmental time proposed by Storey and Jacobi (1999). The exponential form of this equation provides a smooth transition from the structure encountered in the early growth period to that expected in the mature growth period. The time constant of 0.1 is chosen on the basis of the observation of the time necessary for transition from the early growth period to the mature growth period (Storey and Jacobi 1999).

The early frost growth period also differs from the mature growth period in terms of the number of possible locations for water vapor deposition. Microscopy reveals that the initial volume fraction of frost appearing from the frozen condensate is relatively low. Frost is deposited directly onto existing frost so the increase in height between time steps

of the model maintains this low density. The deposition of water vapor onto the frost layer is most intense during the early growth period since the driving potential between the free stream and the frost surface is the highest. The low frost density and high deposition rate accounts for the fast growth rate during the early growth period.

The equation used to compute the density of the new frost layer deposited is similar to the matching equation for crystal orientation and is given by

$$\varepsilon_B = (\varepsilon_{Bm} - \varepsilon_{Bi})\left(1 - \exp\left(-\frac{\sqrt{\tau}}{0.1}\right)\right) + \varepsilon_{Bi} \qquad (7.12)$$

where ε_{Bi} and ε_{Bm} are the early and mature growth density used to compute the new growth on the frost layer. On the basis of observations made in Chapter 5 as well as those made by Tao and Besant (1993a), a value of 0.02 is proposed for ε_{Bi} and a value of 0.12 for ε_{Bm}.

While simulating the frost growth, the average value of crystal orientation, Ω_m, was adjusted to fit the observed trends. Other than the initial conditions, this was the only parameter which was changed from the hydrophilic to hydrophobic simulation. The value of Ω_m is 45° for a hydrophilic substrate and 65° for a hydrophobic substrate. The simulated frost height is plotted versus the experimental data in Fig. 7.4. The temporal axis for the hydrophobic data have been offset by 500 seconds to account for the long condensation period. The simulated density is approximately 20% less than the experimental data. The density of frost on the hydrophilic substrate starts higher than that on the hydrophobic substrate (because it is set that way for the initial condition of the

model); however, at the end of the simulation, the density on the hydrophilic substrate is 12% lower than that on the hydrophobic substrate. Recall that the experimental results revealed a 14% difference in the densities.

7.4 *Extension of Observations to Substrate Surface Temperature/ Conductivity Dependence*

As reported in Chapter 1, the conductivity of the frost layer is usually correlated with frost density. Of course, this is a correlation of convenience since it has been difficult to examine the conductivity of frost as a function of structure. This correlation is in error when calculating the conductivity of frost as a function of substrate contact angle, since the lower density frost found on a hydrophilic substrate has a higher conductivity than that found growing on a hydrophobic substrate under identical environmental conditions. Likewise, frost growing at a lower substrate temperature has a higher conductivity and lower density (Mao *et al.* 1993). The higher conductivity and lower frost density at lower substrate temperatures is readily seen by examining the functionality of the correlation for frost density and conductivity proposed by Mao *et al.* (1993). The density changed with plate temperature and time as

$$\rho \propto \left(\frac{T_{tp} - T_w}{T_a - T_w} \right)^{-0.728} t^{0.147} = T^{*-0.728} t^{0.147} \qquad (7.13)$$

and the conductivity changed as

$$k \propto \left(\frac{T_{tp} - T_w}{T_a - T_w} \right)^{0.901} t^{0.791} = T^{*0.901} t^{0.791} \qquad (7.14)$$

where $0.24<T^*<0.51$ and the conductivity of the frost layer was determined by assuming that the frost surface temperature was at the triple point of water. As an example, take T^* to be 0.30 and 0.45 for two different substrate temperatures, all other conditions held constant. The density at any given time on the colder substrate, $T^*=0.45$, is 74% of that on the warmer substrate, $T^*=0.30$, while the conductivity of the frost is 44% greater on colder substrate than the warmer.

Although the characteristics of crystal growth have been reported to be a function of temperature and supersaturation (Hobbs 1974), the measurements of these reports were conducted on crystals not competing for water vapor. The growth of crystals growing in a frost layer is constrained by temperature and the availability of water vapor. Because of this, crystals tend to grow along the vapor pressure gradient. Following the hypothesis explaining the effect that the substrate has on frost properties, the smaller, closer spaced droplets seen on a colder substrate are going to foster the development of a frost layer with a higher conductivity because the growth of the crystals will be predominantly normal to the substrate with less horizontal growth needed to fill in the space between droplets.

7.5 Closure

The trends observed for the density (or mass deposited) and thickness of frost as a function of substrate are hypothesized to be caused by a difference in the thermal conductivity of the frost layers. The number and location of frost spires has been shown to be dependent on the condensate distribution. The number density of frost spires emerging from the condensate affects the direction of growth and densification of the

frost layer. Therefore, the condensate distribution affects the structure of the frost layer. A correlation for the conductivity of a fibrous material based on structure has been implemented in a numerical model for frost growth to determine if a change in the thermal conductivity of the frost layer could affect the observed differences in thickness and density. The trends of thickness and density observed for mature frost growth are reproduced by the model with the only variable being the average orientation of the crystals. The initial conditions on the hydrophobic and hydrophilic substrate are commensurate with observations. The hypothesis that the conductivity is affected by the distribution of condensate is also bolstered by the trends observed for the condensate distribution and conductivity of the frost layer as a function of substrate temperature, which are consistent with this theory.

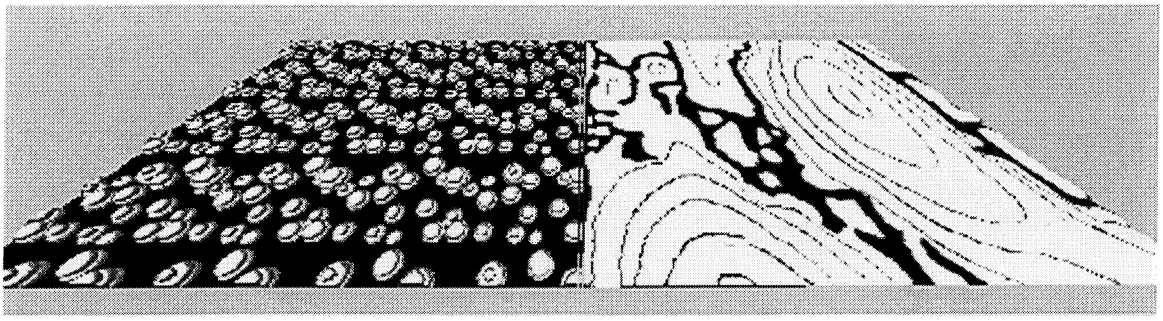

Figure 7.1 Condensation on PTFE (left) and glass (right) substrates, immediately preceding freezing

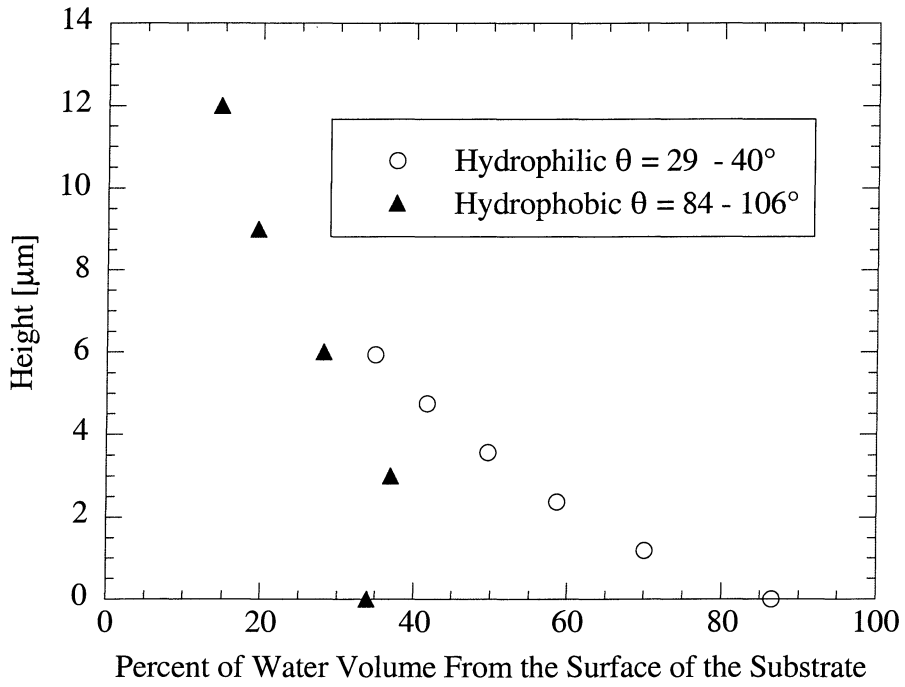

Figure 7.2 Volume fraction of water between the substrate and a plane above the substrate

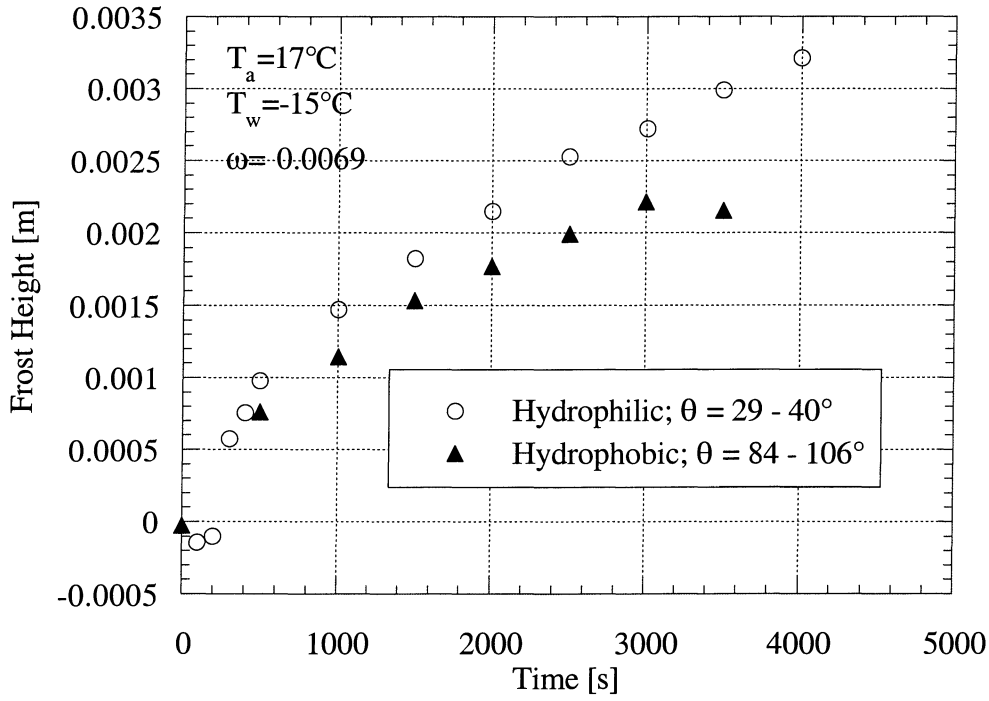

Figure 7.3 Frost thickness versus time on hydrophilic and hydrophobic substrates

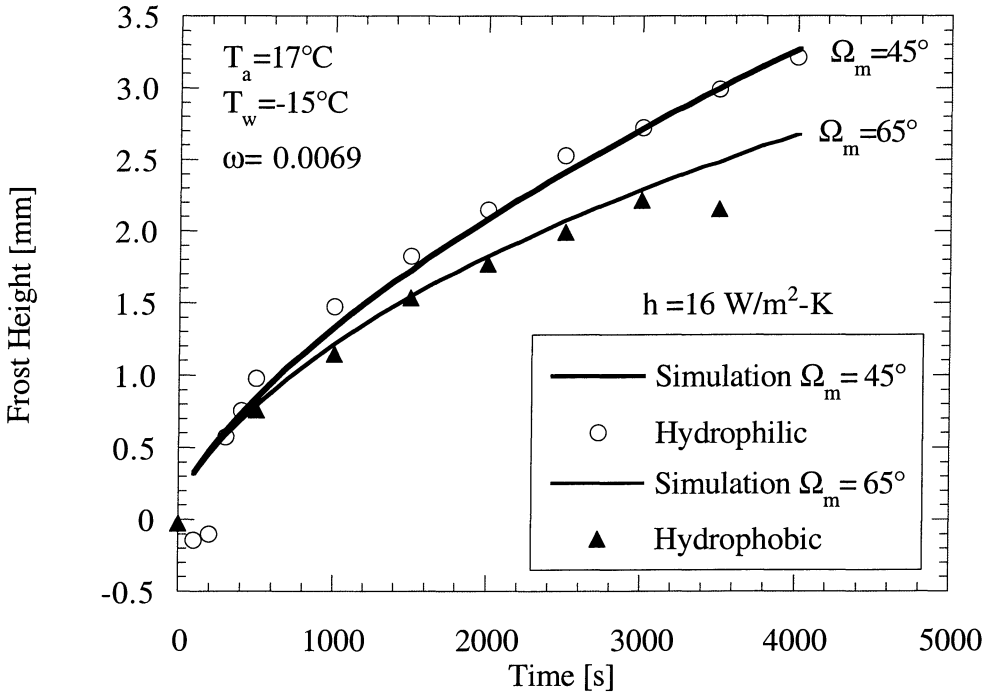

Figure 7.4 Simulation versus experimental results

8 Conclusions and Recommendations for Future Work

8.1 Conclusions

Through a careful experimental investigation of frost growth on a flat substrate exposed to a laminar grazing airflow, new insights into how condensate affects mature frost growth properties have been gained. The condensation period, freezing event, and early frost growth period have been examined in detail, and classical nucleation theory, analysis of heat and mass transfer, and numerical simulation have been employed to interpret the data and explore hypothesized physical mechanisms.

Two possible scenarios for frost inception were identified, condensation and ablimation frosting. Experiments were conducted to determine the demarcation in environmental conditions which favors one frost initiation scenario over the other. The conditions leading to condensation frosting were established. The duration of the condensation period was found to decrease with decreasing substrate temperature, substrate contact angle, and with increasing mass transfer driving potential. The distribution of condensate at the end of the condensation period was quantified as a function of the substrate contact angle and environmental parameters. The effective density of the condensate on a hydrophilic substrate was found to be higher and the height of the condensate was lower than that on a hydrophobic substrate. The percentage of the substrate covered by condensate was higher for a hydrophilic substrate.

The initial frost structure is a function of condensate contact angle. On a hydrophobic substrate, a protrusion formed on the top of each droplet at the end of the freezing process. This protrusion was formed because the latent heat of fusion was

partially removed by convection into the thermal boundary layer freezing the surface of the droplet before the interior was completely frozen. When the interior water froze and expanded, a protrusion was created at the top of the droplet. This protrusion acted as a site for water ablimation and a frost spire quickly grew from this location. On the hydrophilic substrate, no protrusion was observed to form. The spires were not limited to one spire per droplet. The early growth of spires was observed to be normal to the substrate surface with a low volume fraction. The contact angle has its greatest effect on the frost layer during the condensation period. After the condensation period, water ablimates onto existing frost and has little interaction with the substrate.

At some point, the spires begin to branch out and form a more uniform frost layer. The amount of growth parallel to the substrate is hypothesized to be related to the spacing between vertical frost spires. For a hydrophobic substrate the spacing between vertical frost spires can be directly related to the number of droplets on the substrate at the end of the condensation period. For a hydrophilic substrate, where condensate covers the majority of the substrate, and the spacing between drops (where frost cannot grow vertically) is small. The conductivity of the frost layer will be higher when the frost spires are more normal to the substrate.

The difference in conductivity accounts for the reversal in the trends in density and height observed in the early and mature frost growth on hydrophilic and hydrophobic substrates. A conductivity model has been adopted which accounts for the porosity and difference in the structure of the frost layer. A model was used to confirm the hypothesis that the conductivity of the frost layer can cause the reversal in frost density and thickness from the early to the mature growth period as a function of substrate.

The distribution of condensate is also a function of substrate temperature. Colder substrate temperatures result in a larger numbers of smaller droplets. The distance between droplets is also smaller. The smaller distance between droplets results in a frost layer whose growth direction is more normal to the substrate with a higher effective thermal conductivity resulting in a taller less dense frost layer.

This work has provided a more fundamental understanding of how the initial distribution of condensate affects frost properties. For the refrigeration industry, this research offers an understanding of one more potential design parameter. By altering the contact angle on an evaporator, the frosting characteristics can be modified. A hydrophilic coating reduces the thermal insulating effect of the frost, and is therefore desirable. However, for a compact evaporator where the fin spacing is low, a hydrophilic coating would create a thicker frost layer which would decrease the airflow through the evaporator more quickly than if a hydrophobic coating were used. Optimization of an evaporator for a particular application should include contact angle as a design parameter.

8.2 Recommendations for Future Work

Although this body of work provides insights into frost growth, there are many questions and topics that require further investigation. Examining frost properties as a function of the initial condensate distribution under identical environmental conditions has shown the significance of the condensate distribution. With this knowledge, the effects of environmental parameters can be separated and quantified. The characteristics of crystal growth have been shown to be a function of crystal temperature and saturation ratio (Hobbs 1974), but the effect of directional variation in the vapor pressure gradients

(like those experienced in a frost layer) on growth direction and crystal growth characteristics is not well known.

The mobility of the deposited water vapor during the condensation period should be examined as a possible frost management scheme. Under certain conditions, the condensation period can last upwards of 10 minutes. During this period, the condensate can be actively or passively manipulated to either alter frost properties or simply remove condensate from the evaporator. Additionally, the duration of the condensation period is a function of the volume on the substrate; therefore, continually removing the condensate off of the evaporator may increase the length of the condensation period.

References

Abdel-Wahed, R. M., Hifni, M. A. and Sherif, S. A. (1984). "Heat and Mass Transfer from a Laminar Humid Air Stream to a Plate at Subfreezing Temperature." *International Journal of Refrigeration* **7**: 49-55.

ASHRAE (1998). ASHRAE Handbook: Refrigeration. Atlanta, ASHRAE.

Bauer, T. H. (1993). "A General Analytical Approach Toward the Thermal Conductivity of Porous Media." *Int. J. Heat Mass Transfer* **36**(17): 4181-4191.

Biguria, G. and Wenzel, L. A. (1970). "Measurement and Correlation of Water Frost Thermal Conductivity and Density." *I&EC Fundamentals* **9**: 129-138.

Bragg, M. B., Heinrich, D. C., Valarezo, W. O. and McGhee, R. J. (1994). "Effect of Underwing Frost on a Transport Aircraft Airfoil at Flight Reynolds Number." *Journal of Aircraft* **31**(6): 1372-1379.

Carey, V. P. (1992). Liquid-Vapor Phase-Change Phenomena: An Introduction to the Thermophysics of Vaporization and Condensation Process in Heat Transfer Equipment. Bristol, Taylor and Francis.

Davis, M. A. (1996). *Evaporator Calorimeter: The study of Overall Heat Transfer Performance,* Departement of Mechanical and Industrial Engineering. Urbana-Champaign, University of Illinois.

Dyer, J. M., Storey, B. D., Hoke, J. L., Jacobi, A. M. and Georgiadis, J. G. (2000). "An Experimental Investigation of the Effect of Hydrophobicity on the Rate of Frost Growth in Laminar Channel Flows." *ASHRAE Transactions* **106**(1): 143-151.

Emery, A. F. and Siegel, B. L. (1990). "Experimental Measurements of the Effects of Frost Formation on Heat Exchanger Performance." *Heat and Mass Transfer in Frost and Ice, Packed Beds and Environmental Discharges*. ed: R. V. Arimilli, D. E. Beasley, S. Sengupta, S. A. Sherif and R. G. Watts. New York, ASME. **139:** 1-7.

Fletcher, N. H. (1958). "Size Effect in Heterogeneous Nucleation." *Journal of Chemical Physics* **29**(3): 572-576.

Fletcher, N. H. (1959). "On Ice Crystal Production." *Journal of Meteorology* **16**: 173-180.

Fukada, S. and Inoue, K. (1999). "Internal Mass Flux Through Frost." *AICHE Journal* **45**(12): 2646-2652.

Georgiadis, J. G. (1996). "Microscopic Study of Frost Inception." *Proceedings 2nd European Thermal-Sciences Conference*. ed: C. P. Celata, P. DiMarco and A. Mariani. **1:** 269-277.

Georgiadis, J. G., Hoke, J. L. and Ramaswamy, M. (2000). "Quantitative Visulatization of Early Frost Growth via Scanning Confocal Microscopy." *International Journal of Heat and Mass Transfer* : under review, 2000.

Graham, C. and Griffith, P. (1973). "Drop Size Distributions and Heat Transfer in Dropwise Condensation." *International Journal of Heat Mass Transfer* **16**: 337-346.

Granasy, L. (1995). "Diffuse Interface Analysis of Ice Nucleation in Undercooled Water." *Journal of Physical Chemistry* **99**: 14182-14187.

Griffith, P. and Lee, M. S. (1967). "The Effect of Surface Thermal Properties and Finish on Dropwise Condensation." *International Journal of Heat and Mass Transfer* **10**: 697-706.

Hayashi, Y., Aoki, A., Adachi, S. and Hori, K. (1977a). "Study of Frost Properties Correlating with Frost Formation Types." *Journal of Heat Transfer* **99**: 239-245.

Hobbs, P. V. (1974). Ice Physics. Oxford, Clarendon Press.

Hoke, J. L., Georgiadis, J. G. and Jimenz-Flores, R. (2000). "Supercooling of Aqueous Solutions of Glycosylated Bovine Beta-Casein." *Annals of Biomedical Engineering* : under review.

Holden, K. M., Wanniarachchi, A. S., Marto, P. J., Boone, D. H. and Rose, J. W. (1984). "Evaluation of Organic Coatings for the Promotion of Dropwise Condensation of Steam." *Fundamentals of Phase Change: Boiling and Condensation*. ed: C. T. Avedisian and T. M. Rudy. New York, ASME. **HTD-Vol. 38:** 89-97.

Horibe, A., Fukusako, S. and Yamada, M. (1993). "Freezing Characteristics of an Aqueous Solution Droplet Installed on a Wall". *Transport Phenomena in Thermal Enginnering: Proceedings of the 6th International Symposium*, Seoul, Korea, Begall House Inc.

Jeon, N. L., Finnie, K., Branshaw, K. and Nuzzo, R. G. (1997). "Structure and Stability of Patterned Self-Assembled Films of Octadecyltrichlorosilane Formed by Contact Printing." *Langmuir* **13**: 3382-3391.

Jones, B. W. and Parker, J. D. (1975). "Frost Formation with Varying Environmental Parameters." *Journal of Heat Transfer* **97**: 255-259.

Kawanami, T., Yamada, M. and Fukusako, S. (1997). "Solidification Characteristics of a Droplet on a Horizontal Cooled Wall." *Heat Transfer-Japanese Research* **26**(7): 469-483.

Kraus, G. F. and Greer, S. C. (1984). "Vapor Pressure of Supercooled H2O and D2O." *Journal of Physical Chemistry* **88**: 4781-4785.

Le Gall, R., Grillot, J. M. and Jallut, J. (1997). "Modeling of Frost Growth and Densification." *International Journal of Heat Mass Transfer* **40**: 3177-3187.

Leemans, V., Magein, H. and Destain, M.-F. (1999). "Defect Segmentation on 'Jonagold' Apples Using Colour Vision and a Bayesian Classification Method." *Computers & Electronics in Agriculture* **23**(1): 43-53.

Lide, D. R., Ed. (1992). CRC Handbook of Chemistry and Physics. Ann Arbor, CRC Press, Inc.

MacKenzie, A. R. (1997). "Are the (Solid-Liquid) Kelvin Equation and the Theory of Interfacial Tension Components Commensurate." *Journal of Physical Chemistry B* **101**: 1817-1823.

Mao (1999). "Frost Characteristics and Heat Transfer on a Flat Plate Under Freezer Operating Conditions: Part I, Experimentation and Correlations." *ASHRAE Transactions* **105**(2): 231-251.

Mao, Y., Besant, R. W. and Falk, J. (1993). "Measurement and Correlations of Frost Properties with Laminar Airflow at Room Temperature over a Flat Plate." *ASHRAE Transactions* **99 (1)**: 739-745.

Mao, Y., Besant, R. W. and Rezkallah, K. S. (1992). "Measurement and Correlations of Frost Properties with Airflow over a Flat Plate." *ASHRAE Transactions* **98 (2)**: 65-78.

O'Neal, D. L., Bryant, J. A. and Parker, B. (1997). "Impact of a Hydrophobic Coating on the Frost Buildup and Defrost Performance of a Heat Pump Evaporator." *New Approach Toward Low-Temperature Thermal Engineering Without Fluorocarbon Refrigerants, Proceedings of the 45th Oji International Seminar*. ed: S. Fukusako and K. Hijikata. Tomakomai city, Hokkaido Japan**:** 181-187.

O'Neal, D. L. and Tree, D. R. (1984). "Measurement of Frost Growth and Density in a Parallel Plate Geometry." *ASHRAE Transactions* **90 (2A)**: 278-290.

Okoroafor, E. U. and Newborough, M. (2000). "Minimising Frost Growth on Cold Surfaces Exposed to Humid Air by Means of Crosslinked Hydrophilic Polymeric Coatings." *Applied Thermal Engineering* **20**: 737-758.

Ostin, R. and Andersson, S. (1991). "Frost Growth Parameter in a Forced Air Stream." *International Journal of Heat and Mass Transfer* **34**: 1009-1017.

Padki, M. M., Sheirf, S. A. and Nelson, R. M. (1989). "A Simple Method for Modeling the Frost Formation Phenomenon in Different Geometrics." *ASHRAE Transactions* **95 (2)**: 1127-1137.

Sahin, A. Z. (1994). "An Experimental Study on the Initiation and Growth of Frost Formation on a Horizontal Plate." *Experimental Heat Transfer* **7**: 101-119.

Sahin, A. Z. (1995). "An Analytical Study of Frost Nucleation and Growth during the Crystal Growth Period." *Warme- und Stoffubertragung* **30**(5): 321-330.

Saito, H., Tokura, I., Kishinami, K. and Uemura, S. (1984). "A Study of Frost Formation (Dimensionless Parameters Correlating Density and Thickness of Frost Layer)." *Heat Transfer-Japanese Research* **13**(4): 76-88.

Sami, S. M. and Duong, T. (1989). "Mass and Heat Transfer during Frost Growth." *ASHRAE Transactions* **95 (1)**: 158-165.

Schneider, H. W. (1978). "Equation of the Growth of Frost Forming on Cooled Surfaces." *International Journal of Heat Mass Transfer* **21**: 1019-1024.

Seki, N., Fukusako, S., Matsuo, K. and Uemura, S. (1984). "Incipient Phenomena of Frost Formation." *Bulletin of JSME* **27**(233): 2476-2482.

Seki, N., Fukusako, S., Matsuo, K. and Uemura, S. (1985). "An Analysis of Incipient Frost Formation." *Warme- und Stoffubertragung* **19**: 9-18.

Shinagawa, H., Hamada, T., Miyamoto, K. and Okuyama, K. (1994). "Heterogeneous Nucleation Characteristics of a Eutectic-Forming Vapor Mixture on a Cold Substrate." *Separation Science and Technology* **29**(14): 1823-1840.

Shinagawa, H., Miyamoto, K., Okuyama, K. and Wyslouzil, B. (1995). "Simulation of a Transient Heterogeneous Phase Transition." *Journal of Chemical Engineering of Japan* **28**(4): 456-461.

Shinagawa, H., Okuyama, K. and Kawamura, Y. (1992). "Observations of Heterogeneous Nucleation of Water Vapor on a Cold Substrate." *Journal of Chemical Engineering of Japan* **25**(4): 448-450.

Steyer, A., Guenoun, P., Beysens, D. and Knobler, C. M. (1991). "Growth of Droplets on a Substrate by Diffusion and Coalescence." *Physical Review A* **44**(12): 8271-8277.

Stoecker, W. F. (1957). "How Frost Formation on Coils Affects Refrigeration Systems." *Refrigeration Engineering* **65**(1): 42-46.

Storey, B. D. (1997). *Frost Growth in Laminar Channel Flows with Streamwise Vortices*, Department of Mechanical and Industrial Engineering. Urbana, University of Illinois.

Storey, B. D. and Jacobi, A. M. (1999). "The Effect of Streamwise Vortices on the Frost Growth Rate in Developing Laminar Channel Flows." *Int. J. Heat Mass Transfer* **42**: 3787-3802.

Swofford, D. (2000). Personal Communication.

Tanaka, H. (1975). "Measurements of Drop-Size Distributions During Transient Dropwise Condensation." *Journal of Heat Transfer* **97**: 341-346.

Tao, Y.-X. and Besant, R. W. (1993a). "Prediction of Spatial and Temporal Distributions of Frost Growth on a Flat Plate Under Forced Convection." *Journal of Heat Transfer* **115**: 278-281.

Tao, Y.-X., Besant, R. W. and Mao, Y. (1993b). "Characteristics of Frost Growth on a Flat Plate During the Early Growth Period." *ASHRAE Transactions* **99 (1)**: 746-753.

Tao, Y.-X., Mao, Y. and Besant, R. W. (1994). "Frost Growth Characteristics on Heat Exchanger Surfaces: Measurement and Simulation Studies." *Fundamentals of Phase Change: Sublimation and Solidification.* ed: P. H. Oosthuizen and P. G. Kroeger. New York, ASME. **HTD-Vol. 286:** 29-38.

Tassou, S. A. and Marquand, C. J. (1987). "Effects of Evaporator Frosting and Defrosting on the Performance of Air-to-Water Heat Pumps." *Applied Energy* **28**: 19-33.

Thigpen, J. J., Canterbury, J., Killgore, A. M. and Trammel, G. L. (1964). The Investigation of Heat Transfer and Frost Formation in Humid Air Flowing Across a Plate Surface Held at Subfreezing Temperatures. Ruston, Louisiana Polytechnic Inst.

Tokura, I., Saito, H. and Kishinami, K. (1983). "Study on Properties and Growth Rate of Frost Layers on Cold Surfaces." *Journal of Heat Transfer* **105**: 895-901.

Turnbull, D. and Vonnegut, B. (1952). "Nucleation Catalysis." *Industrial and Engineering Chemistry* **44**(6): 1292-1298.

Yamakawa, N., Takahashi, N. and Ohtani, S. (1972). "Forced Convection Heat and Mass Transfer under Frost Conditions." *Heat Transfer: Japanese Research* **2**: 1-10.

Yonko, J. D. and Sepsy, C. F. (1967). "An Investigation of the Thermal Conductivity of Frost While Forming on a Flat Horizontal Plate." *ASHRAE Transactions* **73 (2)**: I.1.1-I.1.10.

Appendix A Substrate Cleaning Protocols

There were several different cleaning protocols for the different substrates. These procedures were followed prior to the experiments and prior to measuring contact angles or surface roughness. The variation in the procedures is primarily due to logistics. Because of the size of the samples used in the macro-wind tunnel, and the available cleaning equipment, samples were cleaned with a soft cloth and ethyl alcohol. The sample was used once and then discarded.

The cleaning procedure used for samples tested in the micro-wind tunnel varied depending on the purpose of the test. PTFE and kapton samples were cleaned with a soft cloth and ethyl alcohol to duplicate the surface tested in the macro-wind tunnel. The glass cover-slips tested in the micro-wind tunnel went through a more vigorous cleaning procedure: (i) 5 minutes cleaning in an ultrasonic bath with detergent at 50°C, (ii) water and de-ionized water wash, (iii) 5 minutes cleaning in an ultrasonic bath in de-ionized water at 50°C, (iv) de-ionized water wash and (v) drying on a hotplate at 300°C.

The silicon wafers went through a vigorous cleaning procedure also. The cleaning procedure for the silicon wafer was a three step process: (i) the wafer was washed with water, acetone and isopropyl alcohol and then dried with nitrogen gas, (ii) the wafer was then exposed to 10 minutes of ultraviolet light at a distance of 20 mm, and (iii) the wafer was washed with water, acetone, and isopropyl alcohol for three cycles before being dried by nitrogen gas.

Appendix B Frost Growth Simulation

```
      Real  LE,rhovplus(11),rhov(11),pt,error,lay,drops,CA,ksurf,
     &      rhosurf,Tcheck,keff(11),cpf,Tair,effd,mdot(11),mdotplus(11)
     &      ,pv(11),hsg,A(11,11),X(11),rho(11),rhoice,dz,dt,epsbminus(1
     &      1),epsbplus(11),epsb(11),delta,Time,Temp(11),Tplus(11),Tpla
     &      te,cp,C1,h,hm
      Real  cpf1,cpf2,C2,deltanot,dzplus,angle,density,Fo,Ja,Phi,
     &      ETA,Bi,rhov1,rhov2,pv1,pv2,tau
      Integer I,J,K,L,M,N,NGAS
      String      data
      NGAS=1
      rhoice=997
      hsg=2838
      cice=4.184
      Pref=.2602
      Tref=263.15
      Rv=.46152
      pt=101
      h=50
      Le=.91
      Tplate=253
      Tair=293
      effd=4e-9
      Write(*,*)'Input End Time in Minutes'
      Read(*,*)Time
      Time=Time*60.0
      delta=0.001
      ANGLE=55.0
      dt=1.0
      Wnot=0.005
C     ***** Read input variables
      open(file='initialconditions',unit=8,status='old')
      read(8,*)Tplate
      write(*,*)'Tplate',Tplate
      read(8,*)Tair,trash
      write(*,*)'effd',effd
      read(8,*)Wnot,trash
      write(*,*)'absolute humidity',Wnot
      read(8,*)effd,trash
      write(*,*)'effd',effd
      read(8,*)delta,trash
      write(*,*)'delta',delta
      read(8,*)lay,trash
      write(*,*)'waterlayer',lay
      read(8,*)drops,trash
      write(*,*)'number of drops',drops
      read(8,*)CA,trash
      write(*,*)'contact angle',CA
      read(8,*)ksurf,trash
      write(*,*)'conductivity',ksurf
      read(8,*)rhosurf,trash
      write(*,*)'density of new layer',rhosurf
      Close(8)
C     *****  Input variables read
```

```
      deltanot=delta
      dz=(delta-lay)/8.0
      Call GASPT(NGAS,Tair,rhoa,xmu,xk,cp,grb,pr,ier)
      hm=h/(rhoa*cp*Le**.66666)
      error=1.0
      data='frostdata'
      OPEN ( FILE=data, UNIT=7, STATUS='UNKNOWN')
      write(7,*)'h,height,surfac Temp,density'
      Do 2 I=1,10
      Do 3 j=1,10
            A(I,J)=0.0
3     Continue
2     Continue
      rho(1)=rhosurf
      epsb(1)=(rho(1)-1.4)/(rhoice-1.4)
      keff(1)=ksurf
      h=2
      Do 7 while (h.LT.6)
            h=h+5
            Call GASPT(NGAS,Tair,rhoa,xmu,xk,cp,grb,pr,ier)
            hm=h/(rhoa*cp*Le**.66666)
            rho(1)=rhosurf
            epsb(1)=(rho(1)-1.4)/(rhoice-1.4)
            keff(1)=ksurf
      Do 5 I=2,9

      mdot(I)=0.0
      epsb(I)=.05
      Temp(I)=Tplate
C     write(*,*)Temp(I)
5     Continue
      Temp(1)=Tplate
      mdot(1)=0.0
      Temp(10)=Tplate
      dz=(delta-lay)/8.0
      Call GASPT(NGAS,Tair,rhoa,xmu,xk,cp,grb,pr,ier)
      Ja=cp*(Tair-273.15)/hsg/1000.0

      pv2=pref*exp(-hsg/Rv*(1.0/273.15-1.0/Tref))
      rhov1=Wnot*rhoa
      rhov2=pv2/Rv/273.25
      Phi=(rhov1-rhov2)/rhoa
      eta=(Tair-273.15)/(273.15-Tplate)
      Fo=8.7e-4/cp/0.0127**2
      Bi=(Ja*Le**.666667)/(eta*(Ja*Le**.666667+phi))
      tau=Fo*Bi*Phi/Le**.666667

      L=1
      Do 10 I=1,Time
            If ((I-L*100)=0) Then

      avg=(epsb(1)*lay+epsb(2)*dz+epsb(3)*dz+epsb(4)*dz+epsb(5)*dz+
            epsb(6)*dz+epsb(7)*dz+epsb(8)*dz+epsb(9)*dz)/delta
                  rhoavg=avg*rhoice
                  write(7,*)I,',',h,',',delta,',',Temp(10),',',rhoavg
                  L=L+1
            endif
```

```
      Tcheck=Temp(10)
      Call GASPT(NGAS,Temp(10),rhoa,xmu,xk,cp,grb,pr,ier)
      rho(9)=epsb(9)*rhoice+(1-epsb(9))*(rhoa)
      pv(10)=pref*exp(-hsg/Rv*(1.0/Temp(10)-1.0/Tref))
      pv(1)=pref*exp(-hsg/Rv*(1.0/Temp(1)-1.0/Tref))
      pv(9)=pref*exp(-hsg/Rv*(1.0/Temp(9)-1.0/Tref))
      rhov(10)=pv(10)/Rv/Temp(10)
      rhov(9)=pv(9)/Rv/Temp(9)
c     keff(9)=1.*(0.02422+7.214e-4*rho(9)+1.1797e-6*(rho(9))**2)
      call conduct(Keff(9),epsb(9),Angle,9,dz,tau,I)
      W=0.6218*(pv(10)/(pt-pv(10)))

      density=((.14-.02)*(1.0-exp(sqrt(real((I*tau)))/0.1*
                  (-1.0)))+.02)

      deltaplus=delta+(hm*(Wnot-W)*rhoa-effd*
            (1.0-epsb(9))*(rhov(10)-
            rhov(9))/dz)*dt/(density*rhoice)/1.0
      dzplus=(deltaplus-lay)/8.0
      DO 15 M=2,8
            epsb(M)=(epsb(M)*(dz-(dzplus-dz)*
                  real(M-2.0))+epsb(M+1)*(dzplus-dz)*
                  real(M-1.0))/dzplus
            rho(M)=epsb(M)*rhoice+(1-epsb(M))*(rhoa)
            call conduct(Keff(m),epsb(m),Angle,m,dzplus,tau,I)
15    CONTINUE
            epsb(9)=(epsb(9)*(dz-(dzplus-dz)*7.0)+density*
                  (dzplus-dz)*8.0)/dzplus
            rho(9)=epsb(9)*rhoice+(1-epsb(9))*(rhoa)

            call conduct(Keff(9),epsb(9),Angle,9,dz,tau,I)
      dz=dzplus
c     write(*,*)'deltaplus',deltaplus
      rho(9)=epsb(9)*rhoice+(1-epsb(9))*(rhoa)
c     Temp(10)=Tair-(keff*(Temp(10)-Temp(9))/
            dz-hsg*1000*rho*(deltaplus-delta)/dt)/h
      Temp(10)=1.0/(keff(9)/dz+h)*(h*Tair+keff(9)/dz*Temp(9)+
                  hsg*1000*rho(9)*(deltaplus-delta)/dt)
      If (I=1) then
            temp(10)=Tplate
      endif
c     write(*,*)'temp(10)',Temp(10)

      pv(10)=pref*exp(-hsg/Rv*(1.0/Temp(10)-1.0/Tref))

      rhov(1)=pv(1)/Rv/Temp(1)
      rhov(10)=pv(10)/Rv/Temp(10)
c     write(*,*)'****',rhov(10)
      A(1,1)=1
      X(1)=Tplate
      A(10,10)=1
      X(10)=Temp(10)
```

```
              J=1
              Do 20 While (J.lt.9)
C                   Write(*,*)'20'
                    J=J+1
C                   write(*,*)J,Temp(j)
                    Call GASPT(NGAS,Temp(J),rhoa,xmu,xk,cp,grb,pr,ier)
c                   write(*,*)'pref',pref
c                   write(*,*)'T(J)',Temp(J)
                    pv(J)=pref*exp(-hsg/Rv*(1.0/Temp(J)-1.0/Tref))
                    rhov(J)=pv(J)/Rv/Temp(J)
c                   write(*,*)'pv',pv(J)
                    rho(J)=epsb(J)*rhoice+(1.0-epsb(J))*(rhoa)
                    call conduct(Keff(j),epsb(j),Angle,j,dz,tau,I)
c                   write(*,*)'keff',keff
                    cpf1=(epsb(J)*rhoice*cice*1000+
                          (1.0-epsb(J))*cp*rhoa)/rho(J)
                    cpf2=(epsb(J-1)*rhoice*cice*1000+
                          (1.0-epsb(J-1))*cp*rhoa)/rho(J-1)
                    C1=keff(J)*dt/(dz**2)/((rho(J)+
                          rho(J-1))/2.0)/((cpf1+cpf2)/2.0)
                    C2=keff(J-1)*dt/(dz**2)/((rho(J)+
                          rho(J-1))/2.0)/((cpf1+cpf2)/2.0)
                    If (J=2) then
                          C2=keff(J-1)*dt/(lay**2)/((rho(J)+
                                rho(J-1))/2.0)/((cpf1+cpf2)/2.0)
                    endif
c                   write(*,*)'rho',rho(J-1),keff(J-1)
                    A(J,J-1)=-1.0*C2

                    A(J,J)=1.0+C1+C2
                    A(J,J+1)=-1.0*C1
                    X(J)=Temp(J)-(mdot(J)+mdot(J-1))/2.0*
                          hsg*1000*dt/((rho(J)+
                          rho(J-1))/2.0)/((cpf1+cpf2)/2.0)

20    Continue
                    Do 33 k=1,10
C                         write(*,*)k,X(k)

                    do 34 j=1,10
C                         write(*,*)A(k,j)
34    continue
33    continue
                    Call Gauss(10, A, X, Tplus)

                    Do 22 K=1,10
C                         write(*,*)k,Tplus(k)
                          pv(K)=pref*exp(-hsg/Rv*(1.0/Temp(K)-1.0/Tref))
                          pvplus=pref*exp(-hsg/Rv*(1.0/Tplus(K)-
1.0/Tref))
                          rhovplus(K)=pvplus/Rv/Tplus(K)
                    Do 23 j=1,10
                          A(K,J)=0.0
23    Continue
22    Continue
                    rhovplus(1)=rhovplus(2)
c                   write(*,*)'rhovplus',rhovplus(1),rhovplus(2)
```

```
              Do 30 N=2,9
                    epsbplus(N)=epsb(N)+(1.0*effd*(1-epsb(N))*
                          (rhovplus(N+1)-2*rhovplus(N)+
                          rhovplus(N-1))/dz**2+(epsb(N)-1.0)*
                          (rhovplus(N)-rhov(N))/dt)*dt/(rhoice-
                          rhovplus(N))
C                   write(*,*)'epsbplus',epsbplus(N)
                    rho(N)=epsb(N)*rhoice+(1.0-epsb(N))*(rhoa)
                    mdotplus(N)=-1.0*(epsbplus(N)-epsb(N))/dt*rhoice
C                   write(*,*)'mdot',mdot(n)
                    error=mdotplus(N)-mdot(N)
                    mdot(N)=mdotplus(N)
                    epsb(N)=epsbplus(N)
30    Continue




      delta=deltaplus
C     write(*,*)'delta',delta
      Do 60 K=2,10
            Temp(K)=Tplus(K)
C           write(*,*)'temp',temp(k)
            epsb(K)=epsbplus(K)
60    Continue
10    Continue
      avg=(epsb(1)*lay+epsb(2)*dz+epsb(3)*dz+epsb(4)*dz+epsb(5)*dz+
            epsb(6)*dz+epsb(7)*dz+epsb(8)*dz+epsb(9)*dz)/delta
      write(*,*)epsb(1),epsb(2),epsb(3),epsb(4),epsb(5),epsb(6),epsb(7)
      ,
            epsb(8),epsb(9),epsb(10)
      write(*,*)Temp(1),Temp(2),Temp(3),Temp(4),Temp(5),Temp(6),Temp(7)
,Temp(8),Temp(9),Temp(10)
      rhoavg=avg*rhoice
      write(7,*)I,',',h,',',delta,',',Temp(10),',',rhoavg
      write(*,*)h,',',delta,',',Temp(10),',',rhoavg
      delta=deltanot
7     Continue

      Close (7)

      End




      SUBROUTINE GASPT(NGAS,T,RHO,XMU,XK,CP,GRB,PR,IER)
C  PROGRAMMED BY: A. M. CLAUSING;  VERSION: APRIL 1982
C  PROPERTIES OF GASES IN SI UNITS(T.GT.0) OR ENGLISH UNITS(T.LT.0)
C  FUNCTIONAL REPRESENTATIONS USED ARE OF THE FORM:  Y=A*T**B.
C  ARRAYS A AND B CONTAIN THE RESPECTIVE CONSTANTS.
C  INPUT:
```

```
C  NGAS     NGAS=1 IS AIR;  NGAS=2 IS NITROGEN
C  T  ABSOLUTE TEMP. (K);  OR NEGATIVE OF ABSOLUTE TEMP. (R)
C  OUTPUT:
C  RHO      DENSITY (KG/M3) OR (LBM/FT3)
C  XMU      VISCOSITY (KG/M-S) OR (LBM/FT-S)
C  XK THERMAL CONDUCTIVITY (W/M-K) OR (BTU/HR-FT-R)
C  CP SPECIFIC HEAT (J/KG-K) OR (BTU/LBM-R)
C  GRB      G*BETA/XNU**2 (1/M3-K) OR (1/FT3-R)
C  PR PRANDTL NUMBER (DIMENSIONLESS)
C  IER      ERROR PARAMETER
C INFORMATIVE ERRORS:
C     IER=1 GAS NUMBER DOES NOT EXIST.  GAS IS ASSUMED TO BE AIR.
C     IER=2 TEMPERATURE OUT OF RANGE OF PROPERTY SUBROUTINE
C RESTRICTIONS:
C     NGAS:       MUST BE 1(AIR) OR 2(NITROGEN)
C     T:          T MUST LIE BETWEEN 150K AND 2100K FOR AIR, AND
BETWEEN
C                 83K AND 450K FOR NITROGEN. RANGES ARE SPECIFIED WITH
ARRAY R.
C
      DIMENSION A(15,2),B(15,2),R(3,2)
      DATA A/364.1,.1764E-6,.1423E-3,990.8,.4178E20,1.23,
     2 350.6,.4914E-6,.2494E-3,299.4,.4985E19,.59,3*.0,
     3 432.4,9.1E-8,1.239E-4,1553.,4.379E20,1.137,
     4 351.6,.18E-6,.221E-3,1031.,.408E20,.841,3*.0/
      DATA B/-1.005,.814,.9138,.00316,-4.639,-.09685,
     2 -.999,.6429,.8152,.1962,-4.284,.0239,3*.0,
     3 -1.046,.938,.9466,-.079,-5.102,-.0872,
     4 -1.005,.8058,.8345,.00239,-4.636,-.02652,3*.0/
      DATA R/150.,400.,2100.,83.,160.,450./
      IER=0
      IF((NGAS.GT.0).AND.(NGAS.LT.3)) GO TO 1
      IER=1
      NGAS=1
1     I=1
      TP=T
      IF(T.LT..0) TP=-T/1.8
      IF((TP.LT.R(1,NGAS)).OR.(TP.GT.R(3,NGAS))) IER=2
      IF(TP.GT.R(2,NGAS))I=7
      RHO=A(I,NGAS)*TP**B(I,NGAS)
      XMU=A(I+1,NGAS)*TP**B(I+1,NGAS)
      XK=A(I+2,NGAS)*TP**B(I+2,NGAS)
      CP=A(I+3,NGAS)*TP**B(I+3,NGAS)
      GRB=A(I+4,NGAS)*TP**B(I+4,NGAS)
      PR=A(I+5,NGAS)*TP**B(I+5,NGAS)
      IF(T.GT..0)RETURN
      RHO=RHO/16.02
      XMU=XMU/1.488
      XK=XK/1.731
      CP=CP/4187.
      GRB=GRB/63.57
      RETURN
      END
```

```
            subroutine gauss(n, a, b, x)
      real a(11,11), b(11), x(11), temp

      integer j, k, l, inx, n

c     elimination
      do 10 k=1,n
        do 20 j=1,n
        if(j .gt. k) then
          temp = a(j,k)/a(k,k)
          do 30 l=k,n
 30       a(j,l) = a(j,l) - temp*a(k,l)
        b(j) = b(j) - temp*b(k)
      endif
 20    continue
 10   continue

c     back substitution
      do 40 k=1,n
        inx = n-k+1
        x(inx) = b(inx)/a(inx,inx)
        do 50 j=1,n
          if( (inx + j) .le. n) then
            x(inx) = x(inx) - (a(inx,inx+j)/a(inx,inx))*x(inx+j)
          endif
 50     continue
 40   continue

      return
      end

      Subroutine conduct(Keff,P,Angle,index,dz,tau,I)
      Real
ERROR,KP,KO,K(3),THETA,LEFT(3),RIGHT,PI,EPSB(9),angle,P,keff,dz,tau
      Integer I,J,M,index
      PI=3.14159
      KP=2.0
      KO=0.02
      THETA=((angle-25.0)*(1.0-exp(sqrt(real(I*tau))/0.1*
           (-1.0)))+25.0)*pi/180.0
      Error=1.0
      RIGHT=1.0-P
      K(1)=0.75
      left(1)=(K(1)-KP)/(KO-KP)*((K(1)+(1.0-SIN(THETA)*SIN(THETA))/
           (1.0+SIN(THETA)*SIN(THETA))*KP)/(KO+(1.0-SIN(THETA)*
           SIN(THETA))/(1.0+SIN(THETA)*SIN(THETA))*KP))**(-1.0*
           (SIN(THETA)*SIN(THETA))/(1+SIN(THETA)*SIN(THETA)))

     K(2)=0.05
     Do 50 While (0.0001.LT.ABS(Error))


           left(2)=(K(2)-KP)/(KO-KP)*((K(2)+(1.0-SIN(THETA)*
                SIN(THETA))/(1.0+SIN(THETA)*SIN(THETA))*KP)/(KO+(1.0-
                SIN(THETA)*SIN(THETA))/(1.0+SIN(THETA)*SIN(THETA))*
                KP))**(1.0*(SIN(THETA)*SIN(THETA))/(1+SIN(THETA)*
                SIN(THETA)))
```

```
            K(3)=(K(1)-K(2))/(LEFT(1)-LEFT(2))*(RIGHT-LEFT(2))+K(2)
            ERROR=K(2)-K(3)
            K(1)=K(2)
            LEFT(1)=LEFT(2)
            If (k(3).lt.0) then
                  k(3)=0.025

            endif
            K(2)=K(3)
c           write(*,*)right-left(2)
c           WRITE(*,*)ERROR

50    CONTINUE

c     WRITE(*,*) K(2),p
      keff=k(2)
```